Insulator Flashover Probability Investigation Based on Numerical Electric Field Calculation and Random Walk Theory

by

Jiahong He

A Dissertation Presented in Partial Fulfillment
of the Requirements for the Degree
Doctor of Philosophy

Approved June 2016 by the
Graduate Supervisory Committee:

Ravi Gorur, Chair
Raja Ayyanar
Keith Holbert
George Karady

ARIZONA STATE UNIVERSITY

August 2016

ABSTRACT

Overhead high voltage transmission lines are widely used around the world to deliver power to customers because of their low losses and high transmission capability. Well-coordinated insulation systems are capable of withstanding lightning and switching surge voltages. However, flashover is a serious issue to insulation systems, especially if the insulator is covered by a pollution layer. Many experiments in the laboratory have been conducted to investigate this issue. Since most experiments are time-consuming and costly, good mathematical models could contribute to predicting the insulator flashover performance as well as guide the experiments. This dissertation proposes a new statistical model to calculate the flashover probability of insulators under different supply voltages and contamination levels. An insulator model with water particles in the air is simulated to analyze the effects of rain and mist on flashover performance in reality. Additionally, insulator radius and number of sheds affect insulator surface resistivity and leakage distance. These two factors are studied to improve the efficiency of insulator design. This dissertation also discusses the impact of insulator surface hydrophobicity on flashover voltage.

Because arc propagation is a stochastic process, an arc could travel on different paths based on the electric field distribution. Some arc paths jump between insulator sheds instead of travelling along the insulator surfaces. The arc jumping could shorten

the leakage distance and intensify the electric field. Therefore, the probabilities of arc jumping at different locations of sheds are also calculated in this dissertation.

The new simulation model is based on numerical electric field calculation and random walk theory. The electric field is calculated by the variable-grid finite difference method. The random walk theory from the Monte Carlo Method is utilized to describe the random propagation process of arc growth. This model will permit insulator engineers to design the reasonable geometry of insulators, to reduce the flashover phenomena under a wide range of operating conditions.

ACKNOWLEDGMENTS

I would like to express my sincere gratitude to Professor Ravi S. Gorur for his continuous guidance and support in my two years study. His advice, patience and understanding not only help me with my academic research but also improve my communication skills and career development.

I especially want to thank Professor Raja Ayyanar and Professor Keith Holbert, Professor George Karady. Thank you for your time and consideration to be my committee members.

In addition, I am also grateful for all the professors in the power system group. In my five years study, I have learned a lot from each course.

I would like to acknowledge all my friends at Arizona State University, who encourage me and give me confidence as always.

Finally, I would like to thank my parents for their extended care and support.

TABLE OF CONTENTS

Page

CHAPTER Page

CHAPTER Page

CHAPTER Page

LIST OF TABLES

Table Page

Table Page

LIST OF FIGURES

Figure Page

Figure Page

Figure Page

Figure Page

Figure Page

Figure Page

NOMENCLATURE

AC	Alternating current
BEM	Boundary element method
CSM	Charge simulation method
DC	Direct Current
E	Electric field intensity
EHV	Extra High Voltage
FDM	Finite Difference Method
FEM	Finite Element Method
IEEE	Institute of Electrical and Electronics Engineers
kV	Kilovolts
P	Probability
PC	Personal computer
RW	Random Walk
UHV	Ultra High Voltage
V	Voltage on the insulator boundary

1 INTRODUCTION

1.1 Introduction to High Voltage Insulators and Flashover Models

High voltage transmission lines bring the power from remote generating stations to consumers. These lines could span over thousands of miles. The efficiency of the power transmission systems mainly depends on the continuity of the service, and avoiding faults that could cause economic losses to utilities and users [1].

Insulators are used to provide mechanical support of transmission lines as well as electrically isolate the conductors from the ground [2]. To maintain the continuity of power transmission, one of the main issues is the flashover in the air around the insulators. Flashover is a dielectric breakdown phenomenon that the insulator suddenly becomes conductive, if electric field applied across the insulating substance exceeds the threshold dielectric strength. The probability of flashover increases significantly when the insulator is covered by the pollution layer. The pollution layer is deposited on the insulator surface due to various types (industrial, marine and desert) of contamination [3]. When the surface of a polluted high voltage insulator is dampened due to dew deposition, fog or rain, a wet conducting film is formed and the leakage current flows through the surface. Insulator surface resistivity would reduce significantly due to the contamination. Meanwhile, water particles in the mist or rain could distort the electric field distribution between insulator sheds and influence the track of arc propagation. Furthermore, insulator radius and number of sheds are two

critical factors of insulator geometry to influence the surface resistivity and leakage distance [4]. Therefore, these two factors are analyzed to evaluate their effects on the insulator flashover performance. In addition, new composite insulators are difficult to wet at the beginning. However, material degradation in the form of tracking and erosion influence the insulator surface condition after long-term outdoor exposure. The surface wettability of aged composite insulators significantly increases [5]. Hence, seven classes of hydrophobicity are introduced to evaluate the impact of insulator surface condition on flashover voltage [6].

The process of flashover consists of many steps of arc propagation. The criterion for arc growth is that the electric field strength exceeds the dielectric strength of insulation materials [7] and arc instant energy exceeds ionization energy [8]. Arc instant energy is calculated by leakage current density and potential distribution on the insulator surface. The dielectric strength of multiple insulation materials is shown in Table 1.

Table 1. Dielectric Strength of Different Materials

Materials	Dielectric Strength (kV/mm)
Air [7]	3.0
Epoxy [9]	220.0 - 253.0
Porcelain [9]	125 - 160
Glass [10]	470 – 670

The arc propagation may create a conductive path from high voltage electrode to the ground electrode, which eventually completes the flashover. The flashover phenomena would induce an instantaneous large amount of current to trigger the protection breaker and cause the system interruption.

Since reducing the flashover phenomena is essential to maintain continuous power transmission, many methods are used to predict flashover phenomena. These methods can be categorized into two classes: laboratory experiments and computer simulations. With the consideration that laboratory experiments are time-consuming and costly, simulations are conducted first to guide the experiments. Obenaus and Neumarker started the modeling of flashover with a mathematic expression [11]. Afterwards, Rizk reviewed the mathematical models for pollution flashover and proposed a flashover equation for AC voltage [12]. In 1858, Jolly, Cheng and Otten first considered the instantaneous arc parameters and created a dynamic model of arc propagation [13]. Later on, a large improvement was accomplished by Sundararajan with the consideration of arc propagation with time [14]. However, the arc propagation in reality is a stochastic process rather than a deterministic one in the previous models. Therefore, a new statistical model is proposed in this dissertation to calculate the flashover probability. This model is based on numerical electric field computation and Random Walk Theory.

With the development of computer technology, numerical methods are employed

in electric potential and field simulation. The common numerical methods are finite element method (FEM), finite difference method (FDM), boundary element method (BEM), and charge simulation method (CSM) [15]. In the flashover model, the electric field around the arc in air is required to determine the arc propagation directions. It has been shown that only FEM and FDM can calculate the electric field both in the homogenous material and on the boundary between different materials, while CSM and BEM merely focus on the electric field on the boundary [16]. Furthermore, FDM has certain advantages over FEM in terms of computational complexity when the geometry of the model is regular [17]. Therefore, FDM is selected to analyze the flashover probability in this dissertation.

Random walk is a mathematical formalization of a path that contains a succession of random steps. At each step, the random walking particle has a certain probability to go any direction in space. The particle stops walking when it reaches the boundary [18]. In the flashover model, arc propagation process is simulated by the random walking path of the particle.

1.2 Types of Insulators

Outdoor insulators are used to provide mechanical support of transmission lines and to electrically isolate the conductors from structures. Due to different dielectric materials, Outdoor insulators are classified into three types: porcelain, glass and composite.

1.2.1 Porcelain Insulators

Porcelain insulators are also referred to ceramic insulators, and they have been used for more than a century [19]. These insulators can be categorized as cap-and-pin insulators and long rod suspension insulators. The schematics of two types of insulators are shown in Figure 1.

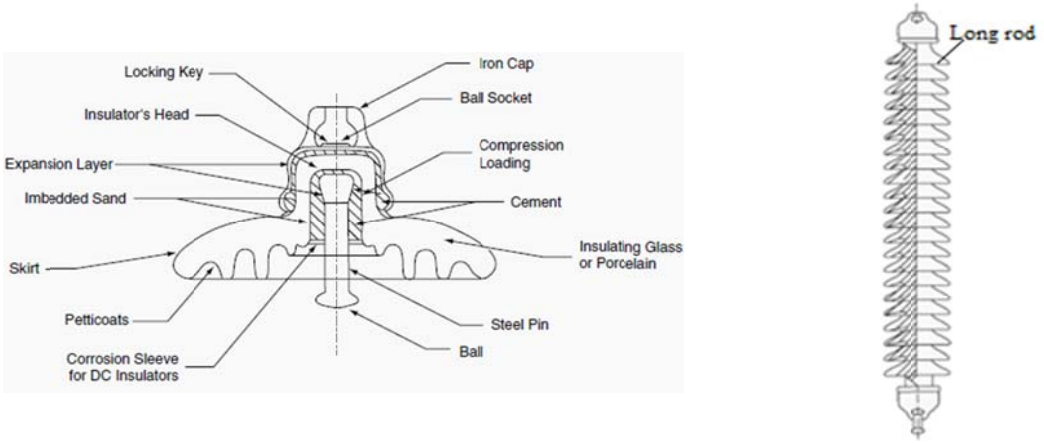

(a) The Structure of Cap-and-pin Insulator (b) The Structure of Long rod Suspension Insulator

Figure 1. The Porcelain Insulator

The cap-and-pin insulators are made up of galvanized malleable iron pins and caps with Portland cement mortar. These insulators are divided into two groups: non-stacking and stacking units [20]. The non-stacking insulators contain one piece of shed between one pair of electrodes, while the stacking units have multi-piece sheds

between one pair of electrodes. Compared to the cap-and-pin insulators, the rod suspension insulators are designed to avoid the puncture completely [21]. These insulators are able to stand more severe pollution, due to the increased leakage distance [22].

The mechanical performances of cap-and-pin insulators and long rod suspension insulators are determined by all the components of the insulators, and require careful treatment. The electrical performance of insulators is dependent on both surface and volume properties [23]. When the porcelain insulator surfaces are wet, water and contaminants tend to form a continuous pollution layer, which could lead to significant decrease of surface resistivity.

1.2.2 Glass Insulators

The glass is prone to fracture under stress, which increases the possibility of dropping conductors, while the cracks on the glass surface also impact the surface property and intensify the field distribution [24]. Therefore, the glass insulators did not initially provide good electrical and mechanical performance in the early ages. The materials of glass insulators have improved significantly after many experiments. Currently, the glass material is toughened by adding potassium, barium, and aluminum [25]. The toughened insulators have a better mechanical performance than the porcelain insulators, which allow thinner shells to be used. Therefore, the voltage stress of glass insulators also increases 40%, when compared to porcelain insulators

[26]. In addition, glass insulators do not need glazing during manufacturing, and their immunity to erosion is stronger than porcelain insulators.

The glass insulators are divided into three categories, pin-type glass insulators, suspension glass insulators and multicone post insulators [27]. The most common type is suspension glass insulators (Figure 2).

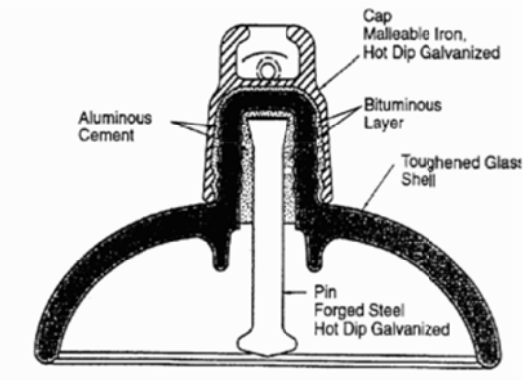

Figure 2. The Structure of Suspension Glass Insulators [4]

1.2.3 Composite Insulators

Composite insulators are also referred to non-ceramic insulators, whose insulation material and mechanical material are combined. The composite insulators are widely used around the world, for reasons of lighter weight and better performance under contaminated conditions. Flashover performance of composite insulators is also better than that of porcelain insulators due to smaller diameter of the insulators and better hydrophobicity [28].

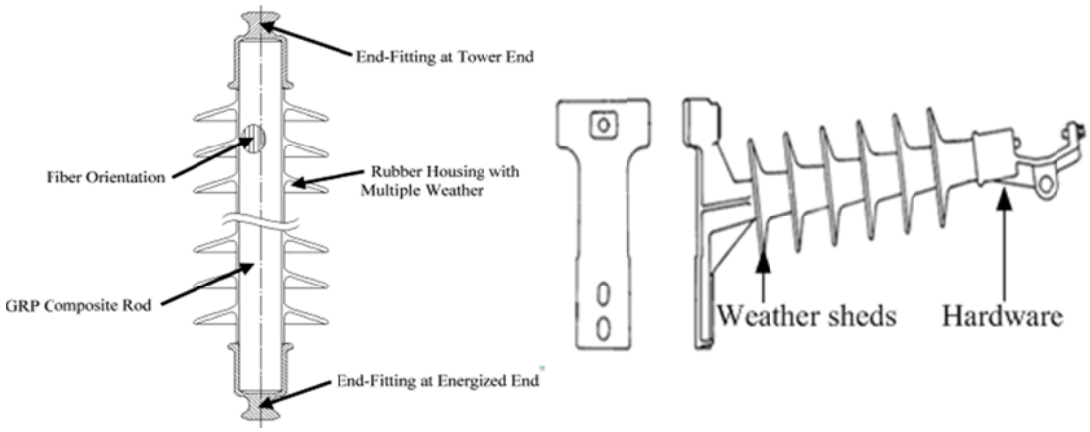

(a) The Structure of Suspension Insulator (b) The Structure of Line Post Insulator

Figure 3. The Composite Insulators

Composite insulators are commonly made of silicone rubber and ethylene propylene rubber. Composite insulators can either be suspension type or line post type. The structures of these two types of insulators are shown in Figure 3. Composite suspension insulator consists of fiberglass core, weather sheds and hardware on the end-fittings [29]. Line post insulators have similar components as suspension insulators. The radius of fiber glass core of line post insulator is larger than that of suspension insulator [13], because the line post insulator needs to undertake more mechanical loads.

1.3 Types and Levels of Contamination

The types and levels of contamination on the insulator surface are associated with the sources of contaminants and the climate of the place. Although many factors can define the insulators pollution, three main types of contamination can be highlighted: the industrial, coastal and desert [30].

1.3.1 Industrial Contamination

The industrial pollution of the insulators rises with the industries development and can be divided into diverse types: metallurgical, chemical substances, dust, smoke, cement and etc. The particles of contaminants are in the suspension of air and mainly spread by the action of wind over zones where transmission lines exist. These particles would settle on the insulator surfaces by the combination effects of the wind, weight and electric fields. Afterwards, a contamination layer is created on the insulator surface and this layer is formed slowly during a period that can last months or years. The sources of industrial pollutions are listed in Table 2 [31].

Table 2. Types and Sources of Industrial Pollutions

Metallic	Mineral mining area
Coal	Coal mining area
Chemical	Chemical industries: Paper mills, oil refineries and etc.
Smog	Automobile and diesel engine emissions
Smoke	Industry and agricultural burning

1.3.2 Coastal Contamination

The insulators exposed to coastal or marine environments could become conductors due to the formation of a conductive layer on their surface. This layer will be formed in terms of the salted dew of the mornings in these zones close to the coasts. When the layer is dried by the heat produced in the insulator or the environment temperature, the evaporated salt would deposit on the insulator surface. Although the salt particles on the insulators are not dangerous in dry weather, the layer may become continuous and conductive, once insulator the surface becomes wet again [32]. The conductivity of the layer depends on the type and density of the salt that forms it. Moreover, the weather conditions vary considerably from the coastal areas to the interior areas. They have a significant impact on the contaminants deposition rate and the insulator performances. With the passage of time the surface contamination layer will be thick enough to be dampened and increase the insulator conductivity [33].

1.3.3 Desert Contamination

The insulators are often subjected to the deposition of contaminants substances of the deserts, which significantly reduce the efficacy of the insulator. The predominant elements in desert contamination are the sand and the widespread salty dust in a dry atmosphere. In addition, the types of climate conditions also impact the insulators considerably. The dry insulators have normally low conductivity, but morning dew is going to dampen the layer and turns the insulator into a conductor. Since desert area has little quantity of rain, it is considerably difficult to naturally wash the insulator surface and to eliminate the contaminant layer [34]. Furthermore, the desert climate also includes sand storms and hurricanes which carry particles at a high speed. These particles would cause the material erosion by striking to the insulator surface. Therefore, the storms of sand are an important factor leading to a major reduction of reliability in the insulation systems [35].

1.3.4 Level of Contamination (ESDD)

Equivalent Salt Deposit Density (mg/cm^2) (ESDD) is used as the standard to describe the pollution severity on the insulator surface. ESDD considers climate effects, such as temperature, humidity, pressure and rain. Since the surface conductivity is used in numerical methods for field calculation, the ESDD values need to be converted to surface conductivity.

The salinity S_a of the solution is calculated as follows [36],

$$S_a = (5.7\sigma)^{1.03} \tag{1}$$

where σ is the surface conductivity (S/m).

In addition, *ESDD* is determined by the expression below [36],

$$ESDD = \frac{S_a Vol}{A} \tag{2}$$

where *Vol* is the volume of the distilled water (cm^3) and *A* is the insulator surface area in the empirical formula (cm^2).

Therefore, surface conductivity K_s is calculated by the empirical formula below [21],

$$K_s = \frac{\sqrt[1.03]{\frac{ESDD}{Vol} A}}{5.7} \tag{3}$$

2 NUMERICAL METHODS FOR FIELD COMPUTATION

Numerical electric field analysis has become an essential tool for the design and development of high voltage products. Continuous electric field distribution can be described by differential equations and boundary conditions. By discretizing the continuous domain into a number of elements or fictitious charges, numerical methods transfer these differential equations into a group of linear functions, which can be easily solved by computers.

2.1 Finite Element Method

The Finite Element Method (FEM) is one of the numerical analysis techniques for obtaining approximate solutions to the electromagnetic problems. In order to summarize in general terms how the FEM works, four steps are listed as follows [37]:

1) Discretize the continuous domain. Continuous differential equation and boundary conditions to describe a two dimension field domain are shown below,

$$\nabla^2 u = \frac{\partial^2 u}{\partial x^2} + \frac{\partial^2 u}{\partial y^2} = F(x, y) \quad \text{in the domain} \tag{4}$$

$$u(x, y)|_{\Gamma} = g_1(\Gamma) \quad \text{on the boundary} \tag{5}$$

$$\left.\frac{\partial u}{\partial n}\right|_{\Gamma} = g_2(\Gamma) \quad \text{on the boundary} \tag{6}$$

FEM divides the field domain into elements. These elements are small areas in the two dimension model or small volumes in the three dimension

model. A triangle is the most popular geometry element used in FEM. The smaller the element is, the more accurate the field strength would be. According to the steps above, the whole field domain can be described by each point potential of the elements [38]. An example of two dimension field discretization is shown in Figure 4.

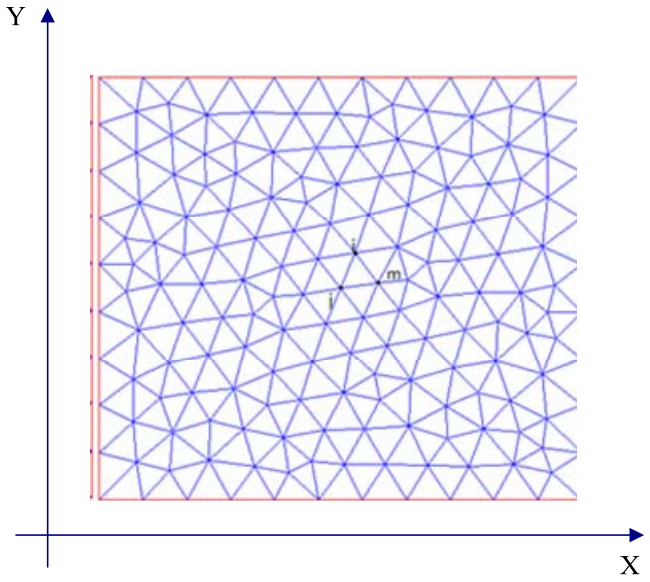

Figure 4. FEM Field Division and Example Triangle Element ijm

2) Select interpolation functions

Figure 4 shows the square field domain is divided by triangle elements. The second step is to assign nodes to each element and select proper interpolation functions. The potential in each triangle element has a relationship with the coordination of the triangle nodes.

$$\varphi = a_1 + a_2 x + a_3 y \tag{7}$$

If the discretized triangle is small enough, the field in the element is assumed as constant. Coefficients a_1, a_2 and a_3 can be calculated by the equations below.

$$\begin{cases} \varphi_i = a_1 + a_2 x_i + a_3 y_i \\ \varphi_j = a_1 + a_2 x_j + a_3 y_j \\ \varphi_m = a_1 + a_2 x_m + a_3 y_m \end{cases} \tag{8}$$

Where φ_i , φ_j and φ_m are potentials at the nodes of the triangle element.

3) Find the element properties

The calculated coefficients a_1, a_2 and a_3 are taken back into equation [39]:

$$\varphi = \frac{1}{2\Delta}\left[\left(a_i + b_i x + c_i y\right)\varphi_i + \left(a_j + b_j x + c_j y\right)\varphi_j + \left(a_m + b_m x + c_m y\right)\varphi_m\right] \tag{9}$$

Where $\triangle$ is the area of the triangle ijm.

Therefore,

$$\varphi = \begin{pmatrix} N_i & N_j & N_m \end{pmatrix} \begin{pmatrix} \varphi_i \\ \varphi_j \\ \varphi_m \end{pmatrix} \tag{10}$$

Where $N_i = \left(a_i + b_i x + c_i y\right)/2\Delta$, $N_j = \left(a_j + b_j x + c_j y\right)/2\Delta$ and $N_m = \left(a_m + b_m x + c_m y\right)/2\Delta$.

The variation problem is discretized with the principle of weighted residuals.

4) Solve the system equations

The matrix equation of triangle elements is shown below [39]:

$$[K] = \begin{bmatrix} K_{ii} & K_{ij} & K_{im} \\ K_{ji} & K_{jj} & K_{jm} \\ K_{mi} & K_{mj} & K_{mm} \end{bmatrix} \tag{11}$$

In the end, the discretized linear equations are represented as, $[K][\varphi] = [V]$, and the unknown potentials at the vertices of all the triangles are calculated.

Designers can divide the field domain by their own purpose with FEM. For example, small elements are set in the area where electric field changes intensively to achieve accurate results. In addition, FEM has strong robustness, when the geometry of electric field is irregular [40].

However, the calculation process of FEM is more complicated and time consuming than finite difference method. Furthermore, the storage capacity requirement of FEM is also considerably larger than that of FDM.

2.2 Boundary Element Method

The boundary element method focuses on the boundary conditions surrounding the field domain. Unique characteristic of this method is to decrease the dimensions of the problem. A two dimensional problem can be described by the boundary line and reduced to one dimensional problem. Three dimensional problems can be described by the boundary surface, and reduced to a two dimensional problem. The procedure of boundary element method is shown below [41],

1) The boundary is discretized into many elements in functions with unknown potentials and normal flux densities.
2) The principle of weighted residuals is used to minimize the error.
3) The coefficient matrix is evaluated after analysis of each element.
4) The linear algebraic equations are then achieved with the proper boundary conditions to the nodes.
5) In the end, the unknown potentials can be calculated from the inversion of the coefficient matrix.

The major advantage of the boundary element method is to reduce the dimensions of the space, so that the orders of the differential equations and the amount of input data are decreased. However, the coefficient matrix is an unsymmetrical full element matrix, which consumes large amounts of computation resources and limits the orders of the matrix [42]. The method makes it difficult to handle multi-media field domain, and cannot be used directly for nonlinear problems. Moreover, as one of the boundary methods, BEM is only capable of calculating the electric potential and field distribution on the interface between different materials. The internal field of a homogenous material cannot be solved by BEM [43].

2.3 Charge Simulation Method

The charge simulation method belongs to the category of boundary methods. This method assembles the effect of each simulating charge to calculate the electric

potential and field distribution. The steps of the charge simulation method are listed below [44]:

1) The simulating charges are introduced and set out of the field domain.
2) The positions of contour points are then determined on the boundaries between different media. The potentials at the contour points are known as boundary conditions [45].
3) According to the superposition principle, the equations of potentials versus simulating charges are obtained:

$$\begin{aligned} \varphi_1 &= P_{11}Q_1 + P_{12}Q_2 + \cdots + P_{1n}Q_n \\ \varphi_2 &= P_{21}Q_1 + P_{22}Q_2 + \cdots + P_{2n}Q_n \\ &\vdots \\ \varphi_n &= P_{n1}Q_1 + P_{n2}Q_2 + \cdots + P_{nn}Q_n \end{aligned} \tag{12}$$

Where P_{ij} is the potential and normal flux coefficient between contour points and simulating charges, Q_j represents the unknown simulating charges and φ_i is the potential and normal flux on the contour points.

4) The equations above are solved to calculate the values of the simulating charges.
5) The check points are selected on the boundary to verify the accuracy requirement. If the accuracy is not satisfied, the number and positions of the simulating charges need to be rearranged [46].

The CSM has some advantages over other methods in the insulator design. For insulators that are rotationally symmetric, CSM can reduce the computational

complexity in three-dimension simulation [47].

Whereas, CSM requires the designers' experience to choose the right number of charges and contour points, and then place them properly to satisfy the accuracy requirement [48]. If the coefficient matrix P gets singular, the results would have large errors. Similar to boundary element method, CSM is merely able to calculate electric potential and field on the boundary rather than any other locations in the field domain.

2.4 Finite Difference Method

The principal of finite difference method is to divide the field domain with regular grid, and replace the Poisson's equations with the linear equations, whose unknown variables are the potentials at the nodes of the grid [49]. Among all the methods introduced above, optimized finite difference method is used in the flashover model to calculate the field. The advantages of this method are shown below:

1) In the flashover model, the electric field around the arc in air needs to be analyzed. Boundary element and charge simulation methods can merely calculate the field distribution along the boundary surface between different materials. As a result, only the finite difference and finite element methods can be used to calculate the whole field values in the domain of both insulating material and air.
2) Since the flashover model is in two-dimension and geometry of the insulator model is regular, finite difference method is more efficient in RAM space and less time-consuming than finite element method.

The Poisson's equations and the boundary conditions to describe the two-dimension field domain are shown below [50]:

$$\nabla^2 u = \frac{\partial^2 u}{\partial x^2} + \frac{\partial^2 u}{\partial y^2} = 0 \quad \text{in the domain} \tag{13}$$

$$u(x, y)|_{\Gamma} = g_1(\Gamma) \quad \text{on the boundary} \tag{14}$$

$$\left.\frac{\partial u}{\partial n}\right|_{\Gamma} = g_2(\Gamma) \quad \text{on the boundary} \tag{15}$$

The traditional finite difference method and variable grid finite difference method under different circumstances are explained in the following sections.

2.4.1 Traditional Finite Difference Method

The main algorithm of traditional finite different method is to describe the relationship among potentials at adjacent nodes by Taylor series. The example of a two dimension node (x, y) and the adjacent node (x_0, y_0) is shown below [50].

$$\begin{aligned}\varphi(x,y) = \varphi_0 &+ \left[(x-x_0)\left(\frac{\partial\varphi}{\partial x}\right)_0 + (y-y_0)\left(\frac{\partial\varphi}{\partial y}\right)_0\right] \\ &+ \frac{1}{2}\left[(x-x_0)^2\left(\frac{\partial^2\varphi}{\partial x^2}\right)_0 + 2(x-x_0)(y-y_0)\left(\frac{\partial^2\varphi}{\partial x\partial y}\right)_0 + (y-y_0)^2\left(\frac{\partial^2\varphi}{\partial y^2}\right)_0\right]\end{aligned} \tag{16}$$

Since the accuracy requirement is set as the second order, Equation 8 can be simplified as below,

$$\varphi(x,y) = \varphi_0 + (x-x_0)(\frac{\partial\varphi}{\partial x})_{x=x_0} \tag{17}$$

In the equation, the subscript 0 represents (x_0, y_0) and the potential φ_0 can be calculated by the average potential values of four adjacent nodes. The relationship among potentials of these nodes is shown as follows [50]:

$$\varphi(x_0+h,y) = \varphi(x_0) + h\frac{\partial\varphi}{\partial x}|_{x=x_0} + \frac{h^2}{2}\frac{\partial^2\varphi}{\partial x^2}|_{x=x_0} \tag{18}$$

$$\varphi(x_0-h,y) = \varphi(x_0) - h\frac{\partial\varphi}{\partial x}|_{x=x_0} + \frac{h^2}{2}\frac{\partial^2\varphi}{\partial x^2}|_{x=x_0} \tag{19}$$

Therefore,

$$\frac{\partial^2\varphi}{\partial x^2} = \frac{\varphi(x+h,y) + \varphi(x-h,y) - 2\varphi(x,y)}{h^2} \tag{20}$$

$$\frac{\partial^2 \varphi}{\partial y^2} = \frac{\varphi(x, y+h) + \varphi(x, y-h) - 2\varphi(x, y)}{h^2} \tag{21}$$

In traditional FDM, the step of grid h is considered as one. The field domain in differential format is:

$$\begin{aligned} \nabla^2 u &= \frac{\partial^2 u}{\partial x^2} + \frac{\partial^2 u}{\partial y^2} \\ &= \varphi(x+h, y) + \varphi(x-h, y) + \varphi(x, y+h) + \varphi(x, y-h) - 4\varphi(x, y) = 0 \end{aligned} \tag{22}$$

2.4.2 Finite Difference Method on the Interface between Different Media

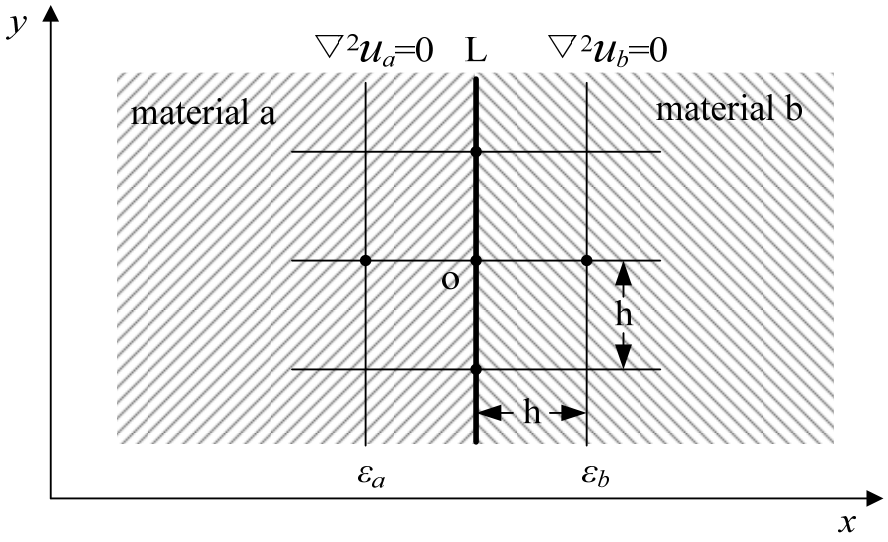

Figure 5. The Grid Schematic on the Interface between Two Different Materials

In Figure 5, the interface L is the boundary between two materials which have the different permittivity of ε_a and ε_b. In order to develop the potential relationship at five nodes, two equations are given below [50],

$$\varphi_a(x+h, y) + \varphi_a(x-h, y) + \varphi_a(x, y+h) + \varphi_a(x, y-h) - 4\varphi_a(x, y) = 0 \tag{23}$$

$$\varphi_b(x+h, y) + \varphi_b(x-h, y) + \varphi_b(x, y+h) + \varphi_b(x, y-h) - 4\varphi_b(x, y) = 0 \tag{24}$$

To keep the potential continuity on the interface,

$$\begin{aligned}\varphi_b(x,y) &= \varphi_a(x,y) = \varphi(x,y)\\ \varphi_b(x,y+h) &= \varphi_a(x,y+h) = \varphi(x,y+h)\\ \varphi_b(x,y-h) &= \varphi_a(x,y-h) = \varphi(x,y-h)\end{aligned} \tag{25}$$

To keep the charge density continuity on the interface,

$$\varepsilon_a \frac{\partial U_a}{\partial n} - \varepsilon_b \frac{\partial U_b}{\partial n} = \sigma \tag{26}$$

Differential format of Equation 25 is:

$$\varepsilon_a \frac{\varphi_a(x-h,y) - \varphi_a(x+h,y)}{h} - \varepsilon_b \frac{\varphi_b(x-h,y) - \varphi_b(x+h,y)}{h} = \sigma \tag{27}$$

σ is charge density on the interface of two materials [51]:

$$\sigma = \int \frac{I(t)}{S} dt = \frac{1}{j\omega S} \frac{[\varphi(x,y+h) - \varphi(x,y)] - [\varphi(x,y) - \varphi(x,y-h)]}{R} \tag{28}$$

where $I(t)$ is the leakage current and R is the surface resistance (Ω) and S is the surface area (m^2).

$$R = \int_{y-h}^{y} \frac{1}{2\pi r K_s} dl \tag{29}$$

$$S = \int_{y-h}^{y+h} \pi r dl \tag{30}$$

where K_s is the surface conductivity and r is the insulator radius.

Equivalent Salt Deposit Density (mg/cm^2) (ESDD) is used as the standard to describe the pollution severity on the insulator surface. The surface conductivity K_s is calculated by the empirical formula below [21],

$$K_s = \frac{\sqrt[1.03]{\frac{ESDD}{Vol}} A}{5.7} \tag{31}$$

where Vol is the volume of the distilled water (cm^3) and A is the insulator surface area in the empirical formula (cm^2).

Therefore, the potential relationship on the boundary in differential format is:

$$\begin{aligned}&\frac{2\varepsilon_b}{\varepsilon_a+\varepsilon_b}\varphi(x+h,y)+\frac{2\varepsilon_a}{\varepsilon_a+\varepsilon_b}\varphi(x-h,y)+(1+\frac{h}{j\omega SR(\varepsilon_a+\varepsilon_b)})\varphi(x,y+h)\\&+(1+\frac{h}{j\omega SR(\varepsilon_a+\varepsilon_b)})\varphi(x,y-h)-(4+2\frac{h}{j\omega SR(\varepsilon_a+\varepsilon_b)})\varphi(x,y)=0\end{aligned} \tag{32}$$

2.4.3 Variable Grid Finite Difference Method

In order to improve the storage efficiency and computation speed, the optimal finite difference method introduce in the variable grid of five points (Figure 6).

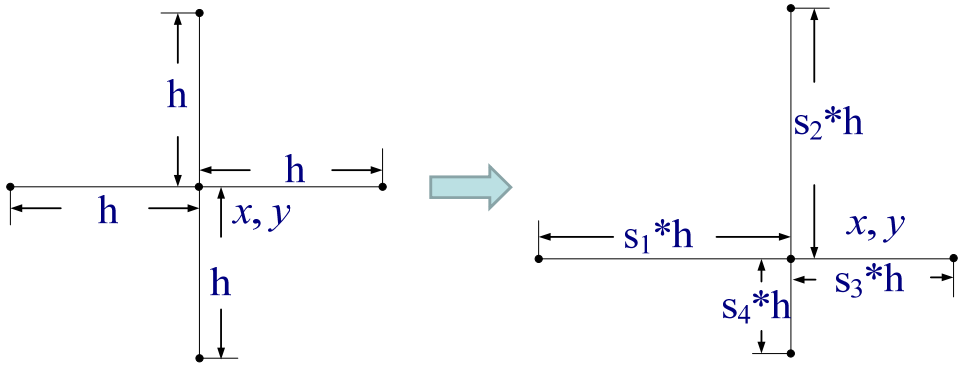

Figure 6. The Variable Grid Schematic of Five Points in Differential Format

In Figure 6, the Taylor equations between nodes can be modified as follows,

$$\begin{aligned}\varphi(x-s_1h,y)&=\varphi-(s_1h)\frac{\partial\varphi}{\partial x}+\frac{(s_1h)^2}{2}\frac{\partial^2\varphi}{\partial x^2}-\frac{(s_1h)^3}{6}\frac{\partial^3\varphi}{\partial x^3}+\ldots\\\varphi(x+s_3h,y)&=\varphi+(s_3h)\frac{\partial\varphi}{\partial x}+\frac{(s_3h)^2}{2}\frac{\partial^2\varphi}{\partial x^2}+\frac{(s_3h)^3}{6}\frac{\partial^3\varphi}{\partial x^3}+\ldots\\\varphi(x,y+s_2h)&=\varphi+(s_2h)\frac{\partial\varphi}{\partial y}+\frac{(s_2h)^2}{2}\frac{\partial^2\varphi}{\partial y^2}+\frac{(s_2h)^3}{6}\frac{\partial^3\varphi}{\partial y^3}+\ldots\\\varphi(x,y-s_4h)&=\varphi-(s_4h)\frac{\partial\varphi}{\partial y}+\frac{(s_4h)^2}{2}\frac{\partial^2\varphi}{\partial y^2}-\frac{(s_4h)^3}{6}\frac{\partial^3\varphi}{\partial y^3}+\ldots\end{aligned} \tag{33}$$

Then, the field domain is discretized below,

$$\begin{aligned}\frac{\partial^2 u}{\partial x^2}+\frac{\partial^2 u}{\partial y^2} &= \varphi(-\alpha_0+\alpha_1+\alpha_2+\alpha_3+\alpha_4)\\ &+\frac{\partial u}{\partial x}(\alpha_1 s_1 h-\alpha_3 s_3 h)+\frac{\partial u}{\partial y}(\alpha_2 s_2 h-\alpha_4 s_4 h)\\ &+\frac{1}{2}\frac{\partial^2 u}{\partial x^2}(\alpha_1(s_1 h)^2+\alpha_3(s_3 h)^2)+\frac{1}{2}\frac{\partial^2 u}{\partial y^2}(\alpha_2(s_2 h)^2+\alpha_4(s_4 h)^2)\\ &+\frac{1}{6}\frac{\partial^3 u}{\partial x^3}(\alpha_1(s_1 h)^3-\alpha_3(s_3 h)^3)+\frac{1}{6}\frac{\partial^3 u}{\partial y^3}(\alpha_2(s_2 h)^3-\alpha_4(s_4 h)^3)\end{aligned} \tag{34}$$

The coefficients are compared in Equation 35:

$$\begin{cases}-\alpha_0+\alpha_1+\alpha_2+\alpha_3+\alpha_4=0\\ \alpha_1 s_1 h-\alpha_3 s_3 h=0\\ \alpha_2 s_2 h-\alpha_4 s_4 h=0\\ \alpha_1(s_1 h)^2+\alpha_3(s_3 h)^2=2\\ \alpha_2(s_2 h)^2+\alpha_4(s_4 h)^2=2\end{cases} \tag{35}$$

$$\Rightarrow\begin{cases}\alpha_0=2[\frac{1}{s_1 s_3 h^2}+\frac{1}{s_2 s_4 h^2}]\\ \alpha_1=\frac{2}{s_1 h(s_1 h+s_3 h)}\\ \alpha_2=\frac{2}{s_2 h(s_2 h+s_4 h)}\\ \alpha_3=\frac{2}{s_3 h(s_1 h+s_3 h)}\\ \alpha_4=\frac{2}{s_4 h(s_2 h+s_4 h)}\end{cases} \tag{36}$$

Therefore, the potential relationship on the boundary in differential format is:

$$\alpha_0 u(i,j)=\alpha_1 u(i+1,j)+\alpha_2 u(i-1,j)+\alpha_3 u(i,j+1)+\alpha_4 u(i,j-1) \tag{37}$$

As all the equations are achieved, the sparse coefficient matrix P is constructed and the known boundary condition values on the nodes are set as V matrix.

$$\begin{bmatrix}P_{11} & \cdots & P_{1i}\\ \vdots & \ddots & \\ P_{i1} & \cdots & P_{ii}\end{bmatrix}\begin{bmatrix}\varphi_1\\ \vdots\\ \varphi_i\end{bmatrix}=\begin{bmatrix}V_1\\ \vdots\\ V_i\end{bmatrix} \tag{38}$$

Since both matrix P and V are sparse, the potential matrix φ is solved by lower upper (LU) decomposition method. The efficiency increases significantly, when

compared with traditional finite difference method, which use great number of iterations to achieve the potential values.

In addition, the matrix element number of variable grid FDM is considerably less than that of traditional FDM. For example, in order to calculate the potential at node X in Figure 7(a), the traditional method needs to calculate the potential of all the nodes in the domain. In contrast, the variable grid finite difference method only requires the potential values of four nodes on the boundary (Figure 7(b)).

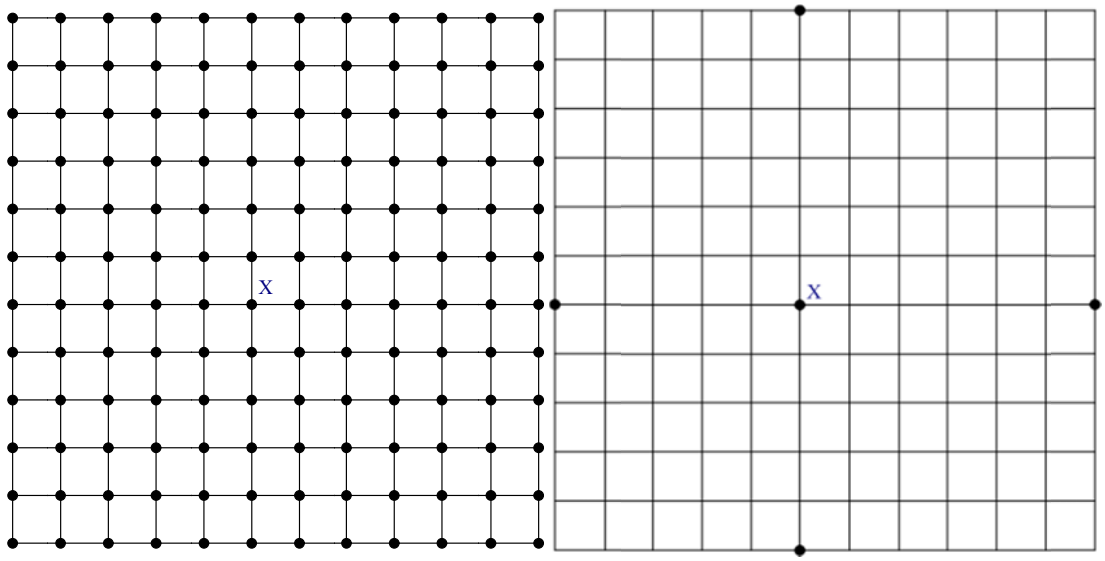

(a) The Traditional FDM Requires the Values of All the Points

(b) The Traditional FDM Requires the Values of Four Points on the Boundary

Figure 7. The Comparison between Traditional and Variable Grid Finite Difference Method

The error between traditional method and variable grid method is shown as follows:

$$\begin{aligned} Error &= \frac{1}{6}\frac{\partial^3 u}{\partial x^3}(\alpha_1(s_1h)^3 - \alpha_3(s_3h)^3) + \frac{1}{6}\frac{\partial^3 u}{\partial y^3}(\alpha_2(s_2h)^3 - \alpha_4(s_4h)^3) \\ &= \frac{1}{3}\frac{\partial^3 u}{\partial x^3}\left(\frac{(s_1h)^2}{s_1h+s_3h} - \frac{(s_3h)^2}{s_1h+s_3h}\right) + \frac{1}{3}\frac{\partial^3 u}{\partial y^3}\left(\frac{(s_2h)^2}{s_2h+s_4h} - \frac{(s_4h)^2}{s_2h+s_4h}\right) \\ &= \frac{1}{3}\frac{\partial^3 u}{\partial x^3}(s_1h - s_3h) + \frac{1}{3}\frac{\partial^3 \boldsymbol{u}}{\partial y^3}(s_2h - s_4h) \end{aligned} \tag{39}$$

From Equation (39), it can be seen that the error increases when the position of the point is near the boundary. The potential error between traditional FDM and variable-grid FDM is calculated in Equation 40.

$$Error\_ratio = \left\| \frac{V_{TF} - V_{VF}}{V_{TF}} \right\| \tag{40}$$

where V_{TF} and V_{VF} are the potentials at all the points of traditional FDM and Variable-grid FDM respectively. *Error_Ratio* is the 2-norm of the error ratios at all the points in the field domain.

The error distribution results in the field domain are shown in Figure 8. The dimension of square area model (Figure 8) is 1001×1001.

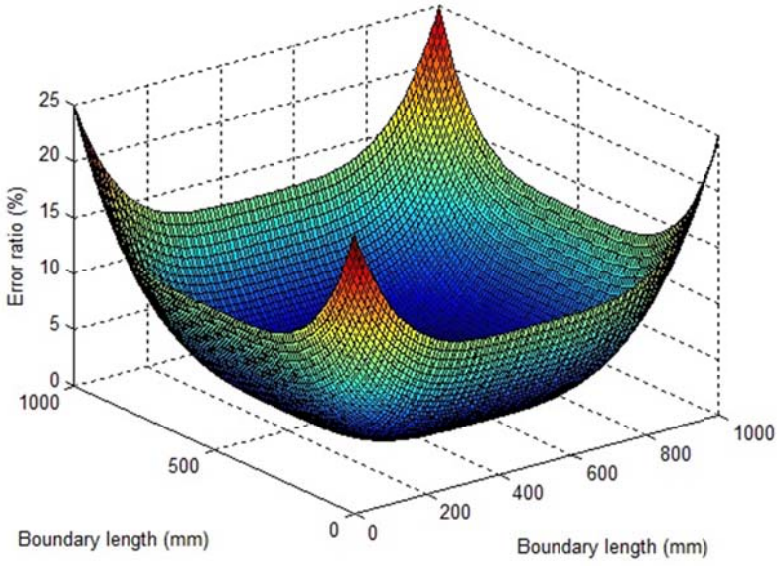

Figure 8. The Error Ratio Distribution in the Field Domain

The potential error between traditional FDM and variable-grid FDM is calculated at different ratio of distance to boundary over grid length. The fitting curve is shown in Figure 9.

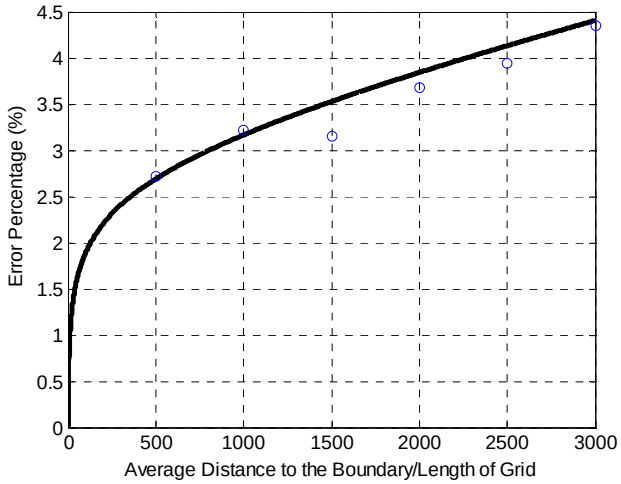

Figure 9. Relationship between Errors and the Ratio of Boundary Length over Grid Length.

3 FLASHOVER MODELS

Many researchers have made great amount of contributions to improve the flashover models. Obenaus and Neumarker started the modeling of flashover with a mathematic expression. Afterwards, Rizk reviewed the mathematical models for pollution flashover and proposed a flashover equation for AC voltage [6]. In 1858, Jolly, Cheng and Otten firstly considered the instantaneous arc parameters and gave dynamic model of arc propagation [7]. All the models above are discussed in the first section of Chapter 3. As flashover is a stochastic process, a new theoretic model is proposed by combining numerical electric field calculation with Random Walk Theory.

3.1 Review of Previous Flashover Models

The schematic of most mathematical models used to predict the flashover voltage of polluted insulators is shown in Figure 10.

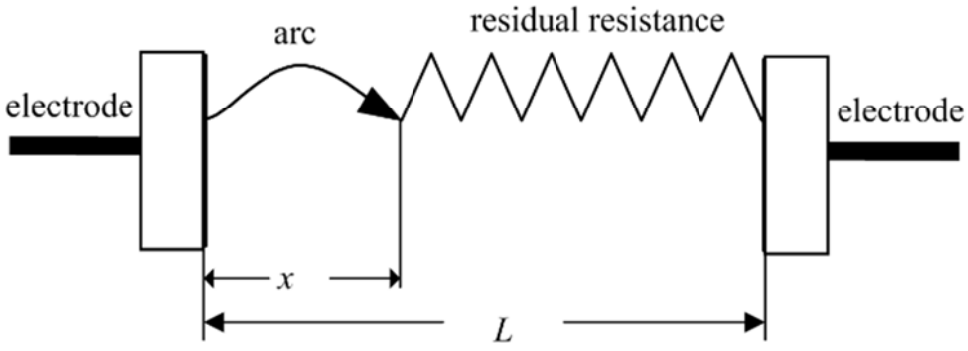

Figure 10. The Fundamental Model of Flashover Circuit

This mathematical model aims at predicting the propagation process of the arc on polluted insulators. The critical voltage to maintain the arc propagation can be

deduced from Equation 41.

$$U = AxI^{-n} + R_p I \tag{41}$$

Where U (V) is the peak value of the applied voltage, x (cm) is the arc length, I (A) is the peak value of the arc current, R_p (Ω) is the resistance of the remaining pollution layer, and A, n are the arc characteristic constants. [52]

Rizk developed the relationship between the arc conductivity and energy. The arc reignition condition can be deduced as [11]:

$$U_m = \frac{2080x}{i_m} \tag{42}$$

Where x (cm) is the arc length, i_m (A) is the peak value of the leakage current, and U_m (V) is the peak value of the applied voltage.

The Hampton criterion is the existing criterion to determine dynamic arc propagation. The further propagation depends on whether the electric field of the pollution layer (E_p) is greater than that of arc gradient (E_{arc}). The electric field for arc and pollution layer is calculated below:

$$E_{arc} = AI^{-n} \tag{43}$$

$$E_p = R_p I \tag{44}$$

Where I (A) is the peak value of the arc current, R_p (Ω) is the resistance of the remaining contamination layer, and A, n are the arc characteristic constants.

By increasing the supply voltage or pollution severity, the leakage current will increase to a level so that $E_{arc} < E_p$ and arc starts to propagation. It can be seen that the

E_{arc} will keep decreasing and E_p will keep increasing during arc propagation process, which means once arc initializes, it cannot stop until flashover occurs [53].

3.2 New Flashover Model Based on Random Walk Theory

A two-dimension stochastic model of flashover around the insulators has been developed. The arc growth is described by a stochastic propagation of the channel structure on the insulator surface as well as in the air. The channel growth is driven by the instantaneous electric field.

Random Walk is a mathematical formalization of a path that consists of a succession of random steps [54]. Assume a particle P executing a random walk on a two-dimension integer lattice, length of each random step is determined by the magnitude of electric field vectors to the directions.

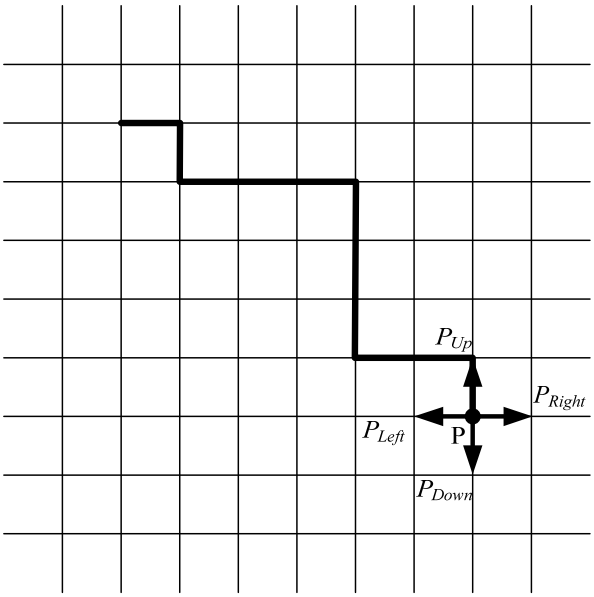

Figure 11. The Random Walk Process of Particle P

In this study, an ensemble of four possible directions is used for simulation (Figure 9). The position of the new point is selected stochastically from the possible

positions with the probability P, which is determined by the square of the potential difference φ between the possible position and the growth point. The arc energy is also considered as a criterion for arc propagation. The law of growth probability is given by [55]

$$P = \frac{(\Delta\varphi)^2}{\sum(\Delta\varphi)^2}\theta(\Delta\varphi - E_c d)\theta(W - W_t) \tag{45}$$

Where $\sum(\Delta\varphi)^2$ is the summation made over all possible attachment positions providing $\Delta\varphi > E_c d$ and E_c is the dielectric strength of the material. The W is the arc energy and W_t is the threshold energy in air. $\theta(x)$ is the step function:

$$\theta(x) = \begin{cases} 0 & x < 0 \\ 1 & x \geq 0 \end{cases} \tag{46}$$

Specifically, when $\Delta\varphi > E_c d$,

$$P_{Up} = \frac{E_{Up}^2}{E_{Up}^2 + E_{Down}^2 + E_{Left}^2 + E_{Right}^2} \tag{47}$$

$$P_{Down} = \frac{E_{Down}^2}{E_{Up}^2 + E_{Down}^2 + E_{Left}^2 + E_{Right}^2} \tag{48}$$

$$P_{Left} = \frac{E_{Left}^2}{E_{Up}^2 + E_{Down}^2 + E_{Left}^2 + E_{Right}^2} \tag{49}$$

$$P_{Right} = \frac{E_{Right}^2}{E_{Up}^2 + E_{Down}^2 + E_{Left}^2 + E_{Right}^2} \tag{50}$$

If the electric field is less than the dielectric strength of air or the arc reaches the ground electrode and completes the flashover, the arc propagation stops. When the arc grows to ground electrode, it is assumed that the arc has enough energy to complete

the flashover [56].

The flashover probability is calculated by the equation below.

$$P_{flashover} = \frac{N_A}{N_T} \tag{51}$$

where N_A represents the number of arcs that completes the flashover and N_T is the total number of arc propagation processes.

In order to calculate the flashover probability, a certain number of arc propagation processes are repeated. The number of arc propagation iterations is determined by the variance of flashover probability.

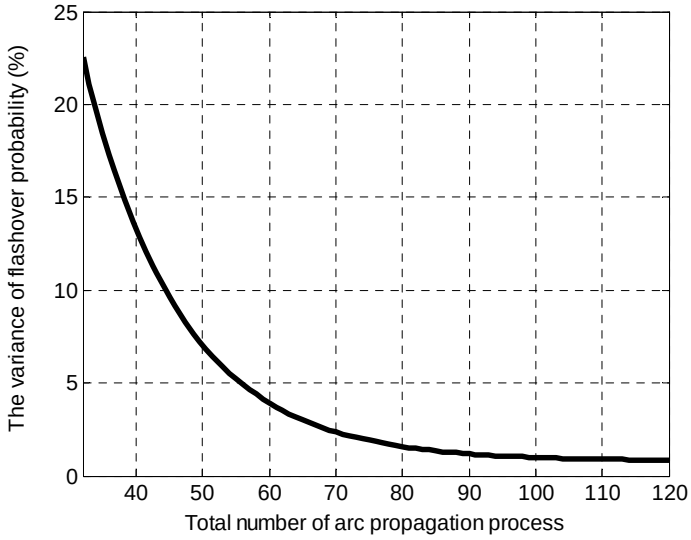

Figure 12. The Variance of Flashover Probability versus Number of Arc Propagation Processes

Figure 12 shows that the variance of flashover probability reduces significantly as the number of arc propagation iterations increases from 30 to 120. When the total number of arc propagations is larger than 100, the improvement of probability accuracy is less than 0.5%. Therefore, the number of arc propagations is set as 110.

The arc energy consists of two parts: capacitive energy and resistive energy (Figure 13).

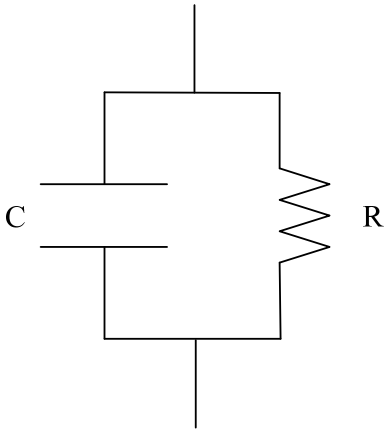

Figure 13. Capacitive and Resistive Properties of the Insulator

In Figure 13, the capacitive energy is the RMS value of the energy contained in the capacitor C. The capacitance is calculated as follows,

$$C = \frac{\varepsilon_r \varepsilon_0 S}{L} \tag{52}$$

where L is the dry arc distance of the insulator, S is the area of the electrode, ε_r is the relative permittivity and ε_0 is the electric constant.

Since the supply voltage is,

$$V = V_m \cos(\omega t + \delta) \tag{53}$$

where V_m is the maximum voltage and ω is angular frequency.

The current is.

$$I = C\frac{dV(t)}{dt} = -V_m C\omega \sin(\omega t + \delta) \tag{54}$$

Therefore, the capacitive energy is,

$$W_c = \int P(t)dt = -\int \frac{V_m^2 \omega C \sin(2\omega t + 2\delta)}{2} dt = \frac{V_m^2 C \cos(2\omega t + 2\delta + \pi)}{4} \tag{55}$$

The RMS value of the capacitive energy,

$$W_{cRMS} = \frac{V_m^2 C}{4\sqrt{2}} \tag{56}$$

During arc propagation, the arc creates a conductive path on the insulator surface and therefore, the effective resistance of the insulator reduces. The surface charge is calculated below,

$$q(x,y) = \int I(t)dt = \frac{1}{j\omega}\frac{[\varphi(x,y+h)-\varphi(x,y)]-[\varphi(x,y)-\varphi(x,y-h)]}{R} \tag{57}$$

where $I(t)$ is the leakage current and R is the surface resistance (Ω).

The resistive arc energy is consumed in the air during arc propagation and also supplemented due to the increase of leakage current.

$$W_R = \int_0^L V(x,y)q(x,y)dl \tag{58}$$

where L is the leakage distance.

Since the main constituent part of air is nitrogen, the air ionization energy is 1402.3 kJ/mol. The molar volume of ideal gas is 22.414 L/mol. Therefore, the ionization energy to keep arc propagation in two dimensional plane 62.56 J/cm.

The flowchart shown in Figure 14 explains the iteration process of arc propagation as well as the probability calculation of flashover and arc jumping between sheds.

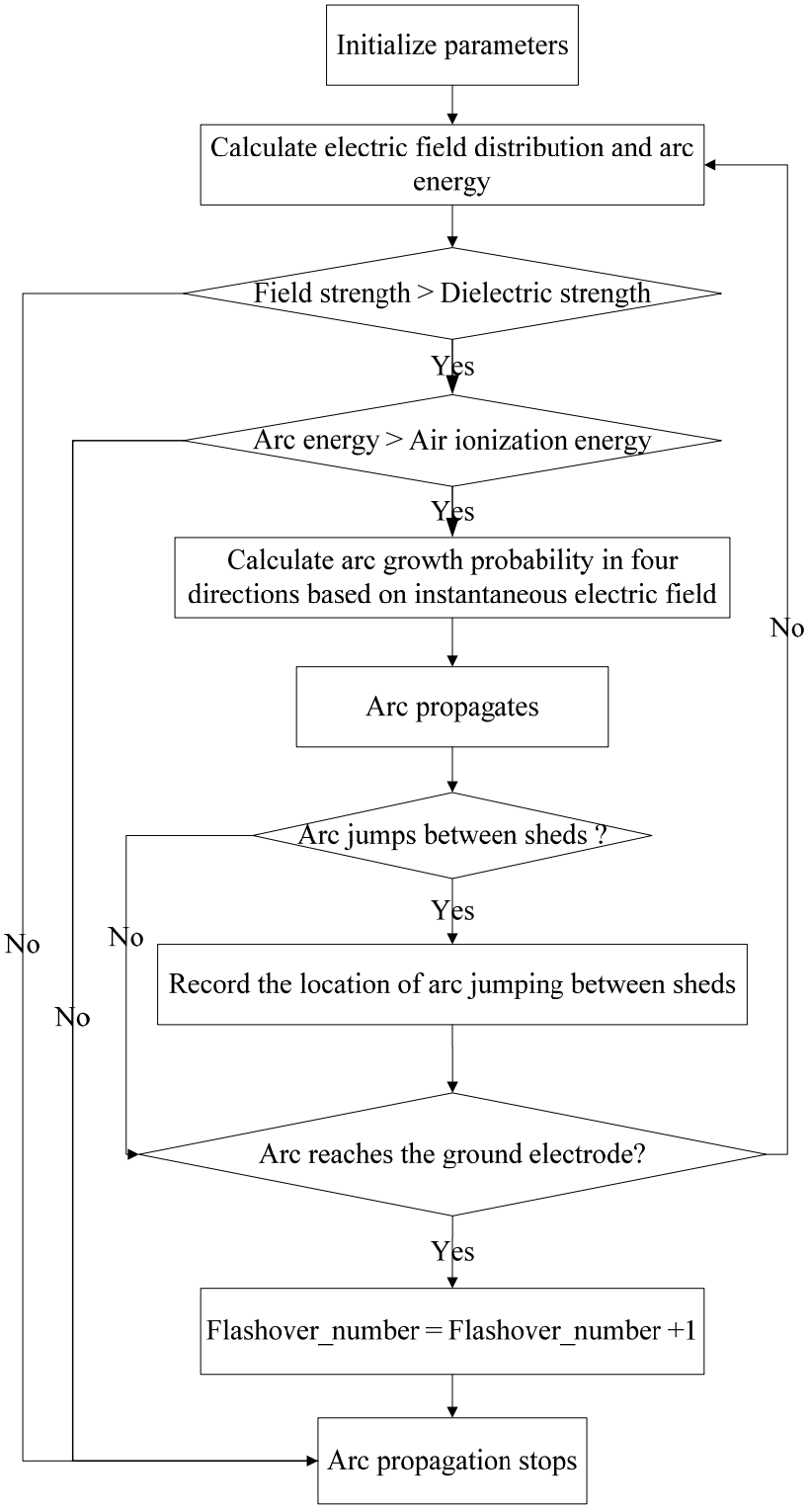

Figure 14. The program flowchart

4 ARC PROPAGATION ANALYSIS

This chapter is divided into five sections. The first section describes the dimension of the insulator model. The second section provides the electric field distribution before arc initialization and detailed arc propagation process. It can be seen that the probabilities of flashover and arc jumping between sheds are mainly impacted by two factors: supply voltage and ESDD values. The third section presents the simulation results under four different conditions (Table 3). The fourth section compares the results and gives the regression model to evaluate the effects of two factors. The fifth section gives the 50% flashover voltage as a function of ESDD values.

Table 3. Four Different Simulation Conditions

Case Number	Supply Voltage (kV)	ESDD (mg/cm^2)
1	70	0.02
2	70	0.5
3	138	0.02
4	138	0.5

4.1 The Structure of Simulation Model

The insulator in this report is modeled as a cylindrical rod with ten sheds and two electrodes. The length of insulator is 1080 mm. The structure of the insulator model is shown in Figure 15.

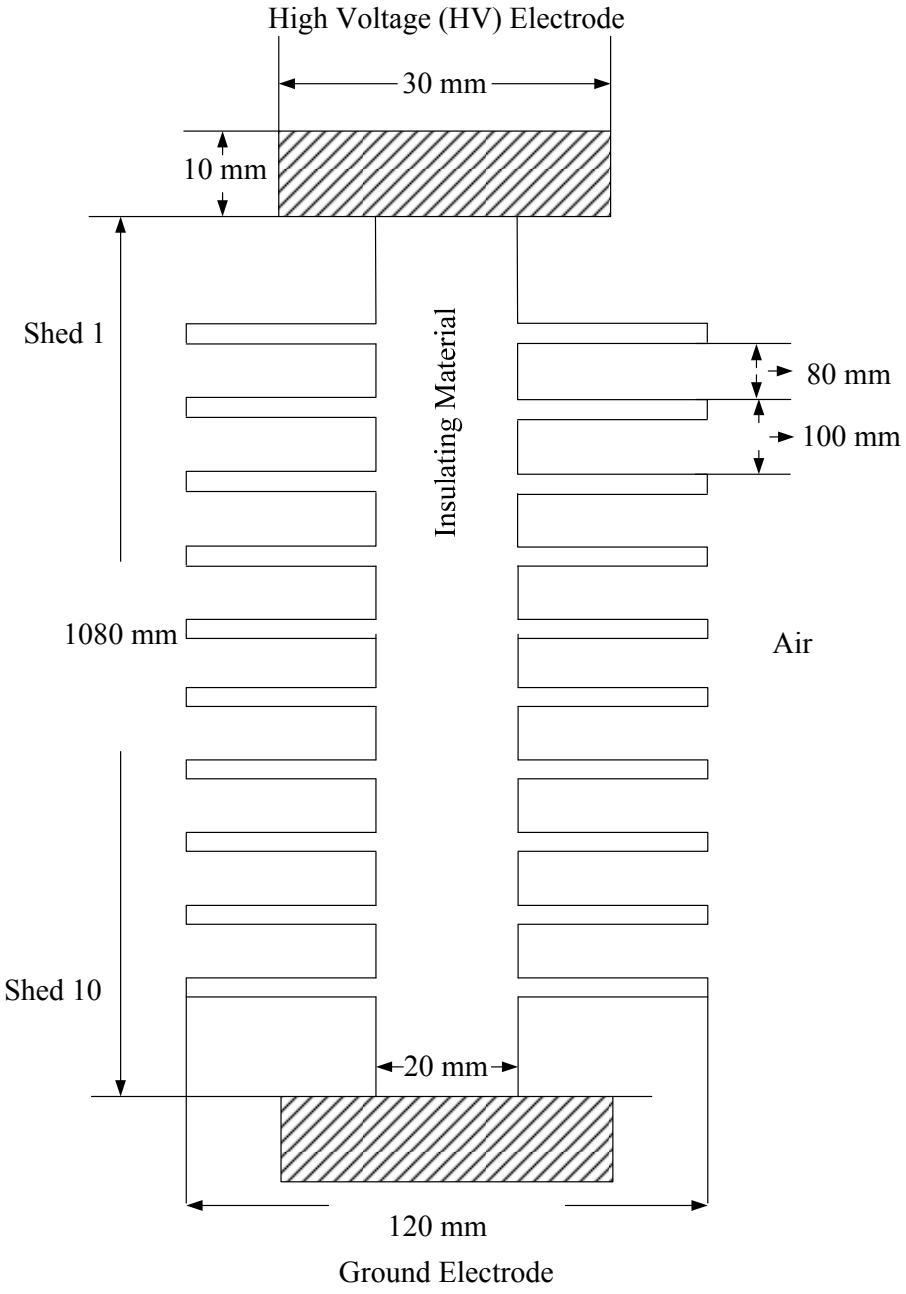

Figure 15. The Structure of Insulator Model

4.2 Detailed Arc Propagation Process

4.2.1 Electric Field Distribution versus Various ESDD Values

The voltage is set as 70 kV. Both horizontal and vertical electric field distributions before arc initialization are simulated with three contamination levels.

- ESDD is set as 0.02 mg/cm^2

The vertical and horizontal electric field distributions in the domain around the insulator model are shown in Figures 16 and 17 respectively.

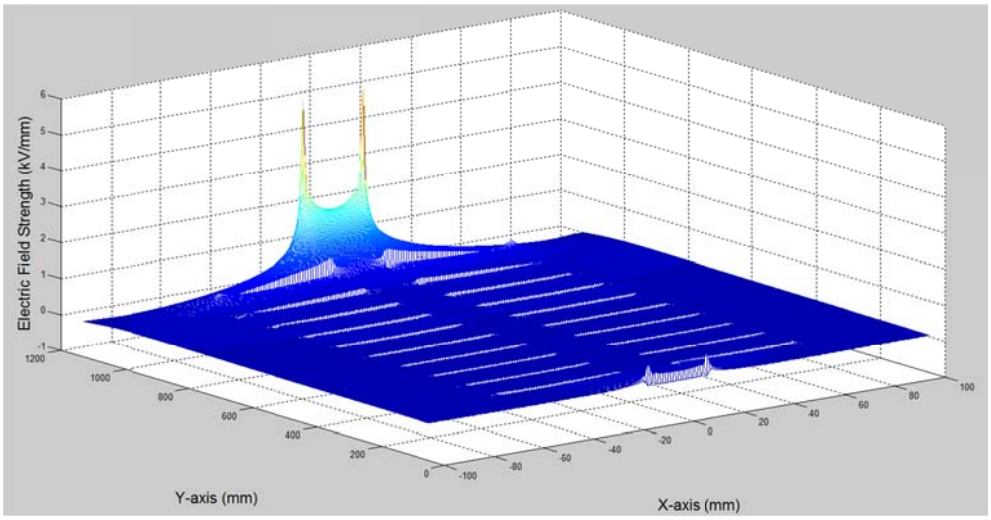

Figure 16. The Vertical Electric Field Distributions in 2D Domain

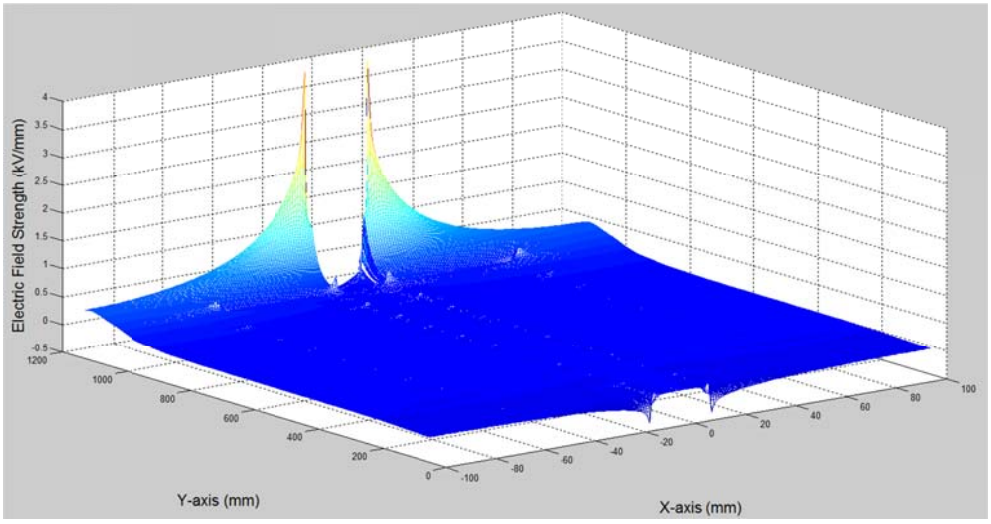

Figure 17. The Horizontal Electric Field Distributions in 2D Domain

In Figures 16 and 17, the maximum horizontal electric field strength is 4.615 kV/mm, the maximum vertical electric field is 3.679 kV/mm. It can be observed that both vertical and horizontal maximum electric field values are larger than dielectric strength of air (3 kV/mm). In addition, the vertical electric field is considerably larger than the horizontal electric field, which indicates that vertical electric field is the dominant factor to generate the arc under severe contamination conditions. The electric field distributions along dry arc distance and leakage distance are shown in Figures 18 and 19 respectively.

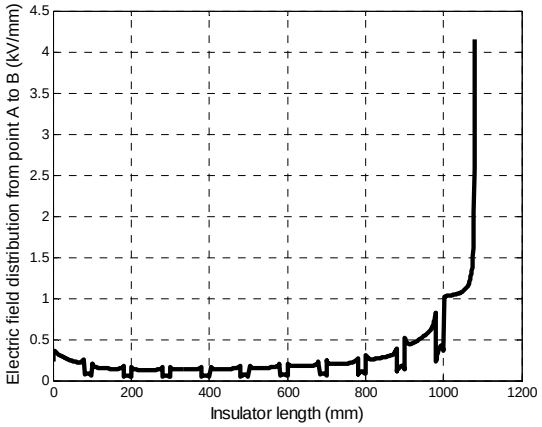

Figure 18. Electric Field Distribution along Dry Arc Distance

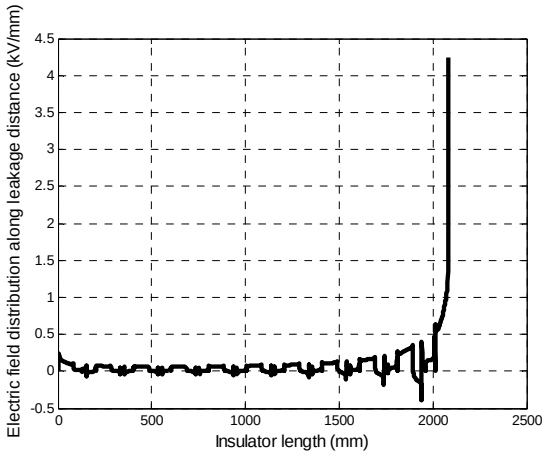

Figure 19. Electric Field Distribution along the Insulator Leakage Distance

- ESDD is set as 0.5 mg/cm^2

The vertical and horizontal electric field distributions in the domain around the insulator model are shown in Figures 20 and 21 respectively.

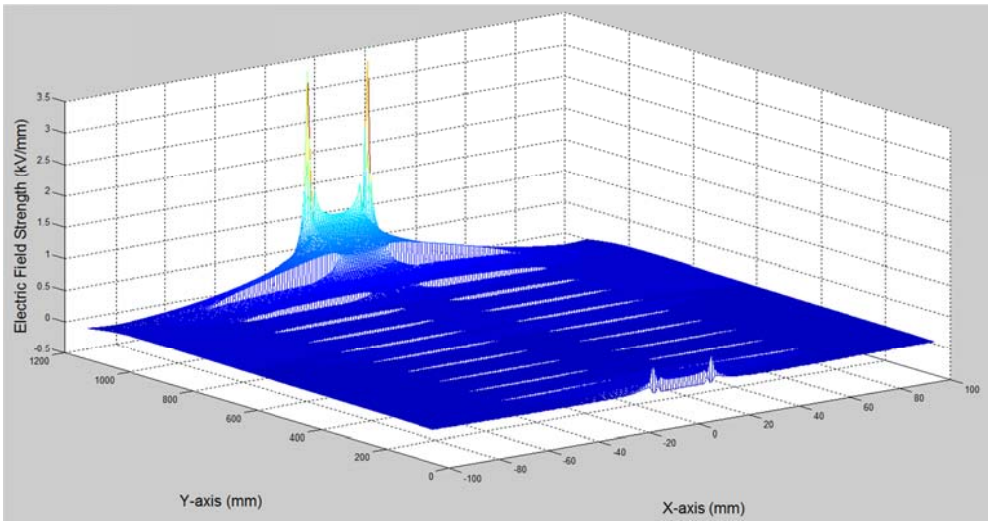

Figure 20. The Vertical Electric Field Distributions in 2D Domain

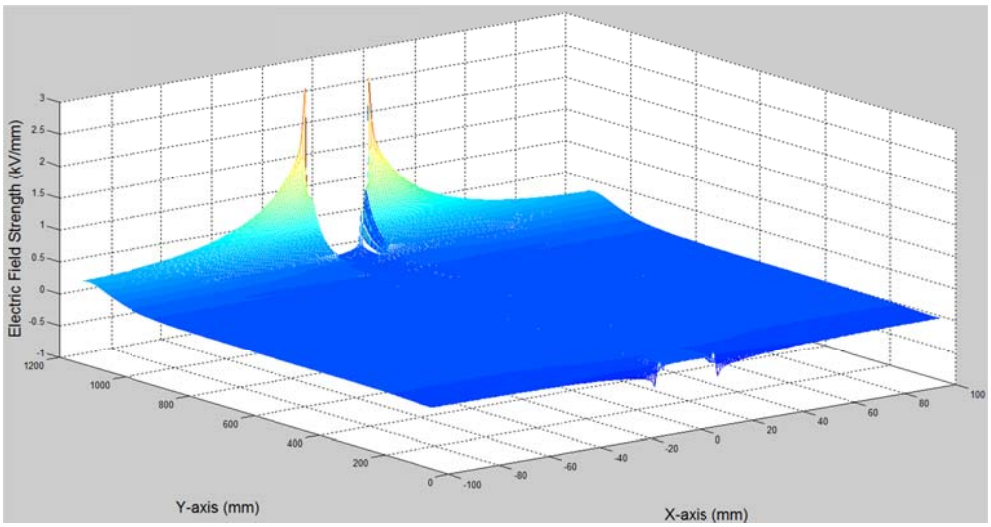

Figure 21. The Horizontal Electric Field Distributions in 2D Domain

In Figures 20 and 21, the maximum horizontal electric field strength is 2.534 kV/mm, and the maximum vertical electric field is 3.475 kV/mm. It can be observed that maximum vertical electric field value exceeds dielectric strength of air (3

kV/mm), while maximum horizontal electric field is less than dielectric strength of air. Therefore, the vertical electric field is the dominant factor to produce arc.

The electric field distributions along dry arc distance and leakage distance are shown in Figures 22 and 23 respectively.

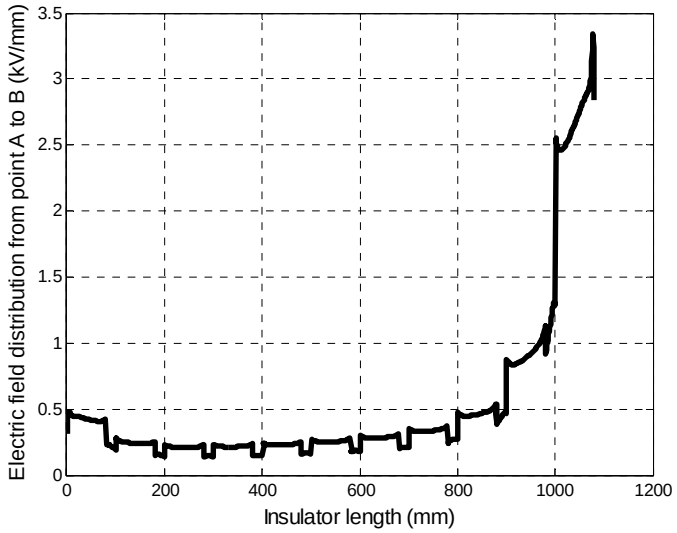

Figure 22. Electric Field Distribution along Dry Arc Distance

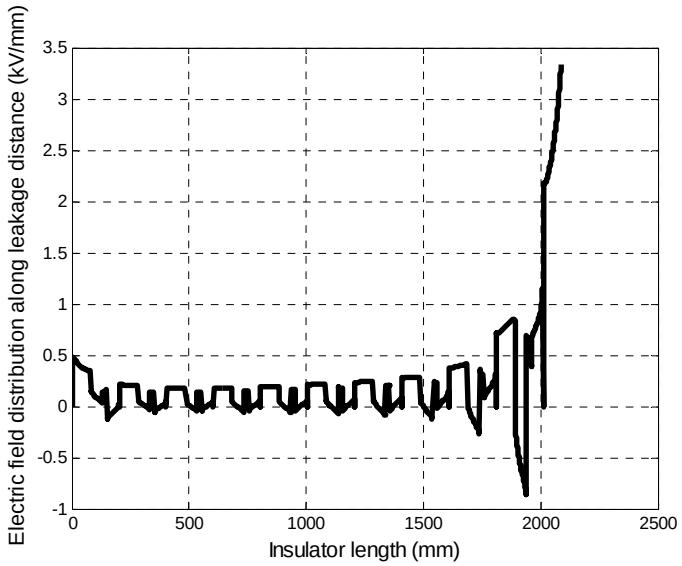

Figure 23. Electric Field Distribution along the Insulator Leakage Distance

- ESDD is 1 mg/cm^2

The vertical and horizontal electric field distributions in the domain around the insulator model are shown in Figures 24 and 25 respectively.

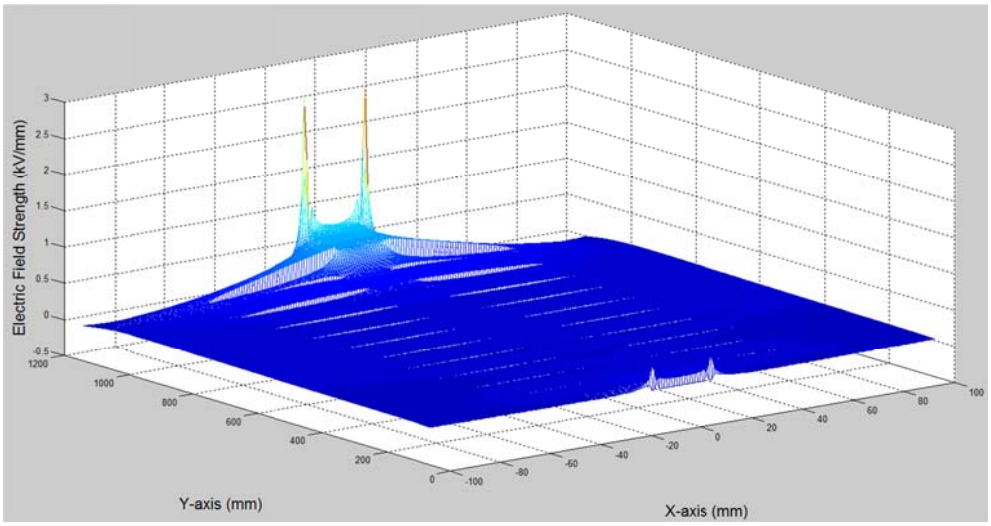

Figure 24. The Vertical Electric Field Distributions in 2D Domain

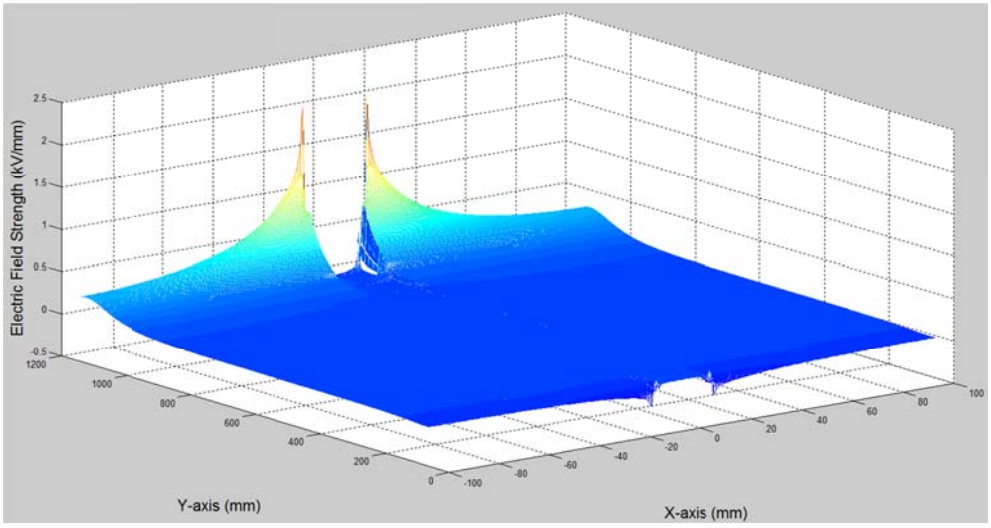

Figure 25. The Horizontal Electric Field Distributions in 2D Domain

In Figures 24 and 25, the maximum horizontal electric field strength is 1.893 kV/mm, and the maximum vertical electric field is 2.326 kV/mm. Both of these two values are lower than dielectric strength of air (3 kV/mm). Hence, arc is not able to ignite.

The electric field distributions along dry arc distance and leakage distance are shown in Figures 26 and 27 respectively.

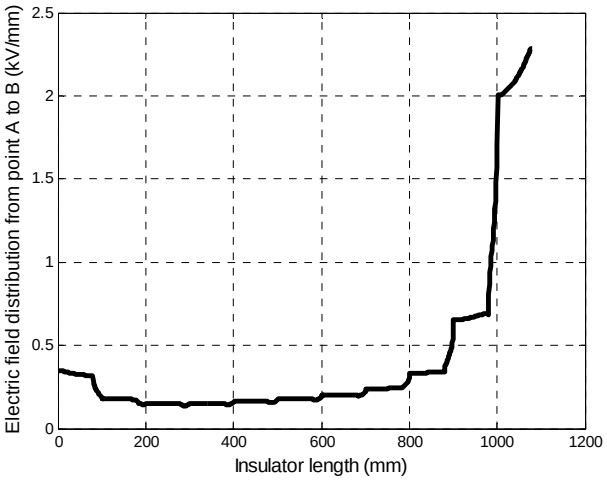

Figure 26. Electric Field Distribution along Dry Arc Distance

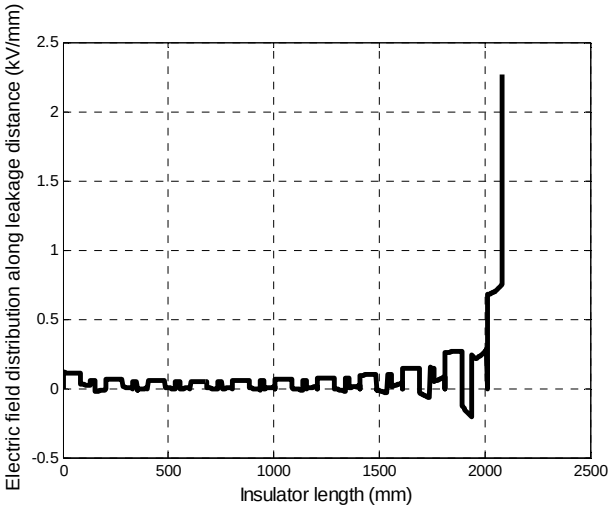

Figure 27. Electric Field Distribution Along the Insulator Leakage Distance

From three cases above, it can be concluded that the maximum electric field reduces with the ESDD increases. Therefore, maximum electric field is only to determine the arc ignition. The flashover performance is not dominated by maximum electric field.

4.2.2 Arc Propagation Process

As arc propagation is a stochastic phenomenon, an arc could travel on different paths based on the electric field distribution. Some arc paths jump between insulator sheds instead of travelling along the insulator surface. The arc jumping phenomena is shown in Figure 28. The stochastic arc propagation processes in the simulation model with and without arc jumping between sheds are shown in Figure 29(a) and (b) respectively.

Figure 28. Laboratorial Testing on the Contaminated Insulator Illustrating Arc Jumping Sheds. Bottom Electrode is HV Electrode and Top Electrode is Ground Electrode.

As the insulator model is simulated under four different conditions (Table 4), Case 2 is shown below as a demonstration to describe arc propagation process in detail. In order to show the process clearly, the instantaneous vertical electric field distribution are provided at six locations on the insulator surface, when arc reaches the

specific location. The voltage is set as 70 kV and ESDD is 0.5 mg/cm^2.

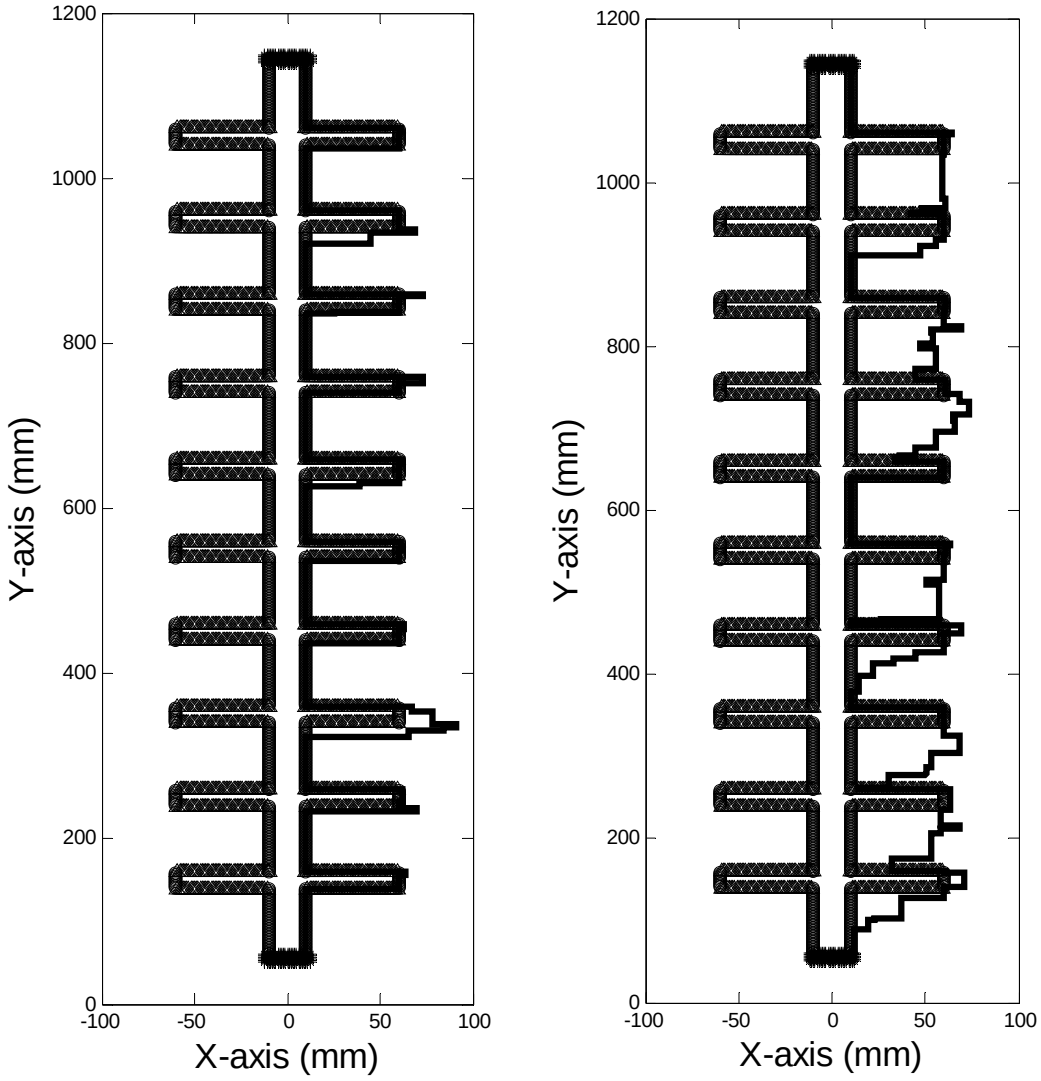

(a) Arc Travels along Insulator Surface (b) Arc Jumps between Sheds

Figure 29. Arc Propagation Process.

The following six locations of arc describe the detail arc propagation process when arc travels randomly in the air. In Table 4, "Field" shows the electric field vector to each direction. "Probability" shows the probability to each direction based on field calculation. "Prob_boundary" is the accumulated probability to determine the arc direction.

- Location 1: the arc reaches the location between shed 2 and 3.

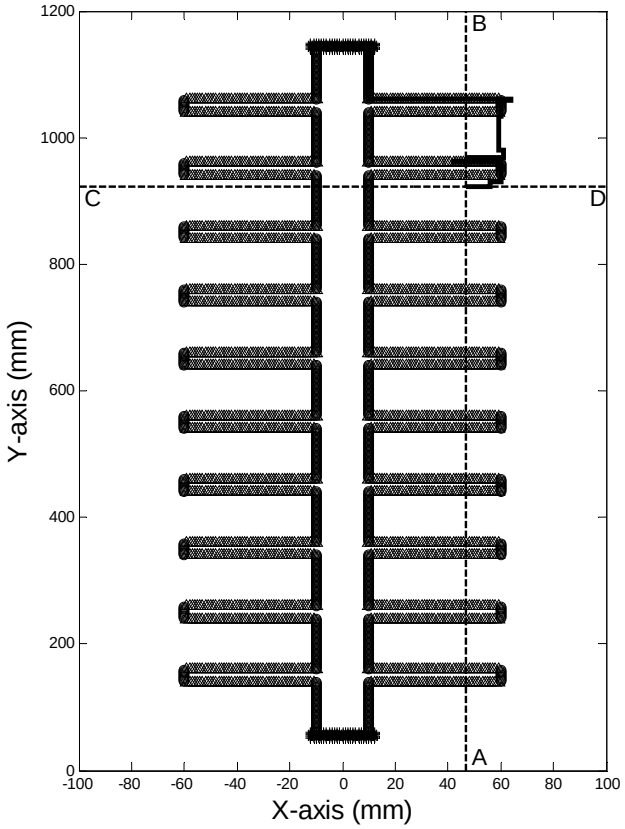

Figure 30. Arc Propagation Process of Location 1

Electric field to each direction and arc instant energy are shown in Table 4.

Table 4. Electric Field and Arc Instant Energy during Propagation

Possible Direction	Up	Down	Left	Right	Random Number	Energy (J/cm)
Field (kV/mm)	1.32	5.45	2.68	3.85	0.32	253.89>62.56
Probability	0.12	0.57	0.43	0		
Prob_boundary	0.12	0.69	1	1		
Arc Direction	Down (No stop)					

The vertical electric field distribution from point A to B (Figure 30) is shown in Figure 31. The horizontal electric field distribution from point C to D (Figure 28) is shown in Figure 32.

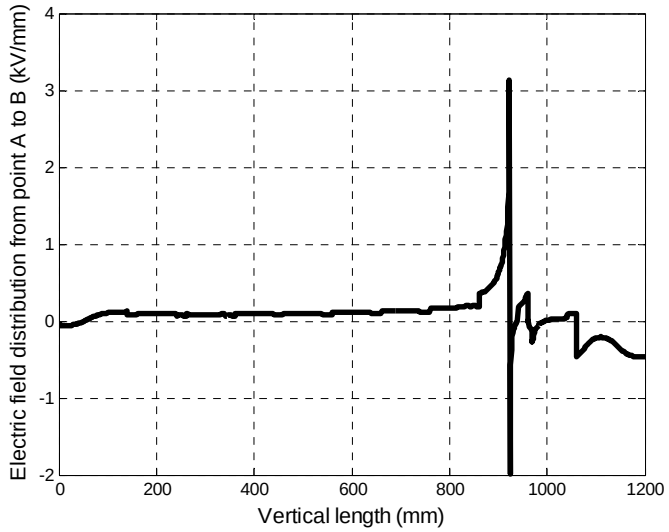

Figure 31. The Vertical Electric Field Distribution from Point A to B

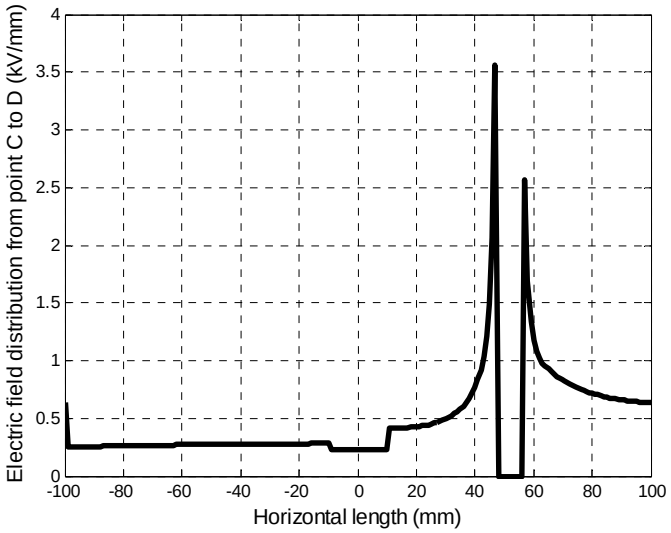

Figure 32. The Horizontal Electric Field Distribution from Point C to D

From Figures 31 and 32, it can be observed that maximum vertical and horizontal electric field is achieved at the leading end of the arc.

- Location 2: the arc reaches the location between shed 4 and 5.

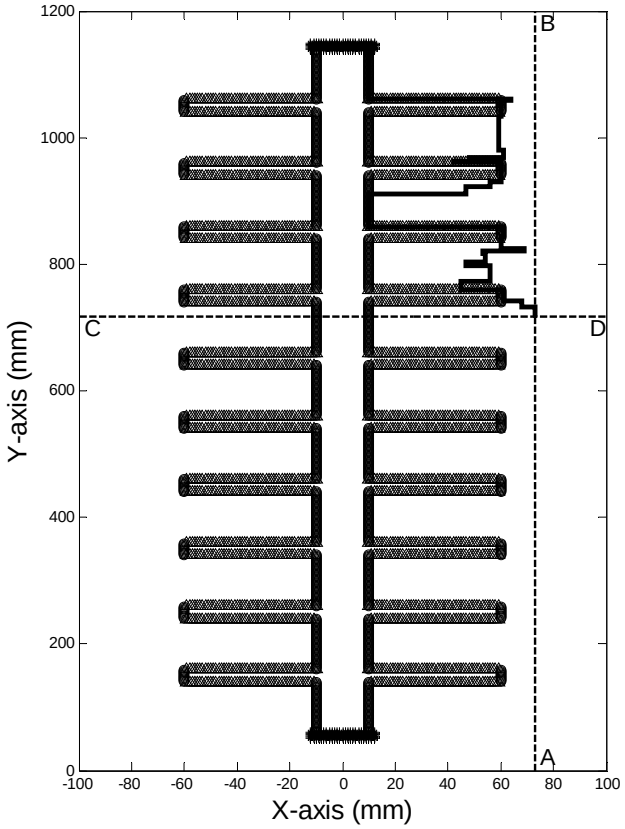

Figure 33. Arc Propagation Process of Location 2

Electric field to each direction and arc instant energy are shown in Table 6.

Table 5. Electric Field and Arc Instant Energy during Propagation

Possible Direction	Up	Down	Left	Right	Random Number	Energy (J/mm)
Field (kV/mm)	0	9.15	7.69	0	0.32	341.72>62.56
Probability	0	0.64	0.36	0		
Prob_boundary	0	0.64	1	1		
Arc Direction	Down (No stop)					

The vertical electric field distribution from point A to B (Figure 33) is shown in Figure 34. The horizontal electric field distribution from point C to D (Figure 33) is shown in Figure 35.

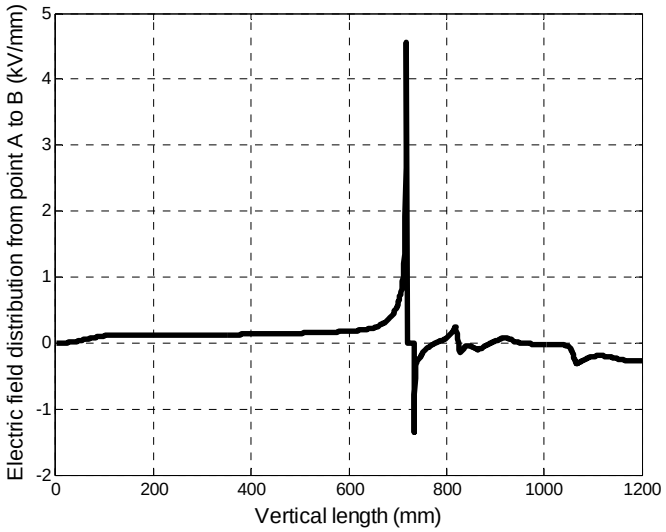

Figure 34. The Vertical Electric Field Distribution from Point A to B

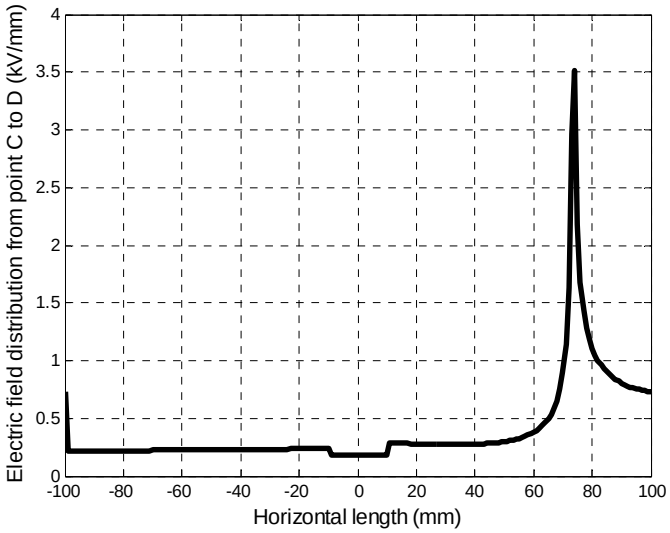

Figure 35. The Horizontal Electric Field Distribution from Point C to D

From Figures 34 and 35, it can be observed that maximum vertical and horizontal electric field is achieved at the leading end of the arc.

- Location 3: the arc reaches the location between shed 5 and 6.

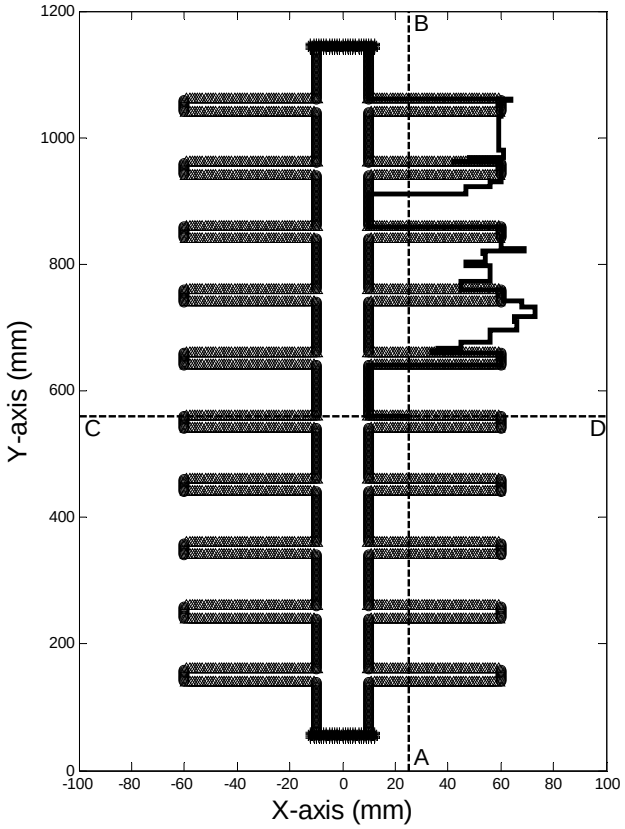

Figure 36. Arc Propagation Process of Location 3

Electric field to each direction and arc instant energy are shown in Table 6.

Table 6. Electric Field and Arc Instant Energy during Propagation

Possible Direction	Up	Down	Left	Right	Random Number	Energy (J/mm)
Field (kV/mm)	4.87	13.4	0	12.1	0.54	325.61>62.56
Probability	0.14	0	0	0.86		
Prob_boundary	0.14	0.14	0.14	1		
Arc Direction	Right (No stop)					

The vertical electric field distribution from point A to B (Figure 36) is shown in Figure 37. The horizontal electric field distribution from point C to D (Figure 36) is shown in Figure 38.

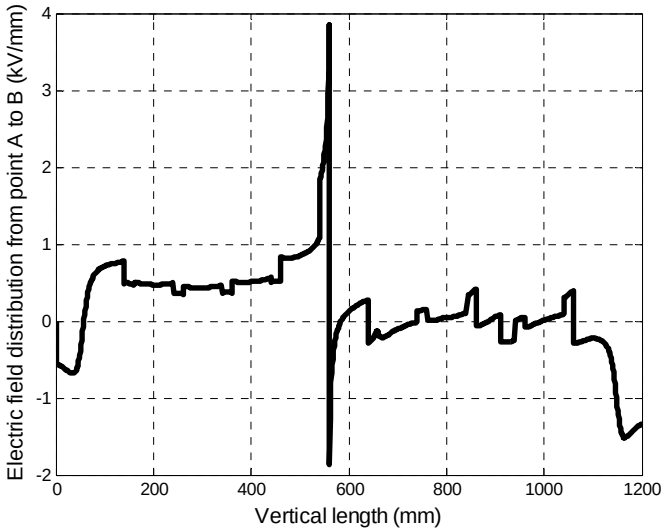

Figure 37. The Vertical Electric Field Distribution from Point A to B

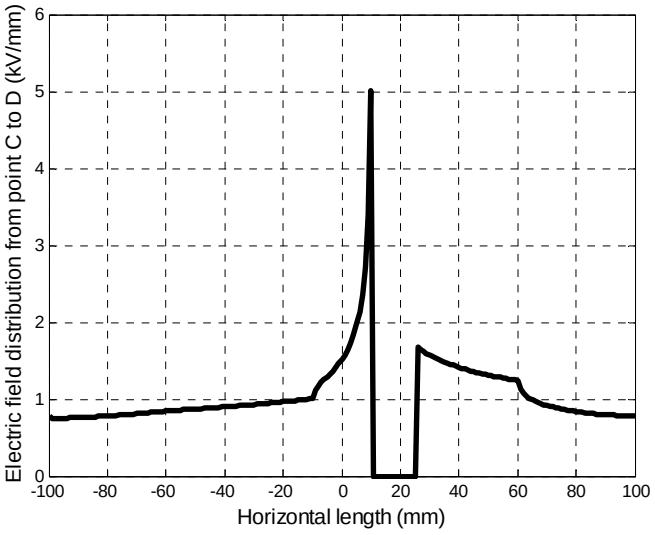

Figure 38. The Horizontal Electric Field Distribution from Point C to D

From Figures 37 and 38, it can be observed that maximum vertical and horizontal electric field is achieved at the leading end of the arc.

- Location 4: the arc reaches the location between shed 7 and 8.

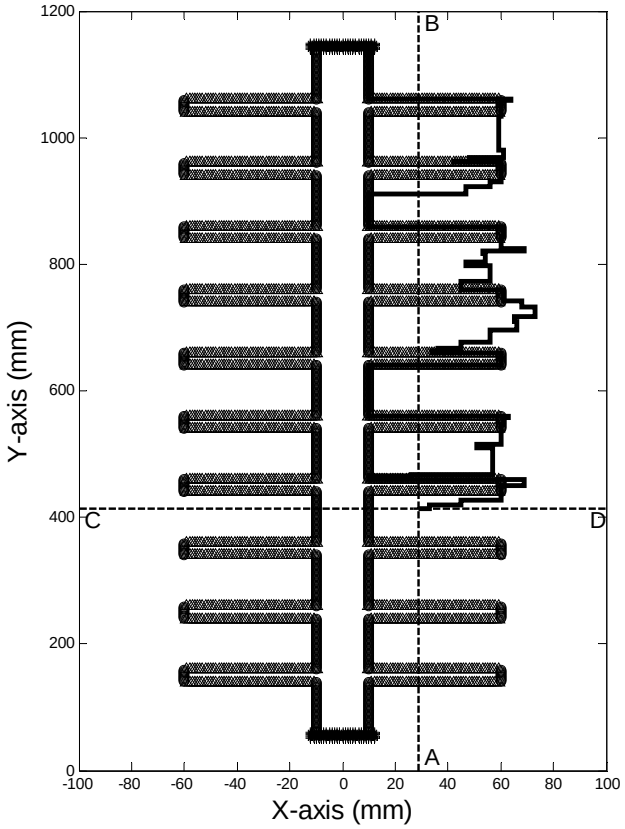

Figure 39 Arc Propagation Process of Location 4

Electric field to each direction and arc instant energy are shown in Table 7.

Table 7. Electric Field and Arc Instant Energy during Propagation

Possible Direction	Up	Down	Left	Right	Random Number	Energy (J/mm)
Field (kV/mm)	3.78	20.9	14.8	0	0.8	478.93>62.56
Probability	0.032	0.8	0.17	0		
Prob_boundary	0.032	0.83	1	1		
Arc Direction	Down (No stop)					

The vertical electric field distribution from point A to B (Figure 39) is shown in Figure 40. The horizontal electric field distribution from point C to D (Figure 39) is shown in Figure 41.

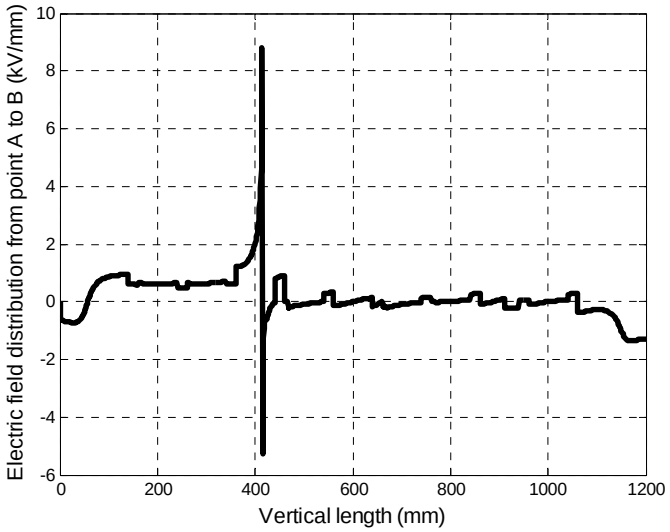

Figure 40. The Vertical Electric Field Distribution from Point A to B

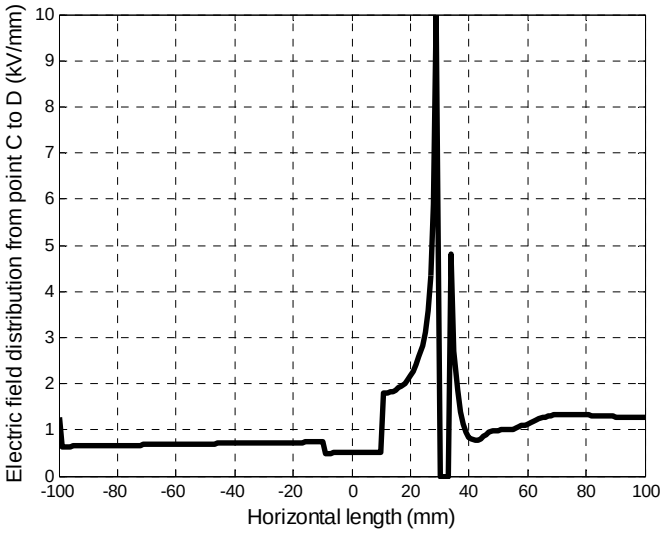

Figure 41. The Horizontal Electric Field Distribution from Point C to D

From Figures 40 and 41, it can be observed that maximum vertical and horizontal electric field is achieved at the leading end of the arc.

- Location 5: the arc reaches the location between shed 8 and 9.

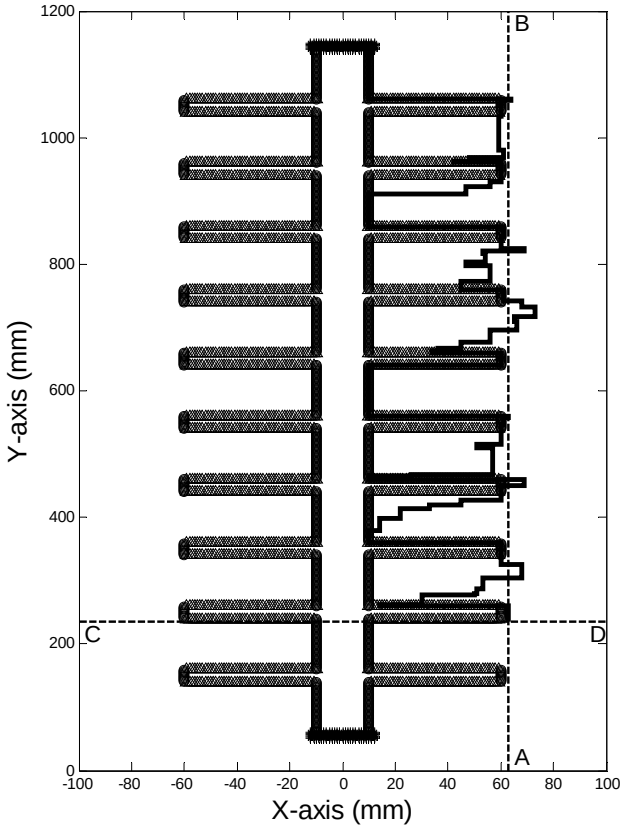

Figure 42. Arc Propagation Process of Location 5

Electric field to each direction and arc instant energy are shown in Table 8.

Table 8. Electric Field and Arc Instant Energy during Propagation

Possible Direction	Up	Down	Left	Right	Random Number	Energy (J/cm)
Field (kV/mm)	0	26.2	19.1	14.7	0.91	663.46>62.56
Probability	0	0.64	0	0.36		
Prob_boundary	0	0.64	0.64	1		
Arc Direction	Right (No stop)					

The vertical electric field distribution from point A to B (Figure 42) is shown in Figure 43. The horizontal electric field distribution from point C to D (Figure 42) is shown in Figure 44.

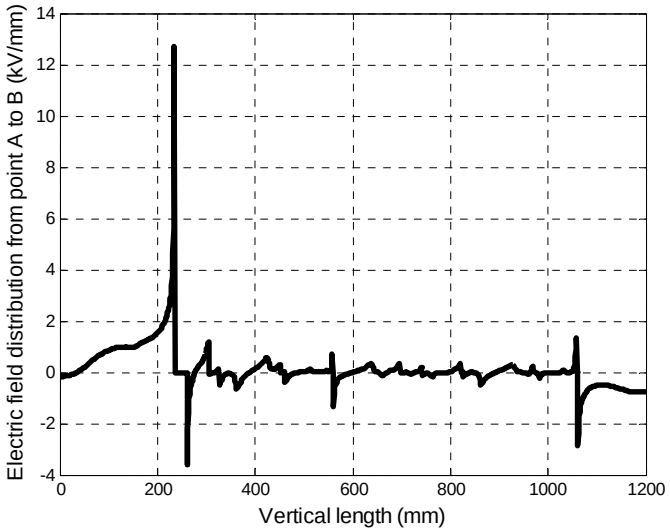

Figure 43 The Vertical Electric Field Distribution from Point A to B

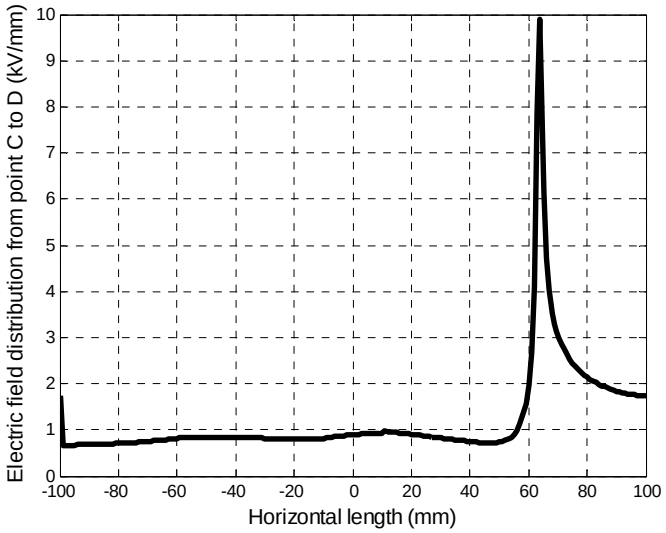

Figure 44 The Horizontal Electric Field Distribution from Point C to D

From Figures 41 and 42, it can be observed that maximum vertical and horizontal electric field is achieved at the leading end of the arc.

- Location 6: the arc reaches the location close to ground electrode.

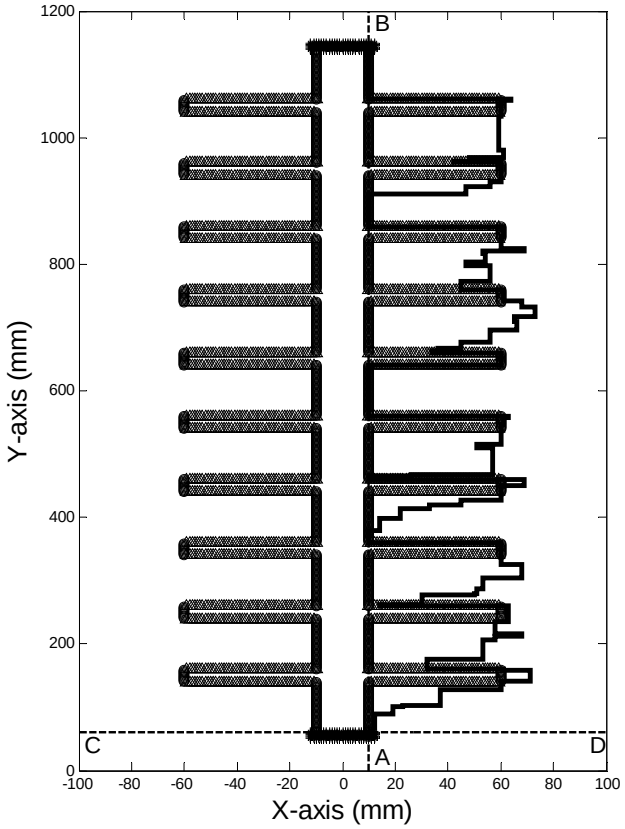

Figure 45 Arc Propagation Process of Location 6

The arc reaches the ground electrode and arc instant energy is still larger than air ionization energy. It is assumed that the arc has enough energy to complete the flashover.

The vertical electric field distribution from point A to B (Figure 45) is shown in Figure 46. The Horizontal electric field distribution from point C to D (Figure 45) is shown in Figure 47.

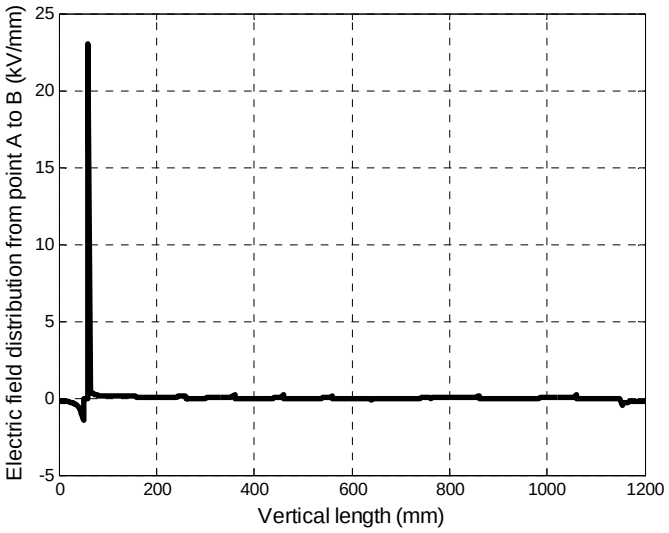

Figure 46 The Vertical Electric Field Distribution from Point A to B

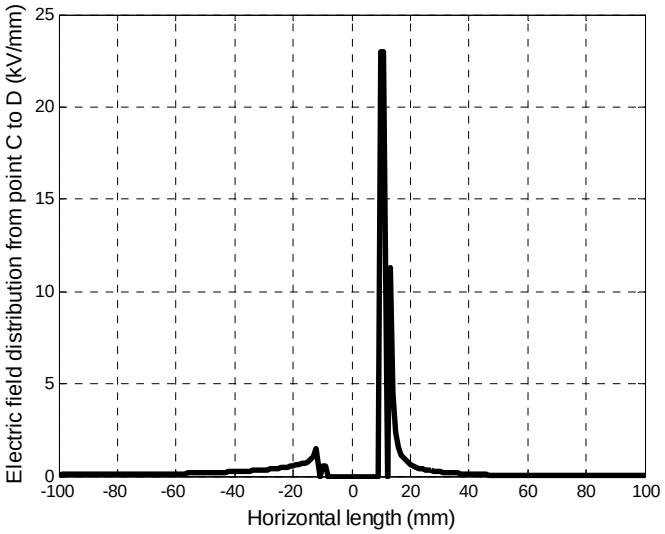

Figure 47 The Horizontal Electric Field Distribution from Point C to D

From six locations during arc propagation, it can be concluded that the electric field increases as the arc grows close to the ground electrode. This is caused by the reduction of insulator leakage distance during arc propagation process.

4.3 Simulation Results under Different Conditions

- Case 1: supply voltage is 70 kV and ESDD value is 0.02 mg/cm^2.

The arc propagation process is repeated for 110 times in Figure 48 and the number of flashover and arc jumping between sheds is recorded to calculate the probability.

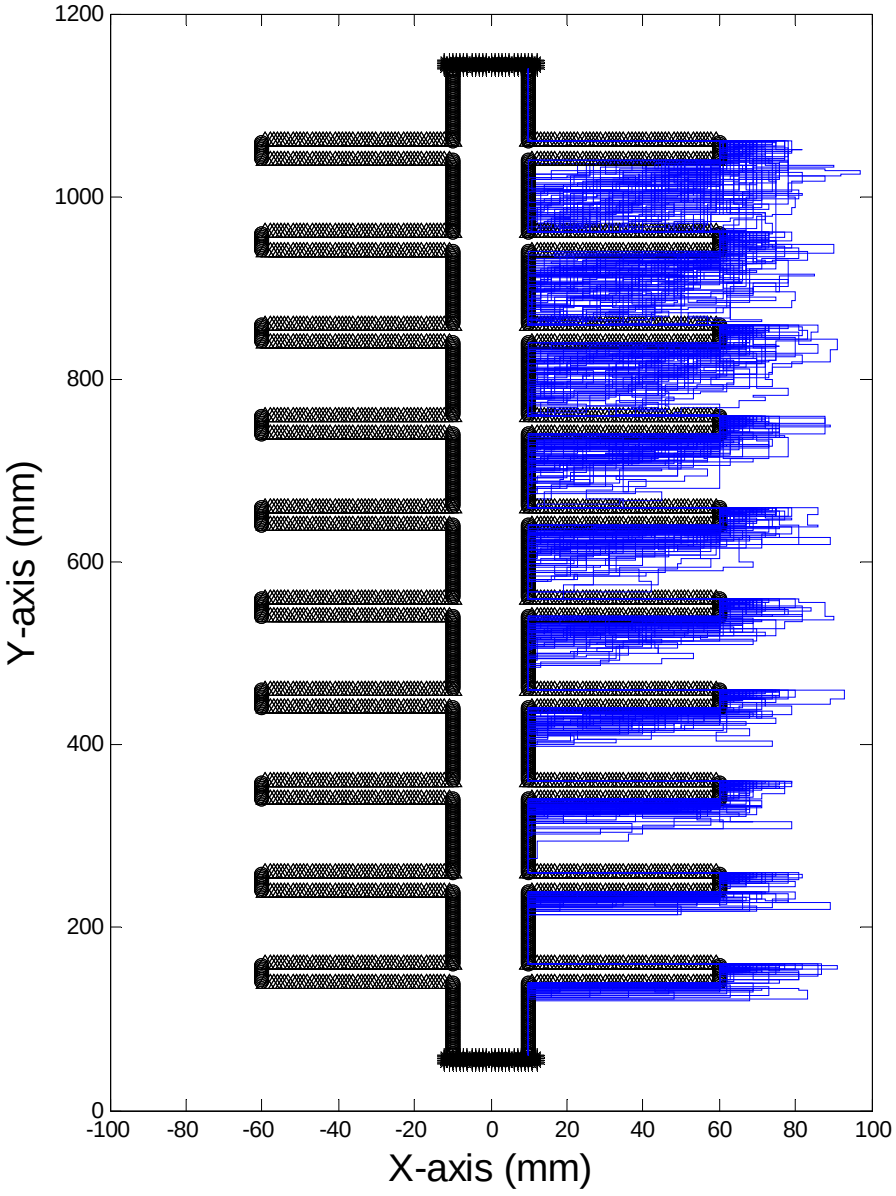

Figure 48 The 110 Times Arc Propagation Processes under Case 1 Condition

The flashover probability is 4%. The probability of arc jumping between sheds is shown in Table 9.

Table 9. The Arc Jumping between Sheds Probability at Different Locations

Sheds Number	1	2	3	4	5	6	7	8	9	10
Arc Jump Probability (%)	45	17	6	4	2	0	0	0	0	0

The histogram of arc jumping sheds probability is shown in Figure 49.

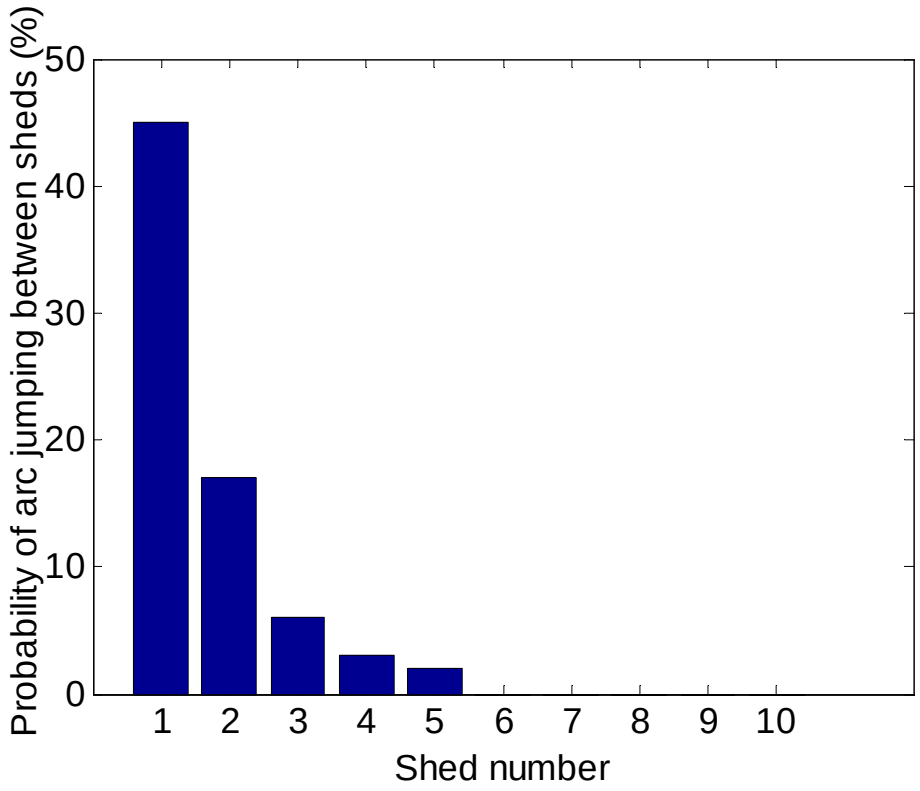

Figure 49 The Arc Jumping between Sheds Probability at Different Locations

The probability mean of arc jumping between ten sheds is calculated as,

$$Mean_{Jump} = \frac{\sum Arc\ Jump\ Probability}{Number\ of\ Sheds} = \frac{0+0+0+0+0+2+4+6+17+45}{10} = 7.3\% \quad (54)$$

The probability standard deviation of arc jumping between ten sheds is calculated as,

$$Std_{Jump} = \sqrt{\frac{\sum (Arc\ Jump\ Probability - Mean_{Jump})^2}{Number\ of\ Sheds}} = 14.26\% \quad (55)$$

- Case 2: supply voltage is 70 kV and ESDD value is 0.5 mg/cm^2.

The arc propagation process is repeated for 110 times in Figure 50 and the number of flashover and arc jumping between sheds is recorded to calculate the probability.

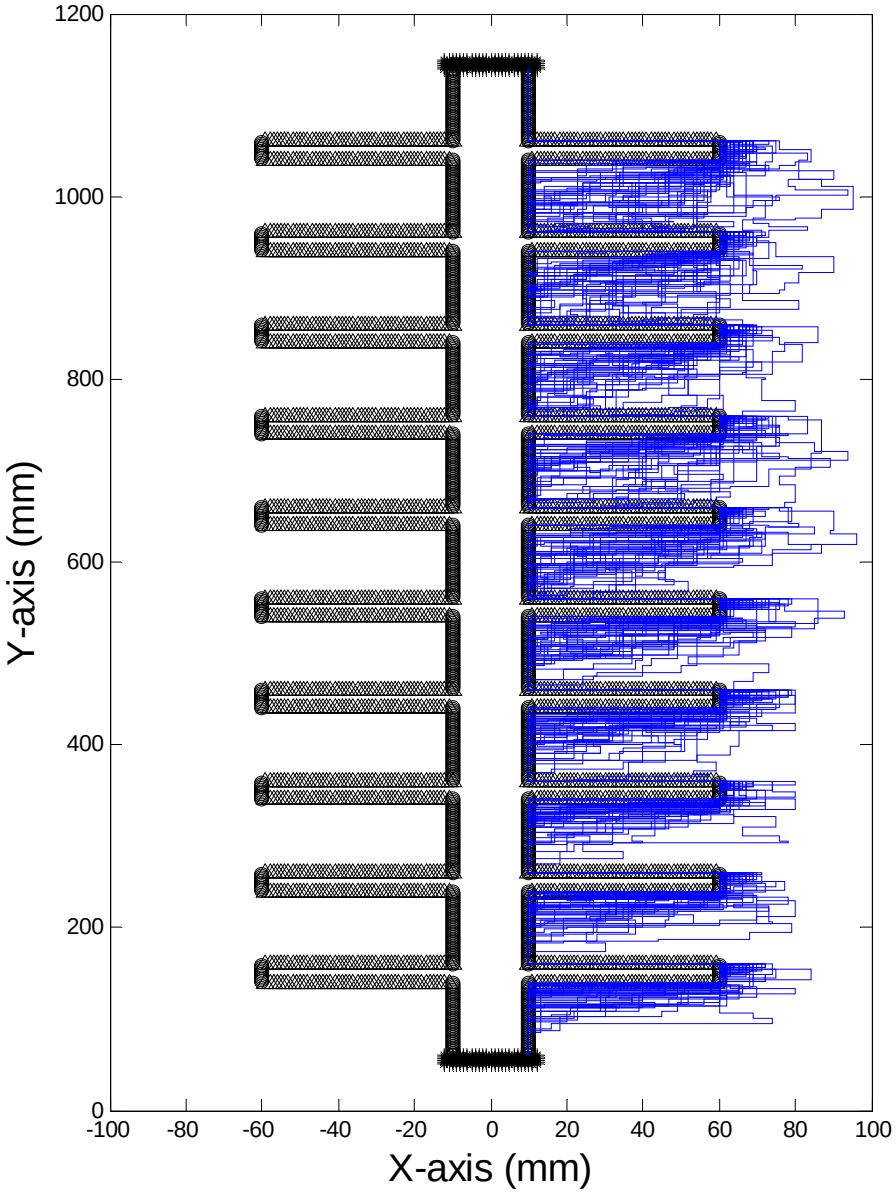

Figure 50 The 110 Times Arc Propagation Processes under Case 2 Condition

The flashover probability is 13%. The probability of arc jumping between sheds is

shown in Table 10.

Table 10. The Arc Jumping between Sheds Probability at Different Locations

Sheds Number	1	2	3	4	5	6	7	8	9	10
Arc Jump Probability (%)	17	13	12	10	4	7	4	3	8	8

The histogram of arc jumping sheds probability is shown in Figure 51.

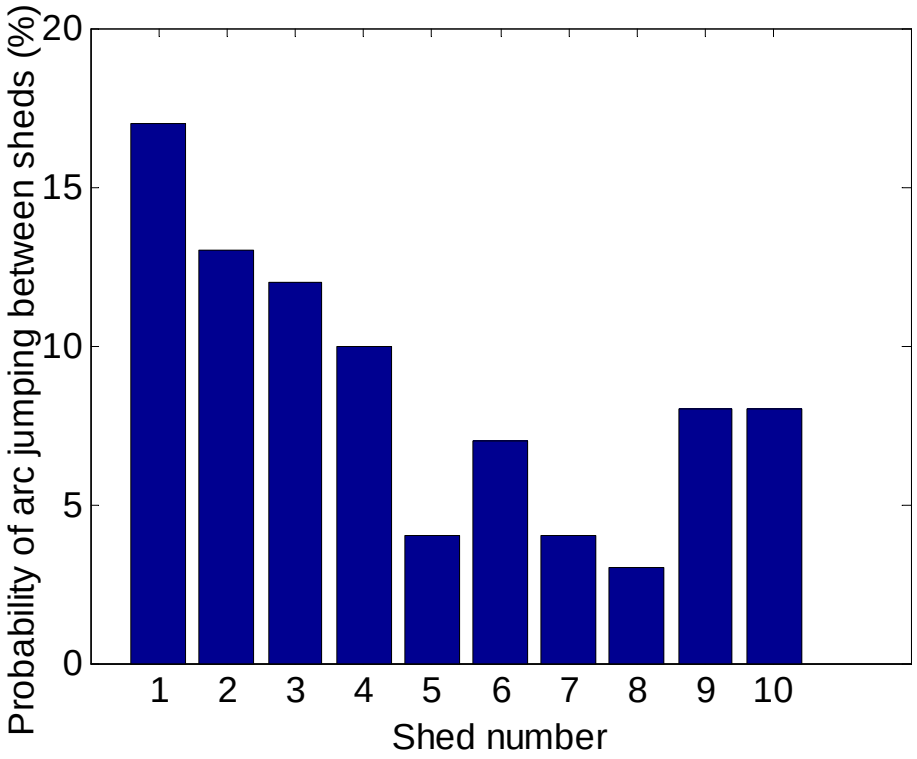

Figure 51 The Arc Jumping between Sheds Probability at Different Locations

The probability mean of arc jumping between ten sheds is calculated as,

$$Mean_{Jump} = \frac{\sum Arc\ Jump\ Probability}{Number\ of\ Sheds} = \frac{8+8+3+4+7+4+10+12+13+17}{10} = 8.6\% \quad (59)$$

The probability standard deviation of arc jumping between ten sheds is calculated as,

$$Std_{Jump} = \sqrt{\frac{\sum (Arc\ Jump\ Probability - Mean_{Jump})^2}{Number\ of\ Sheds}} = 4.47\% \quad (60)$$

- Case 3: supply voltage is 138 kV and ESDD value is 0.02 mg/cm^2.

The arc propagation process is repeated for 110 times in Figure 52 and the number of flashover and arc jumping between sheds is recorded to calculate the probability.

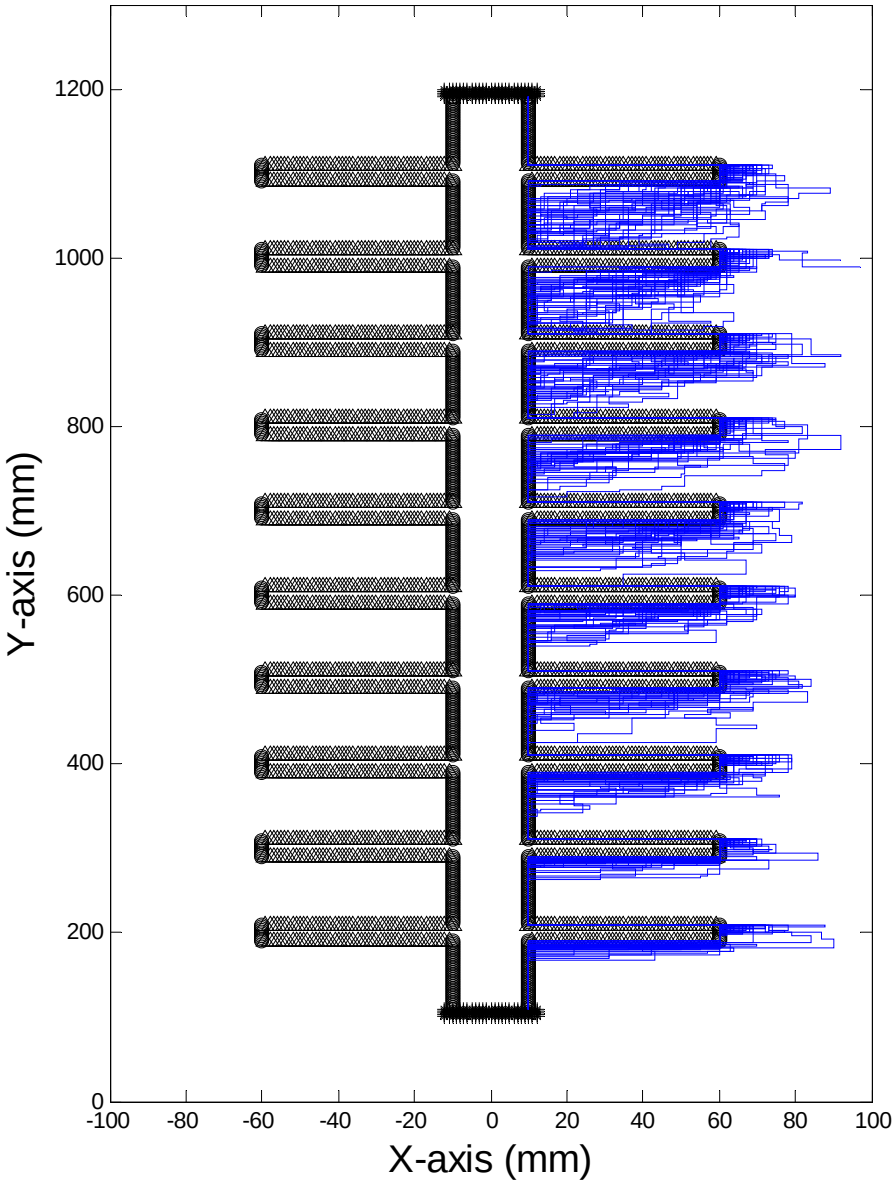

Figure 52 The 110 Times Arc Propagation Processes under Case 3 Condition

The flashover probability is 32%. The probability of arc jumping between sheds is

shown in Table 11.

Table 11. The Arc Jumping between Sheds Probability at Different Locations

Sheds Number	1	2	3	4	5	6	7	8	9	10
Arc Jump Probability (%)	63	21	14	10	3	12	10	7	0	0

The histogram of arc jumping sheds probability is shown in Figure 53.

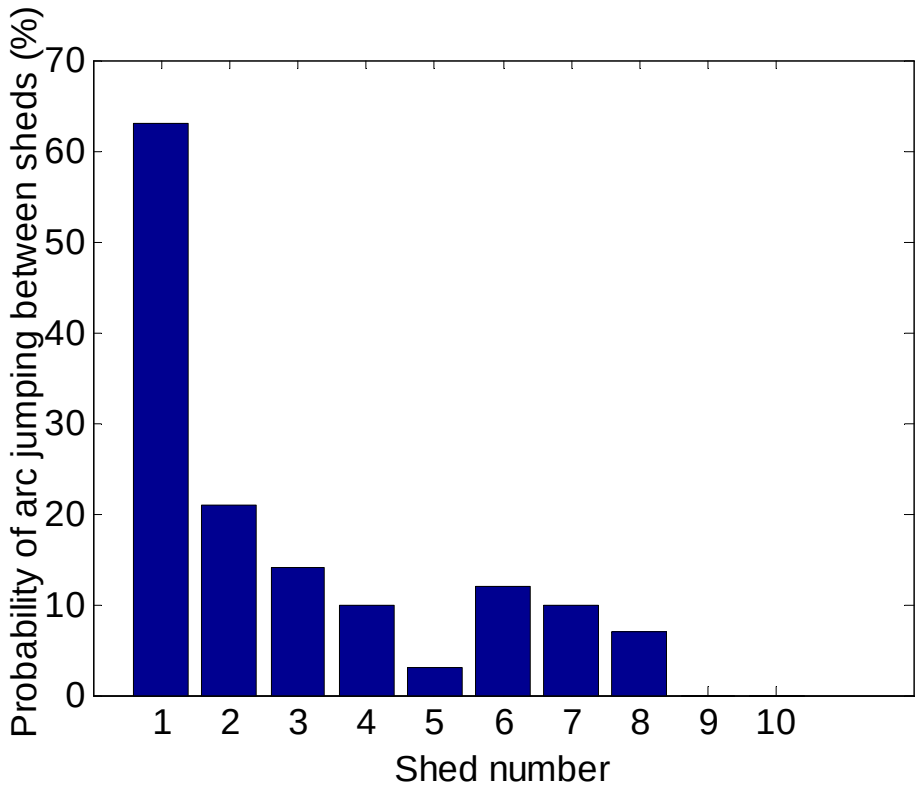

Figure 53. The Arc Jumping between Sheds Probability at Different Locations

The probability mean of arc jumping between ten sheds is calculated as,

$$Mean_{Jump} = \frac{\sum Arc\ Jump\ Probability}{Number\ of\ Sheds} = \frac{0+0+7+10+12+3+10+14+21+63}{10} = 13\% \quad (61)$$

The probability standard deviation of arc jumping between ten sheds is calculated as,

$$Std_{Jump} = \sqrt{\frac{\sum (Arc\ Jump\ Probability - Mean_{Jump})^2}{Number\ of\ Sheds}} = 18.4\% \quad (62)$$

- Case 4: supply voltage is 138 kV and ESDD value is 0.5 mg/cm^2.

The arc propagation process is repeated for 100 times in Figure 54 and the number of flashover and arc jumping between sheds is recorded to calculate the probability.

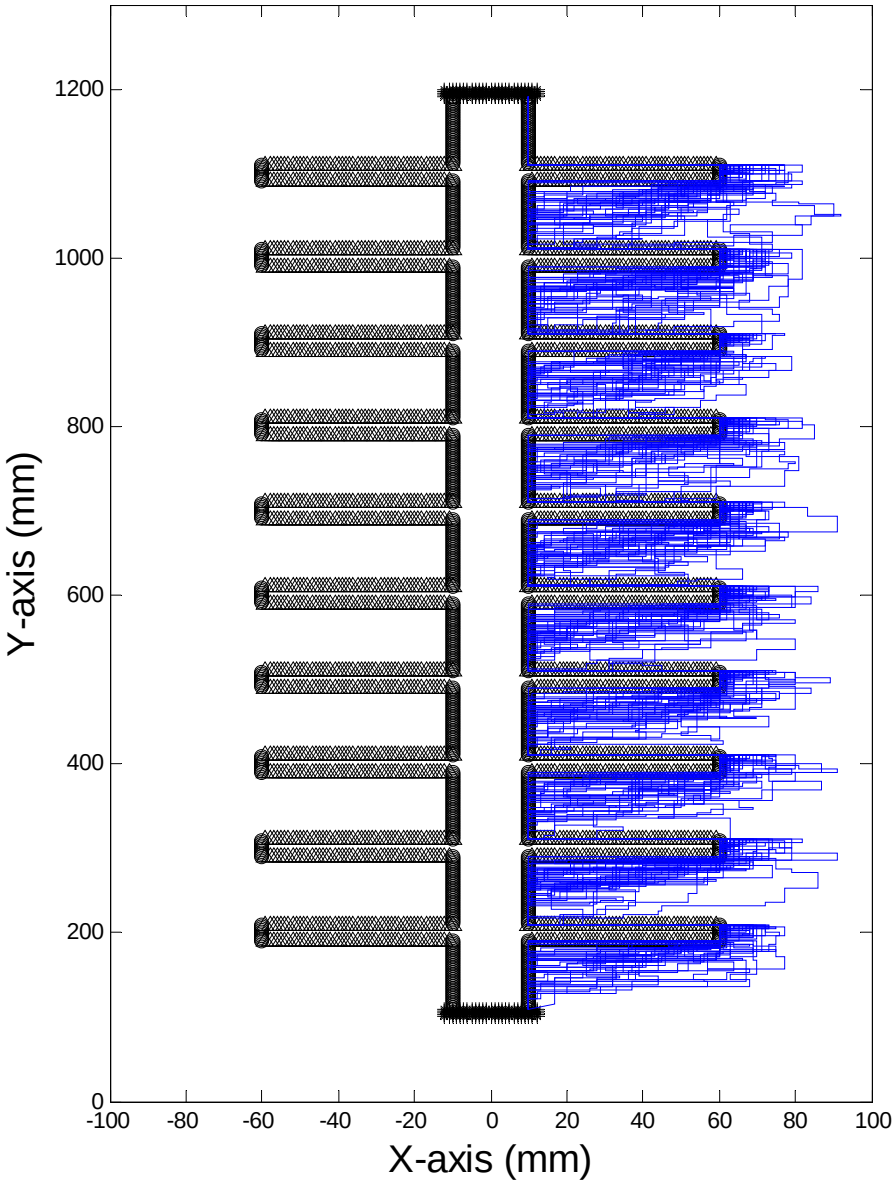

Figure 54. The 110 Times Arc Propagation Processes under Case 4 Condition

The flashover probability is 45%. The probability of arc jumping between sheds is

shown in Table 12.

Table 12. The Arc Jumping between Sheds Probability at Different Locations

Sheds Number	1	2	3	4	5	6	7	8	9	10
Arc Jump Probability (%)	28	22	15	13	10	12	11	12	15	17

The histogram of arc jumping sheds probability is shown in Figure 55.

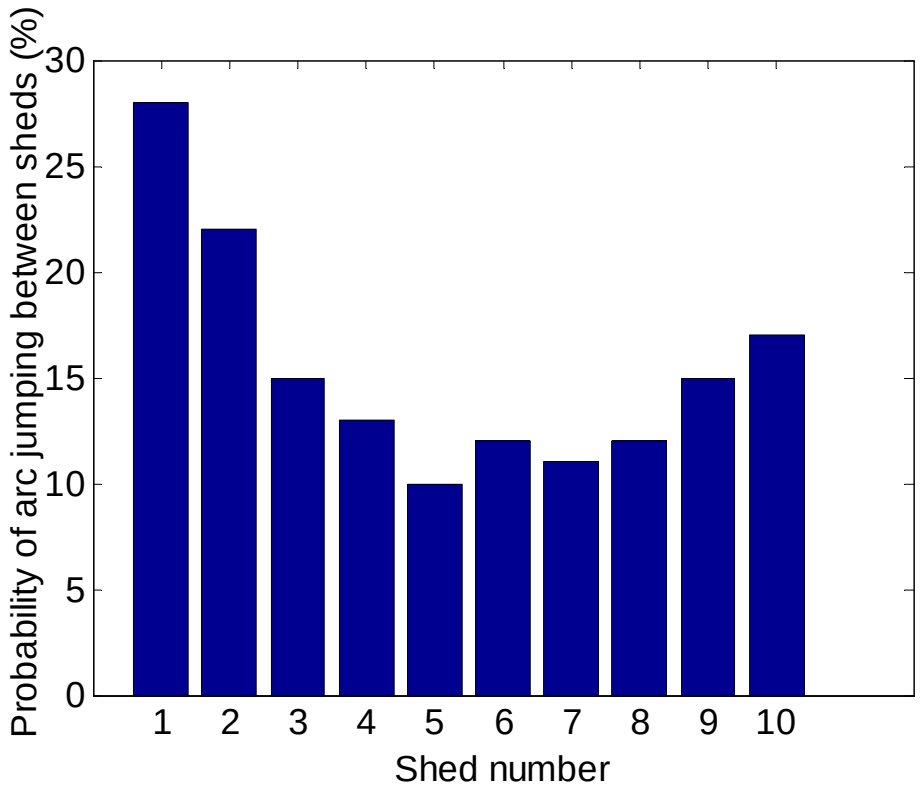

Figure 55. The Arc Jumping between Sheds Probability at Different Locations

The probability mean of arc jumping between ten sheds is calculated as,

$$Mean_{Jump} = \frac{\sum Arc\ Jump\ Probability}{Number\ of\ Sheds} = \frac{17+15+12+11+12+10+13+15+22+28}{10} = 15.5\% \tag{63}$$

The probability standard deviation of arc jumping between ten sheds is calculated as,

$$Std_{Jump} = \sqrt{\frac{\sum (Arc\ Jump\ Probability - Mean_{Mean})^2}{Number\ of\ Sheds}} = 5.6\% \tag{64}$$

4.4 Regression Model of Simulation Results

4.4.1 Flashover Probability Regression Model

The flashover probability under different supply voltage and surface contamination levels is shown in Table 13.

Table 13. Flashover Probability under Four Different Conditions

Flashover Probability (%)	Supply Voltage (kV)	ESDD (mg/cm^2)
4	70	0.02
13	70	0.5
32	138	0.02
45	138	0.5

Since this model involves two factors: supply voltage and ESDD value, 2^2 factorial design is used to evaluate the effects of these factors to the flashover probability. By a factorial design, all possible combinations of the levels of the factors are investigated in each complete trial or replication of the experiment.

Assume that V is the factor of voltage and E is the factor of ESDD value. The magnitude of factors is normalized to [-1, 1].

The treatment combinations of this stochastic process are shown in Table 14.

Table 14. The Treatment Combinations of the Stochastic Process

Factor V	Factor E	Treatment Combination	Flashover Probability
-	-	V low, E low	4
-	+	V low, E high	13
+	-	V high, E low	32
+	+	V high, E high	45

The main effect of factor V:

$$V = \frac{45+32}{2} - \frac{4+13}{2} = 30 \tag{65}$$

The main effect of factor E:

$$E = \frac{45+13}{2} - \frac{32+4}{2} = 11 \tag{66}$$

The interaction effect of factor VE:

$$VE = \frac{45+4}{2} - \frac{32+13}{2} = 2 \tag{67}$$

The regression model is,

$$\hat{y} = 23.5 + \frac{V}{2}x_1 + \frac{E}{2}x_2 + \frac{VE}{2}x_1x_2 = 23.5 + 15x_1 + 5.5x_2 + x_1x_2 \tag{68}$$

Where x_1 is a variable that represents factor V and x_2 is a variable that represents factor E. It is concluded that both supply voltage and ESDD value have significant effects on the flashover probability.

4.4.2 Probability Mean of Arc Jumping Regression Model

The probability mean of arc jumping between sheds under different supply voltages and surface contamination levels is shown in Table 15.

Table 15. Arc Jump Sheds Probability under Four Different Conditions

Probability mean of Arc Jumping (%)	Supply Voltage (kV)	ESDD (mg/cm^2)
7.3	70	0.02
8.6	70	0.5
13	138	0.02
15.5	138	0.5

Similarly, this model involves two factors: supply voltage and ESDD value. Therefore, 2^2 factorial design is used to evaluate the effects of these factors to the arc jumping probability.

Assume that V is the factor of voltage and E is the factor of ESDD. The magnitude of factors is normalized to [-1, 1].

The treatment combinations of this stochastic process are shown in Table 16.

Table 16. The Treatment Combinations of the Stochastic Process

Factor V	Factor E	Treatment Combination	Arc Jumping Probability
-	-	V low, E low	7.3
-	+	V low, E high	8.6
+	-	V high, E low	13
+	+	V high, E high	15.5

The main effect of factor V:

$$V = \frac{13+15.5}{2} - \frac{7.3+8.6}{2} = 6.3 \tag{69}$$

The main effect of factor E:

$$E = \frac{8.6+15.5}{2} - \frac{13+7.3}{2} = 1.9 \tag{70}$$

The interaction effect of factor VE:

$$VE = \frac{7.3+15.5}{2} - \frac{8.6+13}{2} = 0.6 \tag{71}$$

The regression model is,

$$\hat{y} = 11.1 + \frac{V}{2}x_1 + \frac{E}{2}x_2 + \frac{VE}{2}x_1x_2 = 11.1 + 3.15x_1 + 0.95x_2 + 0.3x_1x_2 \tag{72}$$

Where x_1 is a variable that represents factor V and x_2 is a variable that represents factor E. It is concluded that only supply voltage has significant positive effect on probability mean of arc jumping between sheds when the pollution layer on the insulator surface is uniform.

4.4.3 Probability Standard Deviation of Arc Jumping Regression Model

The probability standard deviation of arc jumping between sheds under different supply voltages and surface contamination levels is shown in Table 17.

Table 17. Arc Jump Sheds Probability under Four Different Conditions

Probability standard deviation of Arc Jumping (%)	Supply Voltage (kV)	ESDD (mg/cm^2)
14.26	70	0.02
4.47	70	0.5
18.4	138	0.02
5.6	138	0.5

Similarly, this model involves two factors: supply voltage and ESDD value. Therefore, 2^2 factorial design is used to evaluate the effects of these factors to the arc jumping probability. Assume that V is the factor of voltage and E is the factor of ESDD. The magnitude of factors is normalized to [-1, 1].

The treatment combinations of this stochastic process are shown in Table 18.

Table 18. The Treatment Combinations of the Stochastic Process

Factor V	Factor E	Treatment Combination	Arc Jumping Probability
-	-	V low, E low	14.26
-	+	V low, E high	4.47
+	-	V high, E low	18.4
+	+	V high, E high	5.6

The main effect of factor V:

$$V = \frac{18.4 + 5.6}{2} - \frac{14.26 + 4.47}{2} = 2.63 \tag{73}$$

The main effect of factor E:

$$E = \frac{14.26 + 18.4}{2} - \frac{4.47 + 5.6}{2} = 11.3 \tag{74}$$

The interaction effect of factor VE:

$$VE = \frac{18.4 + 4.47}{2} - \frac{14.26 + 5.6}{2} = 1.505 \tag{75}$$

The regression model is,

$$\hat{y} = 10.68 + \frac{V}{2}x_1 + \frac{E}{2}x_2 + \frac{VE}{2}x_1x_2 = 10.68 + 1.32x_1 + 5.65x_2 + 1.505x_1x_2 \tag{76}$$

Where x_1 is a variable that represents factor V and x_2 is a variable that represents factor E. It is concluded that only ESDD has negative effect on probability standard deviation of arc jumping between sheds when the pollution layer on the insulator surface is uniform.

4.5 Flashover Voltage in terms of Different Contamination Levels

For the insulator model in Figure 12, 138 kV is set to HV electrode. The flashover probability as a function of ESDD values is shown in Figure 56.

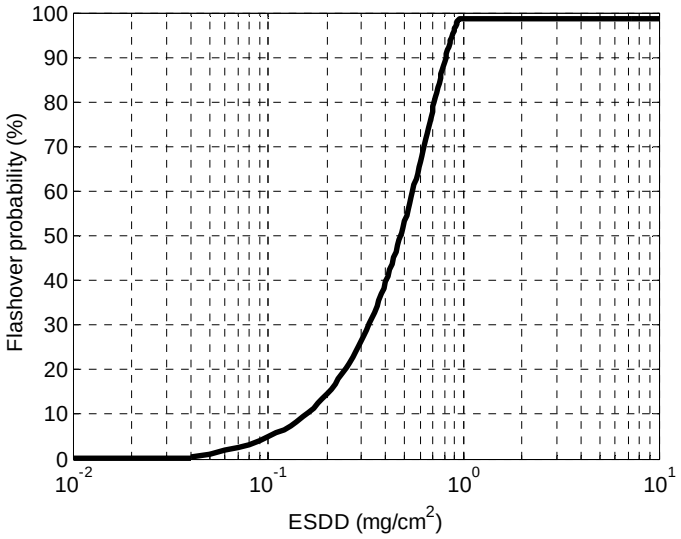

Figure 56. Flashover Probability as a Function of ESDD Values

Since 50% flashover voltage is an important parameter in insulator testing and widely measured in the experiments according to IEEE Standard 4-2013 [31], the new statistical method calculates the 50% flashover voltage as a function of ESDD by considering the stochastic phenomena of arc jumping. The results are compared with deterministic method in Figure 9. It is indicated that the 50% flashover voltage of statistical model is lower than that of deterministic model when the pollution severity on the insulator surface remains the same. The experimental results are also shown in Figure 57 [27]. The 50% flashover voltage results of statistical method are close to the voltage results from experiments. The deviation of the results from experimental values is larger for the deterministic model when compared to the present results for

ESDD values below 0.05 mg/cm^2, which is representative of most locations.

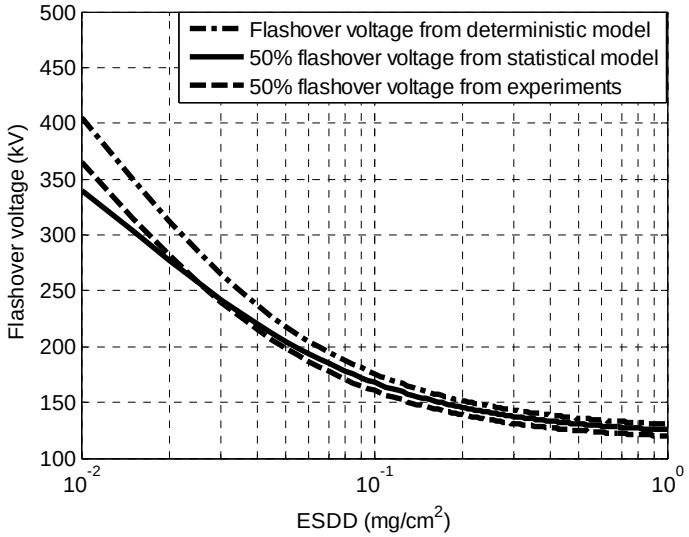

Figure 57. Comparison of Flashover Deterministic and Statistical Models

5 INSULATOR FLASHOVER PERFORMANCE WITH WATER PARTICLES IN THE AIR

When insulator is exposed in the rain or mist condition, the electric field around the insulator is distorted by the water particles in the air. Since the direction of arc propagation track is also driven by the electric field, new model is simulated to evaluate the effects of water particles on the probability of flashover and arc jumping between sheds. 138 kV insulator is modeled in this chapter (Figure 58).

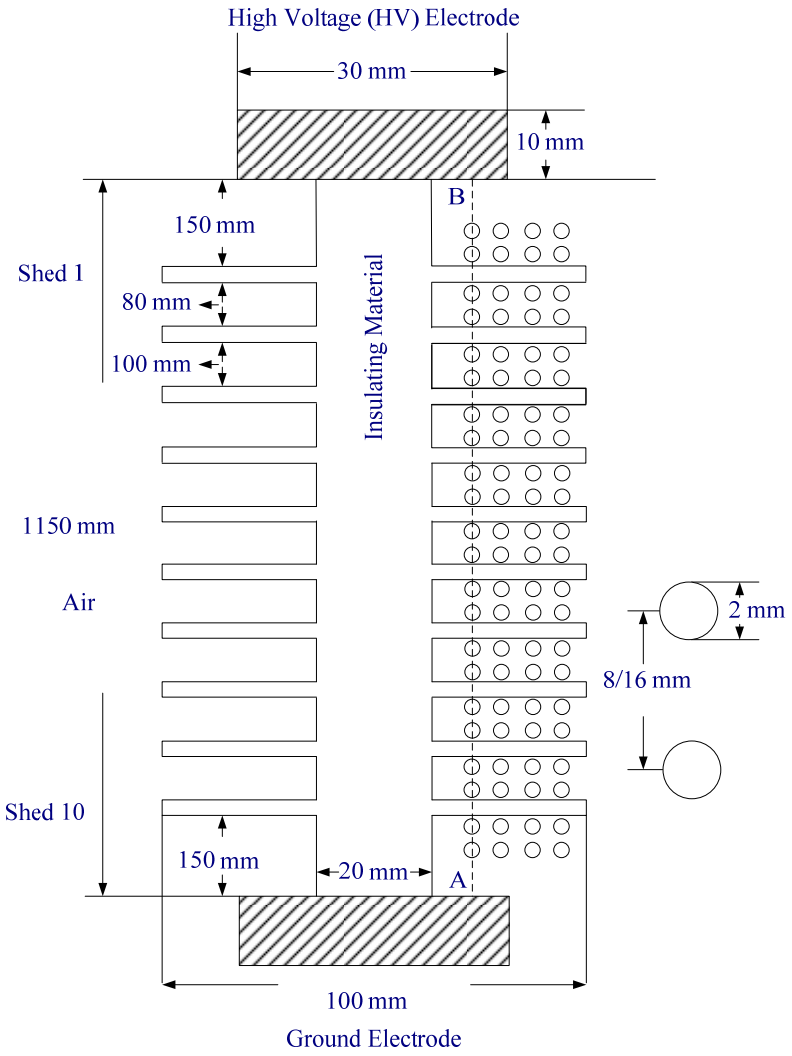

Figure 58. 138 kV Insulator with Water Particles between Sheds

Different density of water particle distribution and ESDD values are analyzed in following four cases (Table 19). Water droplets with different density distributions are shown in Figure 59 (a) and (b).

Table 19 Four Different Simulation Cases

Case Number	Number of Water particles (/cm^2)	ESDD (mg/cm^2)
1	4	0.5
2	4	0.02
3	1	0.5
4	1	0.02

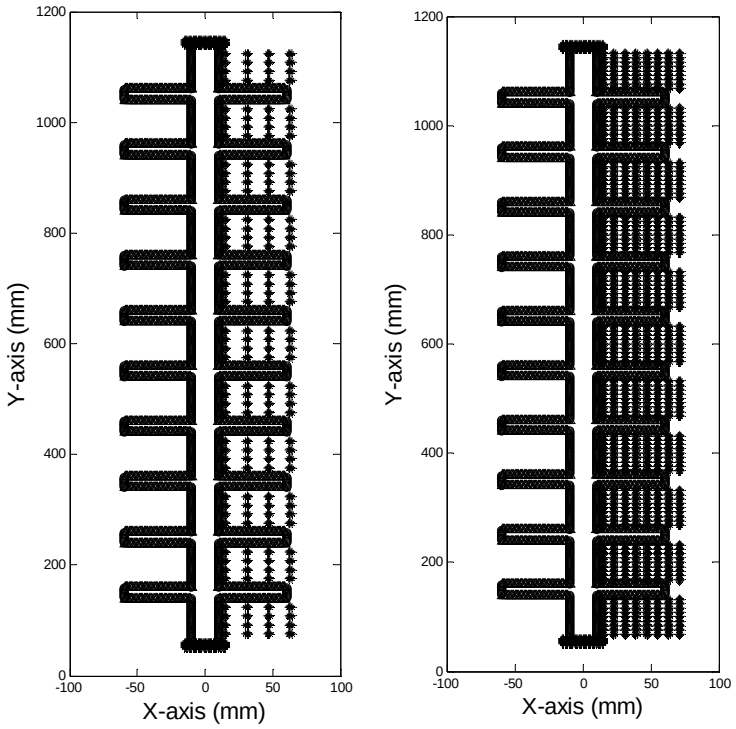

(a) (b)

Figure 59. Sparse and Dense Particles Distributions

5.1 Insulator Model with High ESDD and Dense Particle Distribution

The insulator model with high ESDD value and dense water particle distribution is shown in this section. The electric field distribution from point A to point B (Figure 58) is shown in Figure 60 to observe the effects of water particles on electric field in the air. Meanwhile, electric field distribution along the leakage distance is also shown in Figure 61.

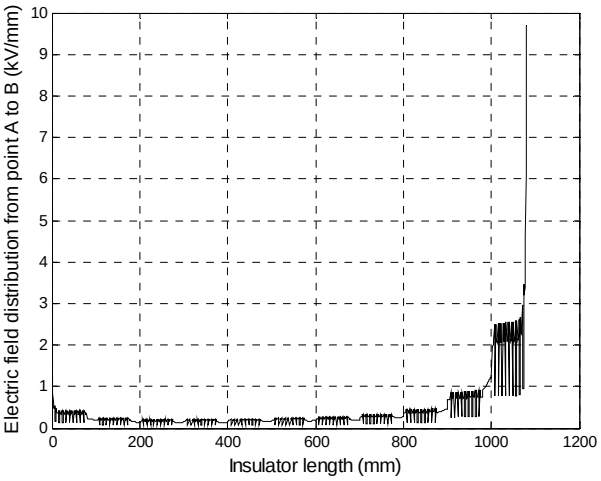

Figure 60. Electric Field Distribution from Point A to B

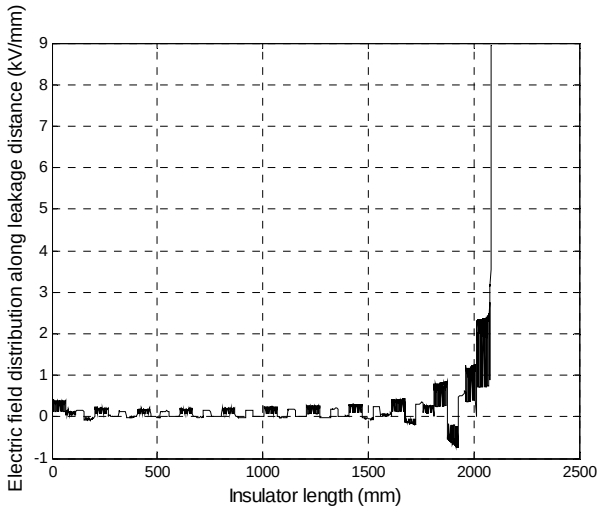

Figure 61. Electric Field Distribution along the Insulator Leakage Distance

The arc propagation process is repeated for 110 times in Figure 62.

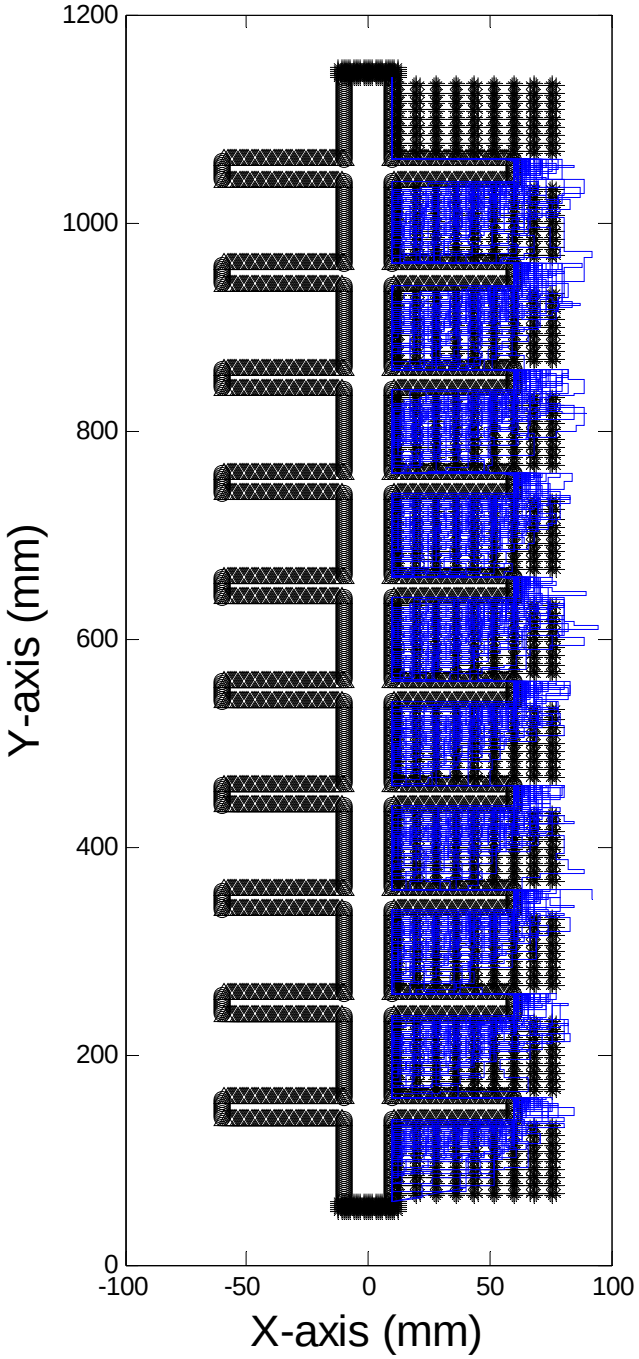

Figure 62. The 110 Times Arc Propagation Processes in Case 1

5.2 Insulator Model with High ESDD and Sparse Particle Distribution

The insulator model with high ESDD value and sparse water particle distribution is shown in this section. The electric field distribution from point A to point B (Figure 58) is shown in Figure 63 to observe the effects of water particles on electric field in the air. Meanwhile, electric field distribution along the leakage distance is also shown in Figure 64.

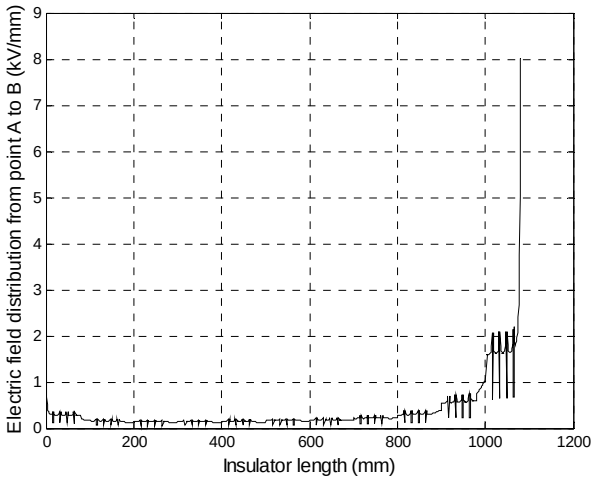

Figure 63 Electric Field Distribution from Point A to B

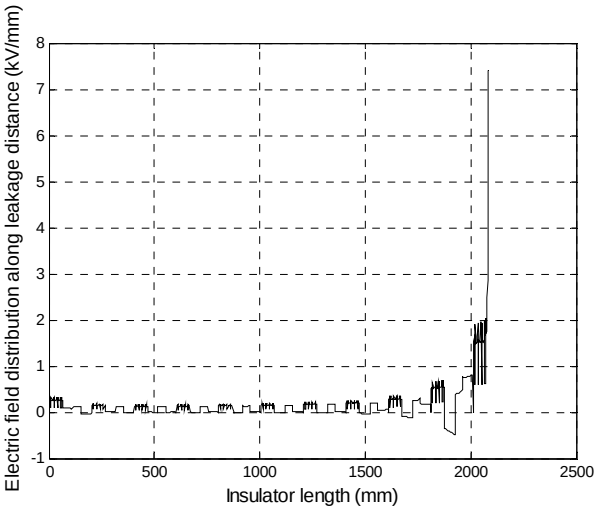

Figure 64 Electric Field Distribution along the Insulator Leakage Distance

The arc propagation process is repeated for 110 times in Figure 65.

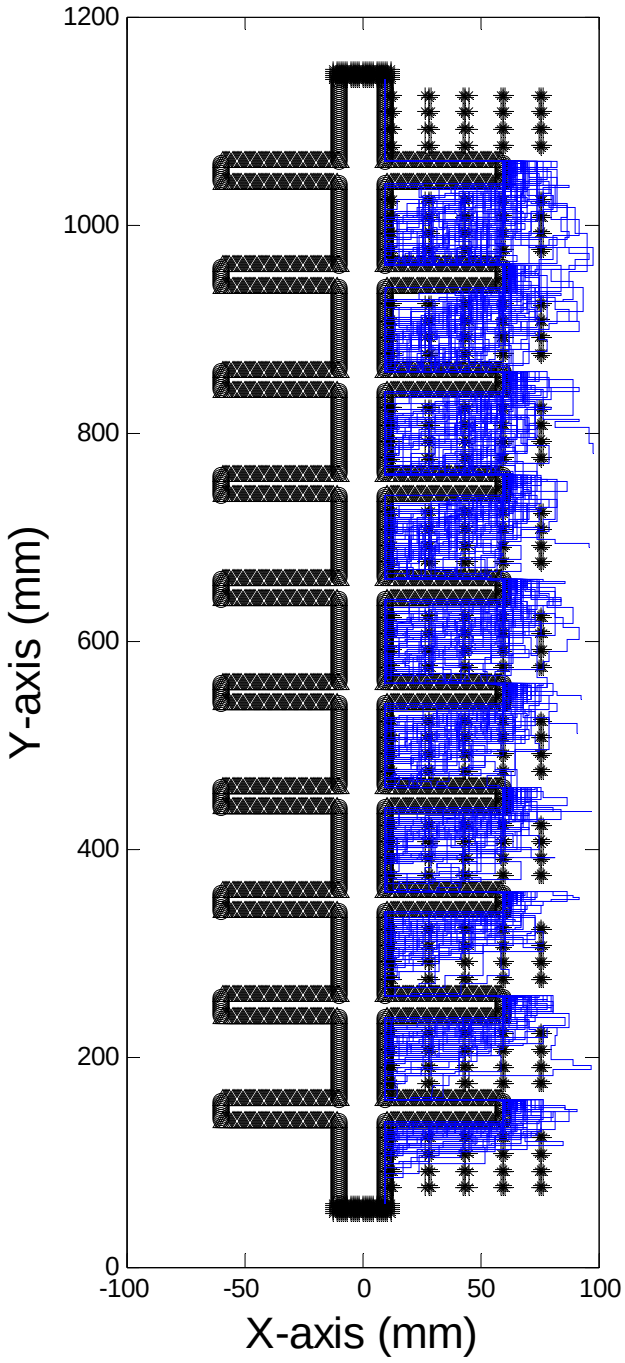

Figure 65. The 110 Times Arc Propagation Processes in Case 2

5.3 Insulator Model with Low ESDD and Dense Particle Distribution

The insulator model with low ESDD value and dense water particle distribution is shown in this section. The electric field distribution from point A to point B (Figure 58) is shown in Figure 66 to observe the effects of water particles on electric field in the air. Meanwhile, electric field distribution along the leakage distance is also shown in Figure 67.

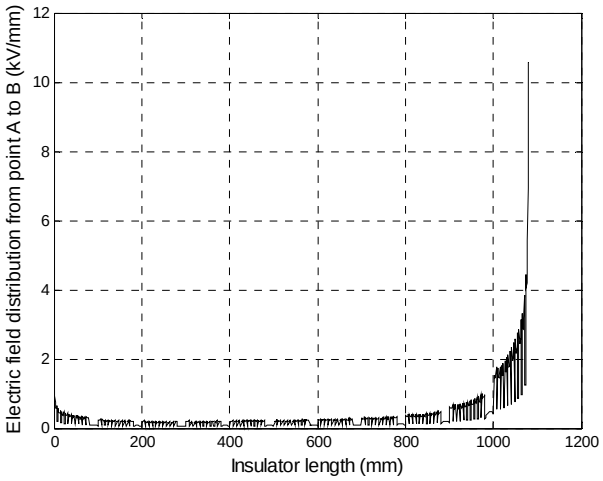

Figure 66 Electric Field Distribution from Point A to B

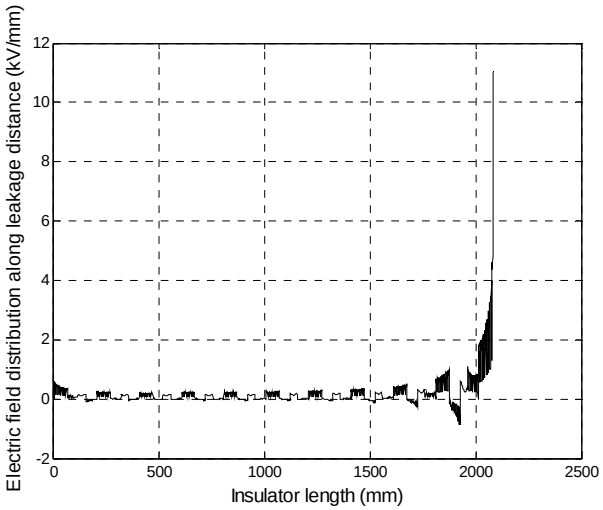

Figure 67. Electric Field Distribution along the Insulator Leakage Distance

The arc propagation process is repeated for 110 times in Figure 68.

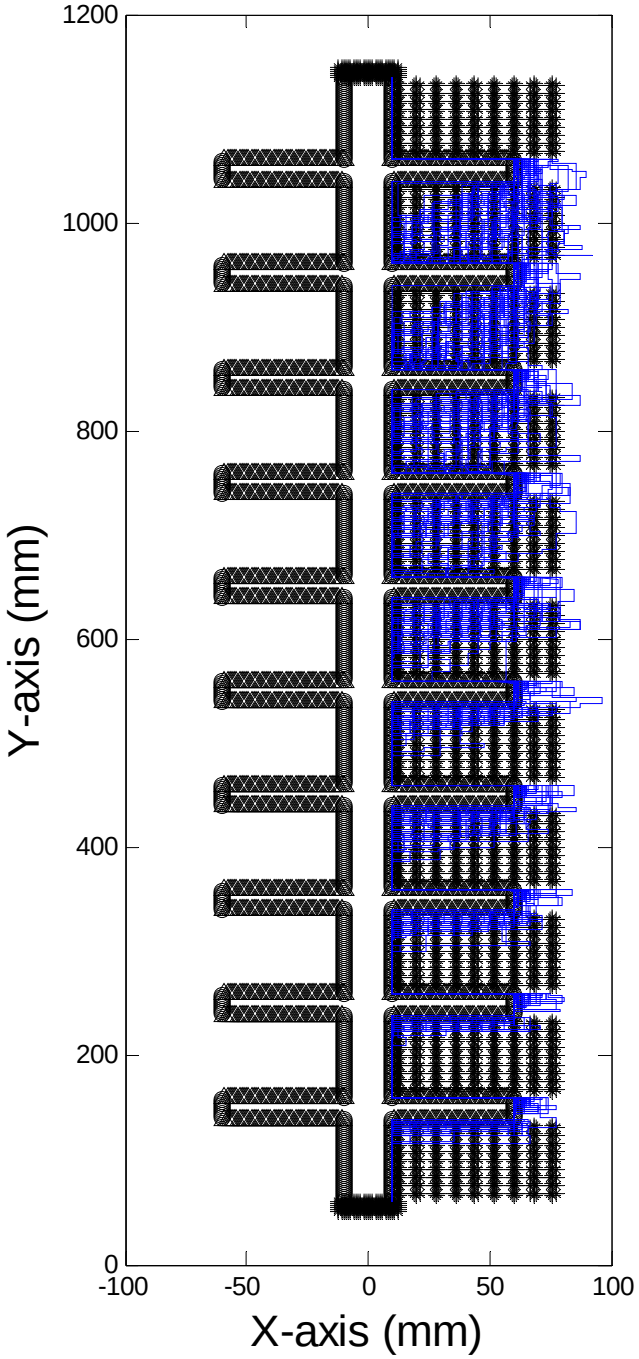

Figure 68. The 110 Times Arc Propagation Processes in Case 3

5.4 Insulator Model with Low ESDD and Sparse Particle Distribution

The insulator model with low ESDD value and sparse water particle distribution is shown in this section. The electric field distribution from point A to point B (Figure 58) is shown in Figure 69 to observe the effects of water particles on electric field in the air. Meanwhile, electric field distribution along the leakage distance is also shown in Figure 70.

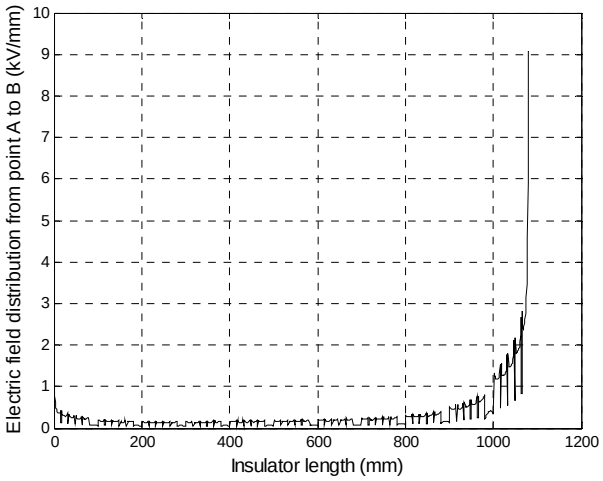

Figure 69. Electric Field Distribution from Point A to B

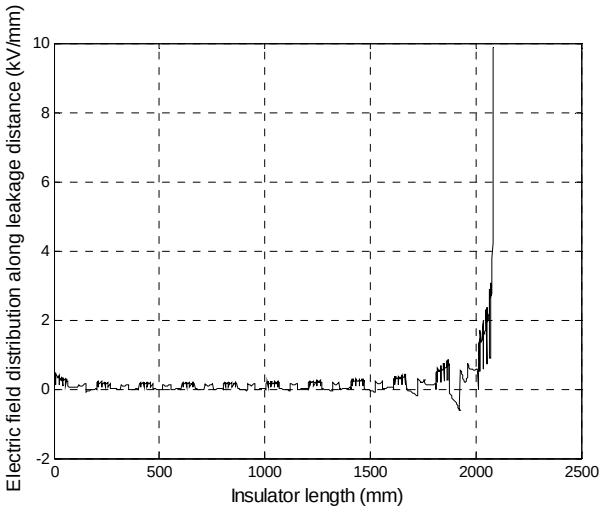

Figure 70. Electric Field Distribution along the Insulator Leakage Distance

The arc propagation process is repeated for 110 times in Figure 71.

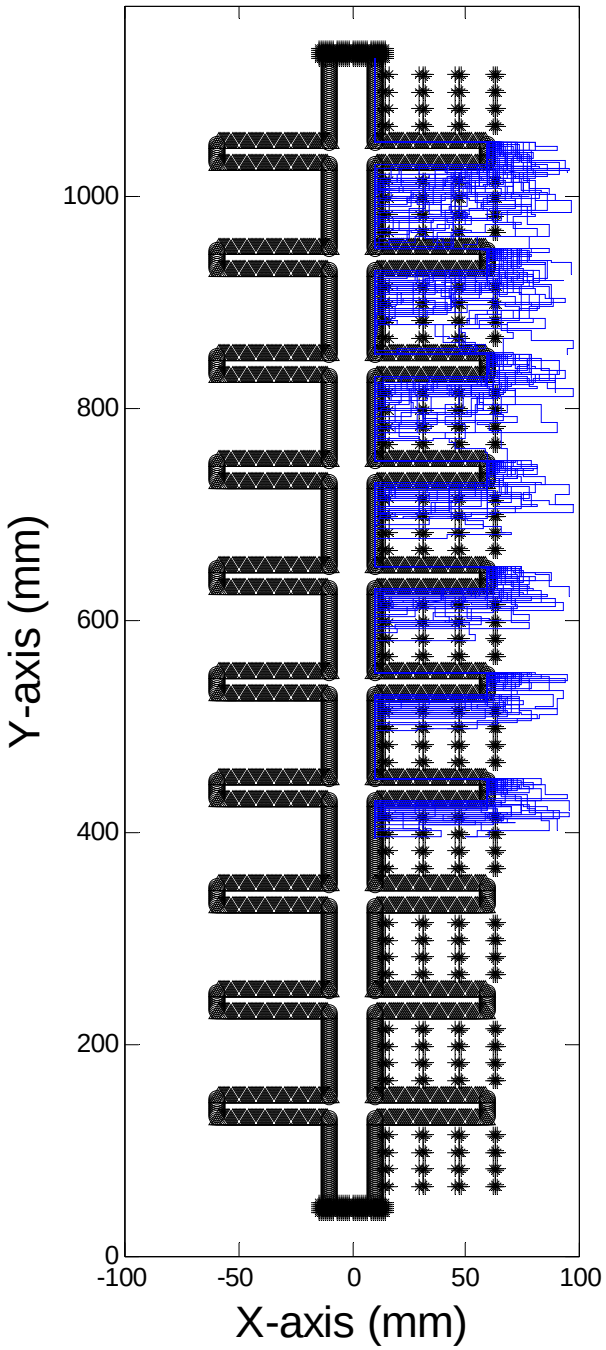

Figure 71. The 110 Times Arc Propagation Processes in Case 4

5.5 Simulation Results Comparison

The simulation results of four cases are shown in previous four sections. The electric field of insulator model with different water particle distributions is analyzed to evaluate the influence of water particles on electric field distributions in the air and along the insulator surface. The field comparison from Point A to B (Figure 58) is shown in Figures 72 and 73 with different ESDD values. The field comparison along the leakage distance is shown in Figures 74 and 75 with different ESDD values.

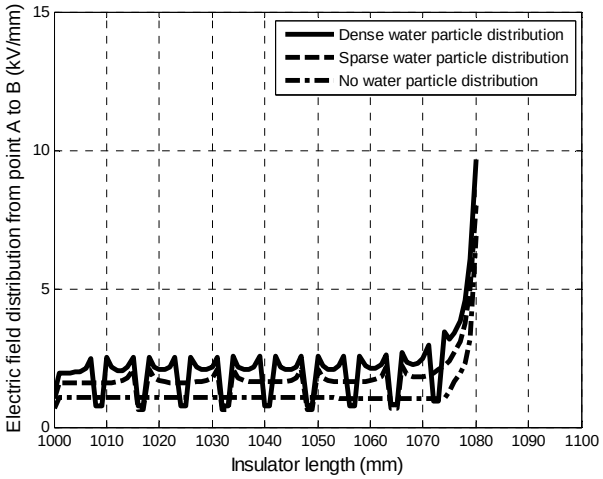

Figure 72. Electric Field Comparsion close to HV Electrode from Point A to B (ESDD 0.7 mg/cm^2)

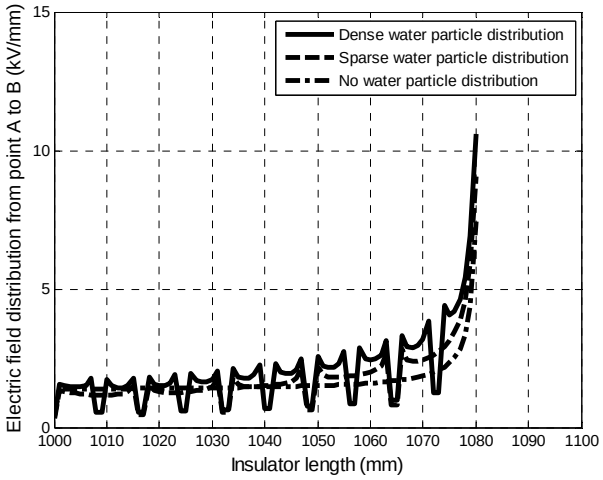

Figure 73. Electric Field Comparsion close to HV Electrode from Point A to B (ESDD 0.02 mg/cm^2)

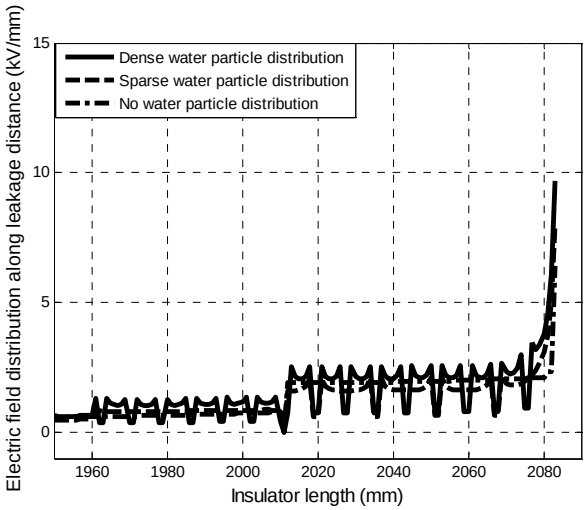

Figure 74. Electric Field Comparsion close to HV Electrode along Leakage Distance (ESDD 0.7 mg/cm^2)

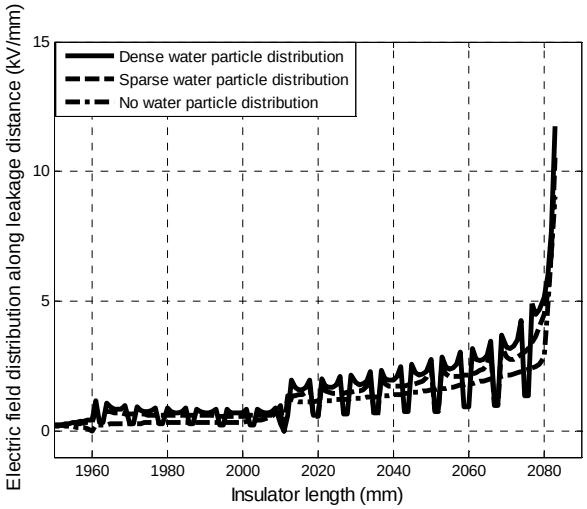

Figure 75. Electric Field Comparsion close to HV Electrode along :Leakage Distance (ESDD 0.02 mg/cm^2)

From electric field comparison above, it can be observed that the water particles distort the electric field distribution and the effects of particles intensify the electric field. The density of water particles is in proportional to the increase of the maximum electric field value.

The flashover probability as functions of ESDD under different density of water particles is shown in Figure 76.

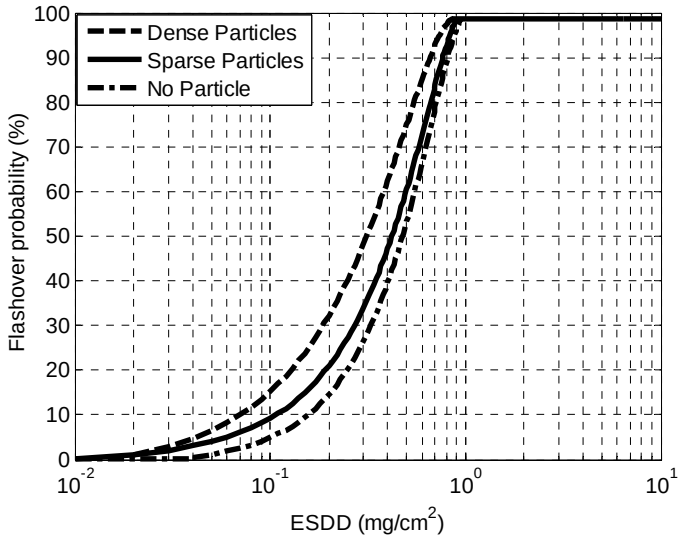

Figure 76. Flashover Probability as Functions of ESDD under Different Density of Water Particles

Figure 76 indicates that the flashover probability increases with the density of water particles. The 50% flashover voltage as functions of ESDD values is shown in Figure 77.

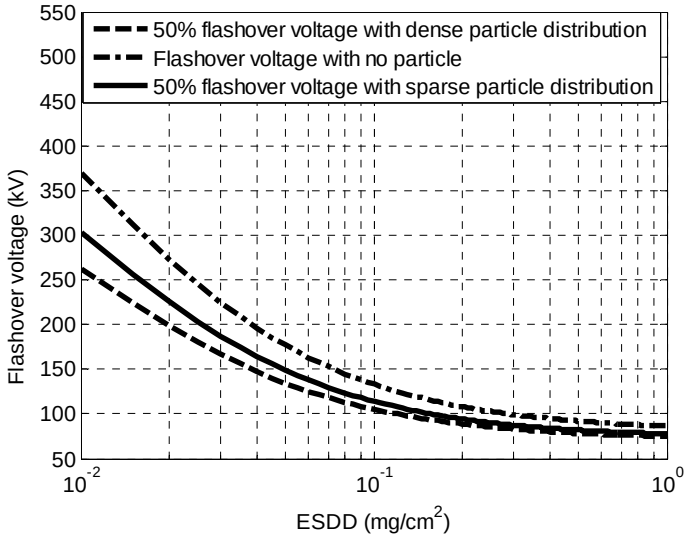

Figure 77. 50% Flashover Voltage as Functions of ESDD Values

The deviation between three cases is larger when ESDD values are below 0.05 mg/cm^2, which is representative of most locations.

6 COMPOSITE INSULATOR DIMENSION ANALYSIS

Insulator dimension is one of the key factors in insulator design. Suitable insulator geometry can provide high withstand voltage and save material during manufacture. Since the influence of dry arc distance on flashover performance has been fully studied, the effects of insulator shank radius, shed radius and number of sheds are discussed in this chapter. Insulator parameters of the base case for comparison are shown in Table 20.

Table 20. Insulator Parameter of Base Case

Voltage level (kV)	138	Shed radius	50
ESDD (mg/cm^2)	0.57	Sheath radius	10
Dry arc distance	1080	Number of sheds	10
Flashover probability (%)		50	

6.1 Effect of Insulator Shank Radius on Flashover Probability

Line composite insulator and station composite insulator have significant difference in shank radius (Figure 78), because the station composite insulator is likely to sustain more mechanical stress.

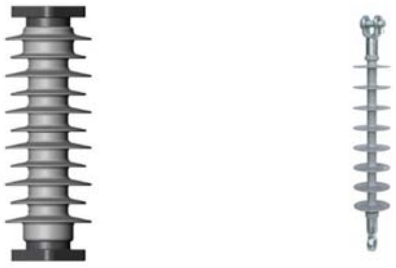

(a) Station Composite Insulator (b) Line Composite Insulator

Figure 78. Physical Dimension of Station and Line Composite Insulators

The schematic of station and line composite insulators in Figure 79 are shown below.

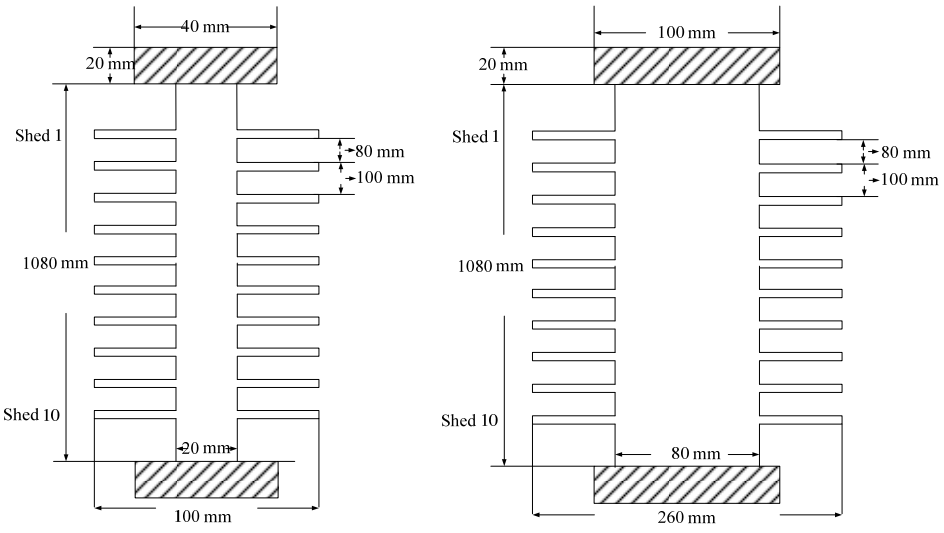

(a) (b)

Figure 79. Schematic of Station and Composite Insulator

In Figure 79(a), insulator shank radius is 10 mm. In Figure 79(b), insulator shank radius is 40 mm. Insulator shed radius and number of sheds remain same. The electric potential and field distributions along leakage distance are shown in Figure 80 and Figure 81. The leakage distance is normalized to 1 to compare the results.

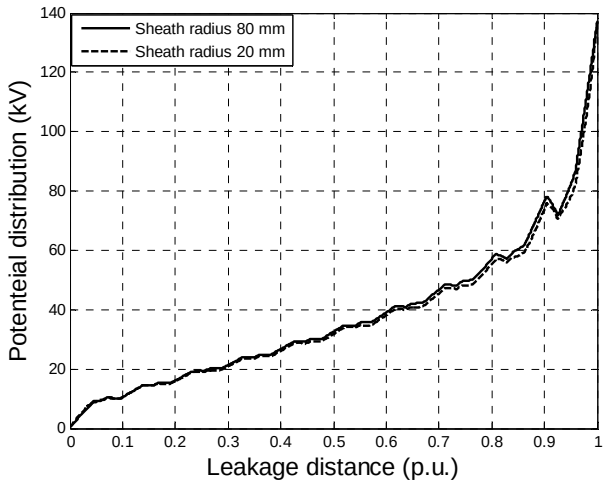

Figure 80. Potential Distribution along Insulator Leakage Distance

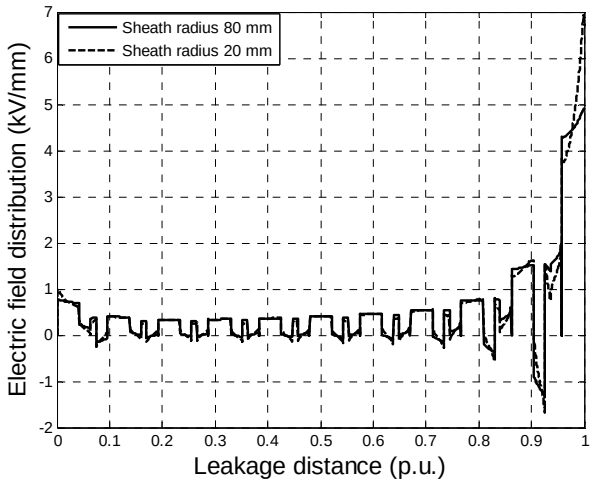

Figure 81. Electric Field Distribution along Insulator Leakage Distance

The flashover probability as a function of insulator shank radius is shown in Figure 82.

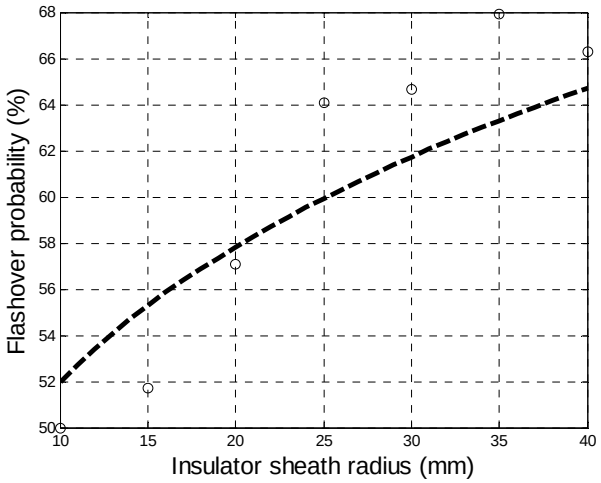

Figure 82. Flashover Probability as a Function of Insulator Shank Radius

The function of flashover probability versus insulator shank radius is shown below.

$$y = 19.7x^{0.23} + 18 \tag{77}$$

Where y is the flashover probability and x is insulator shank radius. Station insulator with large shank radius has higher flashover probability than line insulator with small shank radius, since the large shank radius reduces the surface resistivity.

6.2 Effect of Insulator Shed Radius on Flashover Probability

The schematic of line insulators with different shed radius are shown below.

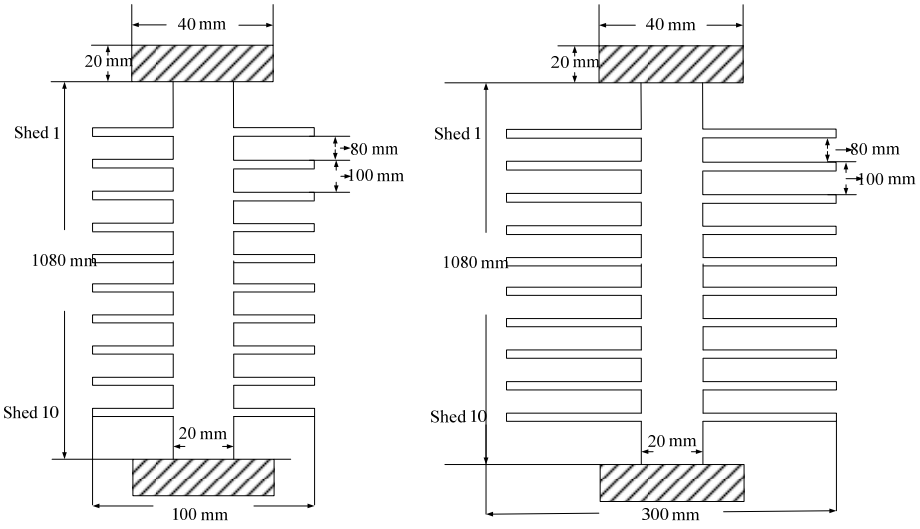

(a) (b)

Figure 83. Insulator with Different Dry Arc Distance

In Figure 83(a), insulator shed radius is 50 mm. In Figure 83(b), insulator shed radius is 150 mm. Insulator shank radius and number of sheds remain same. The electric potential and field distributions along leakage distance are shown in Figure 84 and Figure 85. The leakage distance is normalized to 1 to compare the results.

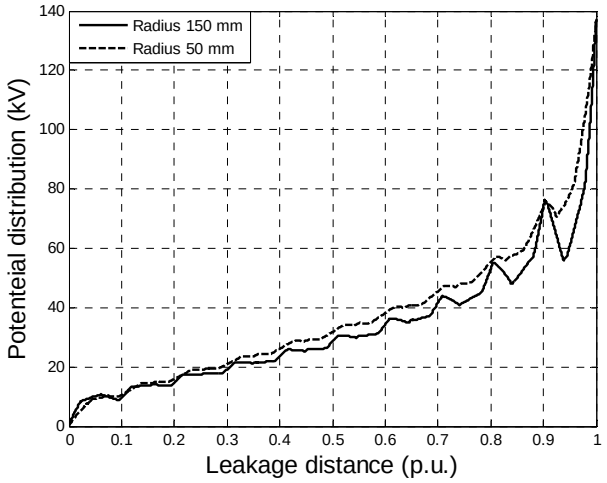

Figure 84. Potential Distributions along the Insulator Leakage Distance

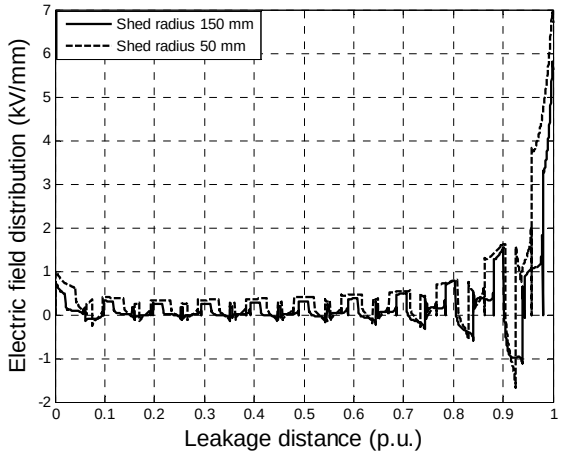

Figure 85. Electric Field Distributions along the Insulator Leakage Distance

The flashover probability as a function of insulator shed radius is shown in Figure 86.

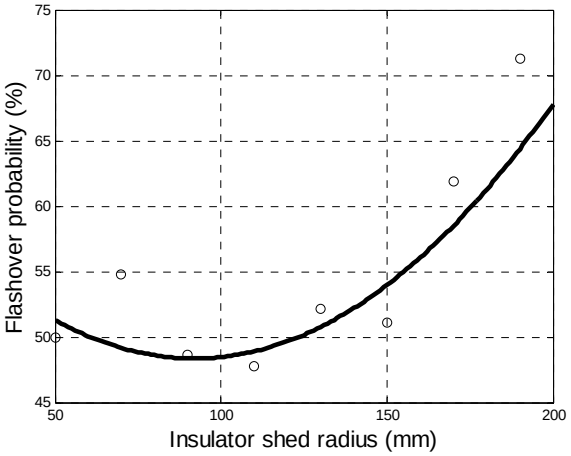

Figure 86. Flashover Probability as a Function of Insulator Shed Radius

The function of flashover probability versus insulator shed radius is shown below.

$$y = 0.00167x^2 - 0.307x + 62.47 \tag{78}$$

Where y is the flashover probability and x is insulator shed radius. It can be seen that increase of shed radius would reduce the flashover probability in the first place by lengthening the leakage distance. However, the flashover probability would increase when shed radius exceeds the critical value (117 mm), because the decreasing surface resistivity becomes the main factor to impact flashover performance.

6.3 Effect of Number of Sheds on Flashover Probability

Insulators with different dry arc distances are shown Figure 87.

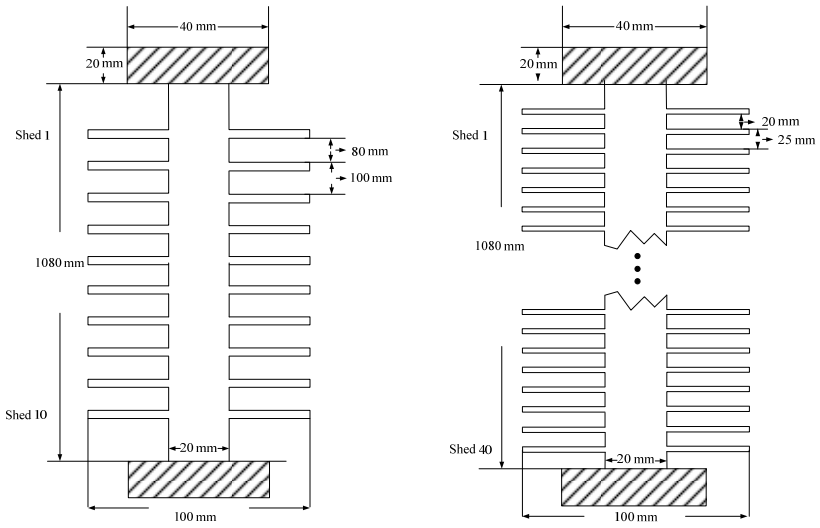

(a) (b)

Figure 87. Insulator with Different Dry Arc Distance

In Figure 87(a), number of shed is 10. In Figure 87(b), number of shed is 40. Insulator shank radius and insulator shed radius remain same. The electric potential and field distributions along leakage distance are shown in Figure 88 and Figure 89. The leakage distance is normalized to 1 to compare the results.

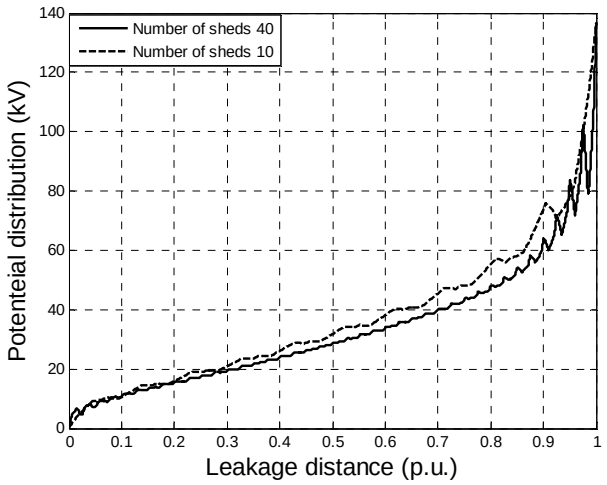

Figure 88. Potential Distributions along the Insulator Leakage Distance

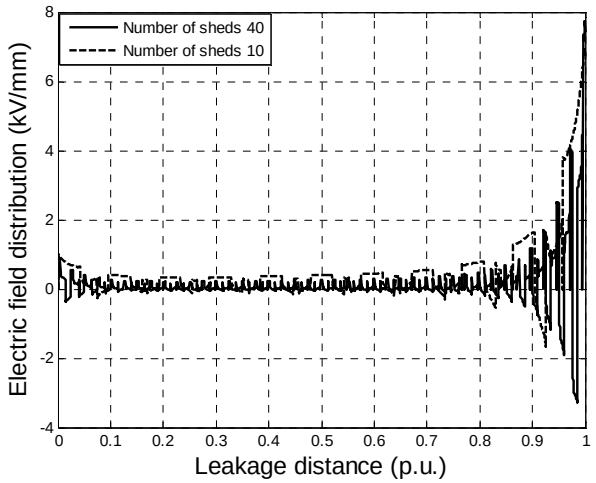

Figure 89. Electric Field Distributions along the Insulator Leakage Distance

The flashover probability as functions of insulator shed radius is shown in Figure 90.

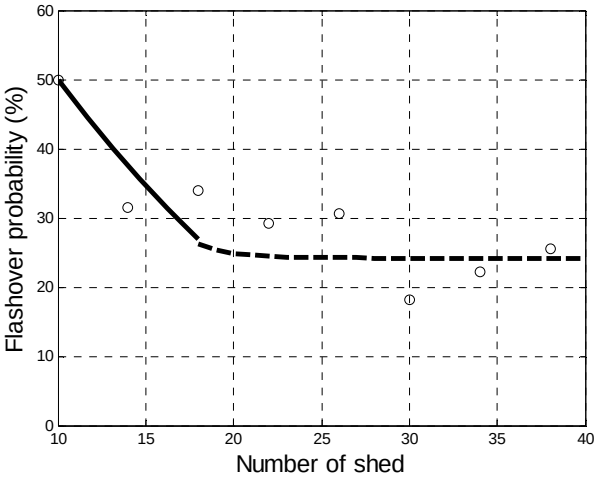

Figure 90. Flashover Probability as Functions of Insulator Shed Radius

The function of flashover probability versus number of sheds is shown below.

$$y = \begin{cases} -2.875x + 78.75 & x < 18 \\ 3.7 \times 10^3 (0.58^x) + 24.2 & x > 18 \end{cases} \quad (79)$$

Where y is the flashover probability and x is number of sheds. It can be observed that adding number of sheds decreases flashover probability. Nevertheless, the flashover performance improvement would be negligible when number of sheds is larger than the critical value.

7 INSULATOR FLASHOVER PERFORMANCE WITH WATER DROPLETS ON HYDROPHOBIC SURFACE

7.1 Hydrophobicity Classification

Hydrophobicity is the physical property of a molecule repelled from water. Contact angle is defined as the angle between water and solid surface (Figure 91). It is used to measure the wettability of a surface or material. The calculation equation of contact angle is shown below [57].

$$\gamma_{SG} = \gamma_{SL} + \gamma_{LG} \cos\theta \tag{80}$$

where γ_{SG} is interfacial tension between solid surface and gas. γ_{SL} is interfacial tension between solid surface and liquid. γ_{LG} is interfacial tension between gas and liquid.

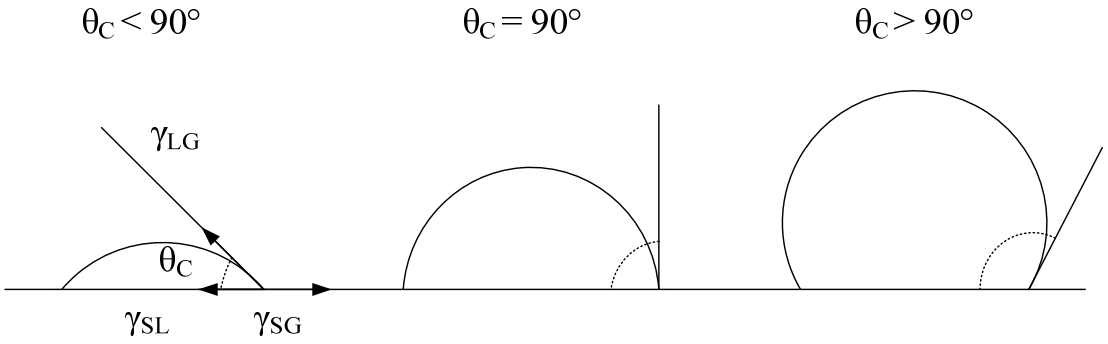

Figure 91. Contact Angle and Droplet Geometry

The wet condition on the insulator surface can be identified into seven hydrophobicity classes (HC). The criteria for the hydrophobicity classification are shown in Table 21. HCs are categorized by different contact angles and forms of water droplets.

Table 21. Criteria for the Hydrophobicity Classification [58]

HC	Description
1	Only discrete droplets are formed. $\theta_C \approx 80°$ or larger for the majority of droplets.
2	Only discrete droplets are formed. $50° < \theta_C < 80°$ for the majority of droplets.
3	Only discrete droplets are formed. $20° < \theta_C < 50°$ for the majority of droplets. Usually they are no longer circular.
4	Both discrete droplets and wetted traces from the water runnels are observed (i.e. $\theta_C = 0°$). Completely wetted areas < 2 cm^2. Together they cover < 90% of the tested area.
5	Some completely wetted areas > 2 cm^2, which cover < 90% of the tested area.
6	Wetted areas cover > 90%, i.e. small unwetted areas (spots/traces) are still observed.
7	Continuous water film over the whole tested area.

7.2 Electric Field Distribution of Water Droplets on Hydrophobic Surface

Electric field distribution of water droplets on hydrophobic surface is calculated in this section. Water droplets with different contact angles are compared. Different number of water droplets is also analyzed in the model (Table 22).

Table 22. Water Droplet Model Dimensions

Voltage (kV)	10
Distance between electrodes (mm)	200
Water droplet diameter (mm)	2
Number of water droplets	1 2 3 4 5
Distance between droplets (mm)	1
Contact Angle (°)	30 50 80 90

Figure 92 shows the schematic of one water droplet model. Figure 93 shows the exact model details in the simulation platform.

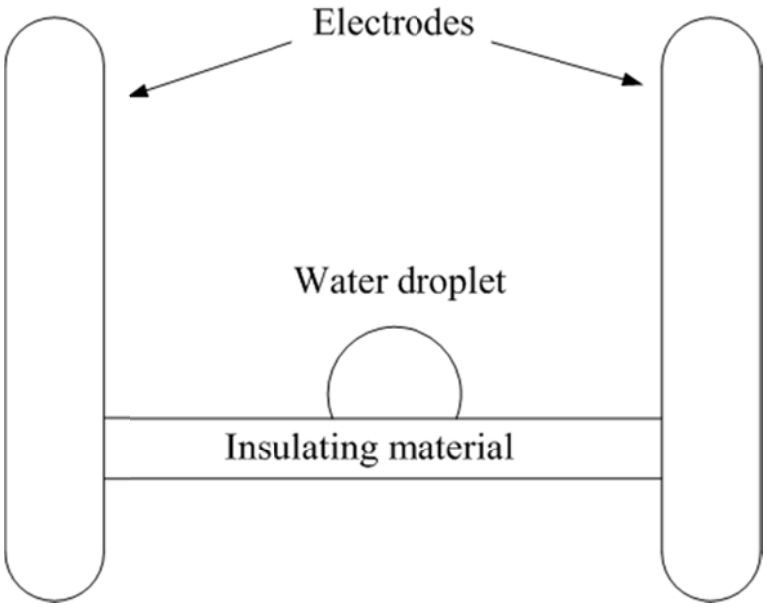

Figure 92. Schematic of One Water Droplet Model

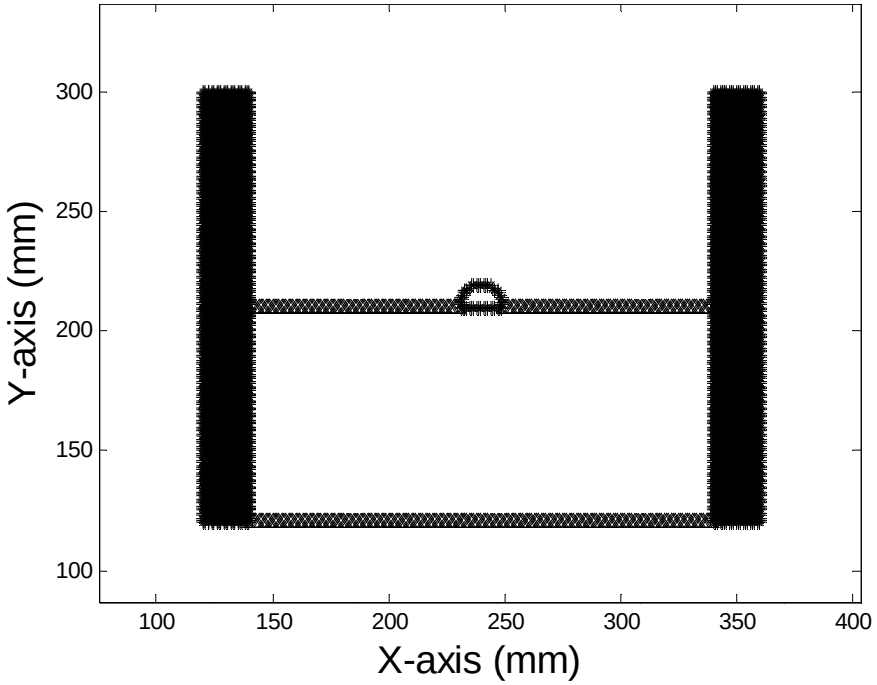

Figure 93. Exact Model Details on the Simulation Platform

The contact angle (θ_C) is varied from 30° to 90°. The geometry of water droplets in the model is shown in Figure 94.

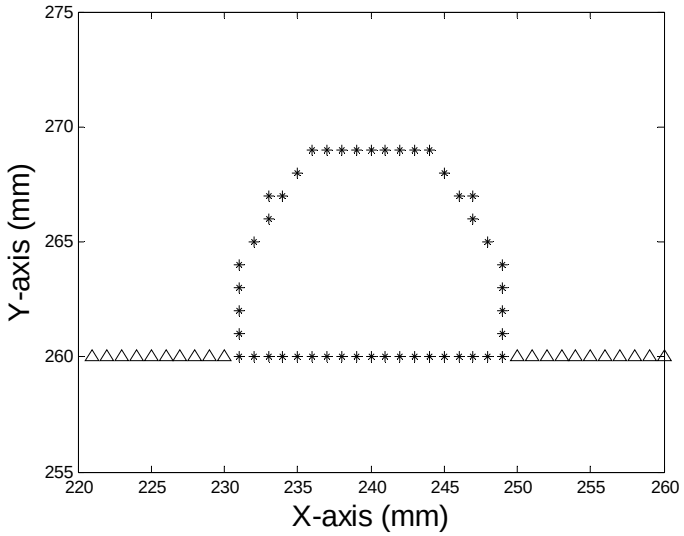

(a) Contact Angle = 90°

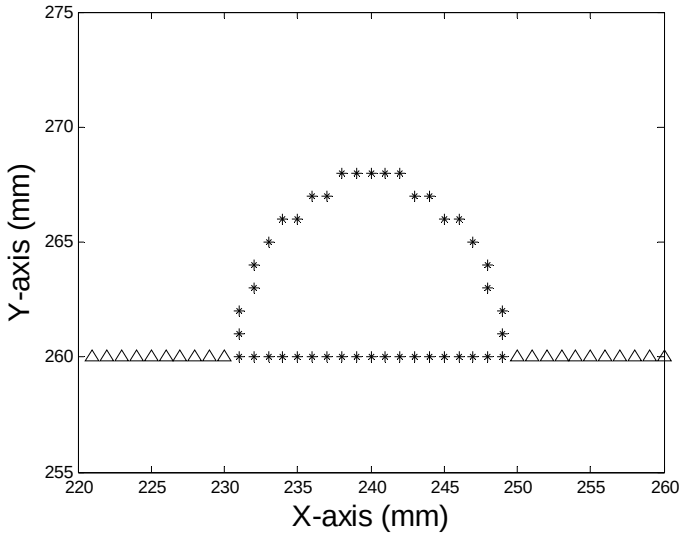

(b) Contact Angle = 80°

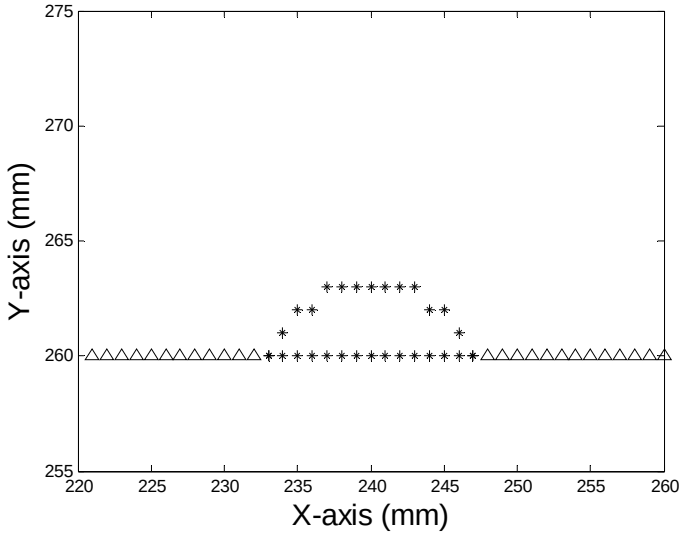

(c) Contact Angle = 50°

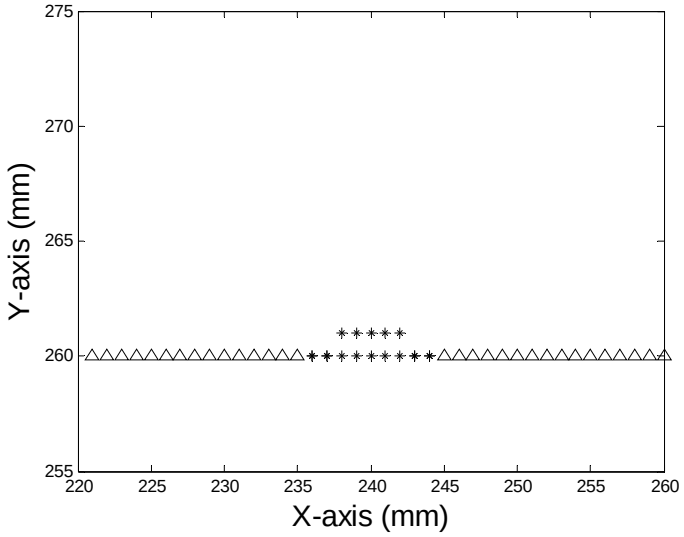

(d) Contact Angle = 30°

Figure 94. Different Contact Angles of Water Droplets

The electric field distribution along the surface is shown in Figure 95. It can be observed that the water droplet on the insulator surface cause severe field distortion. The maximum field distortion is 48.7% when compared to the electric field close to HV electrode.

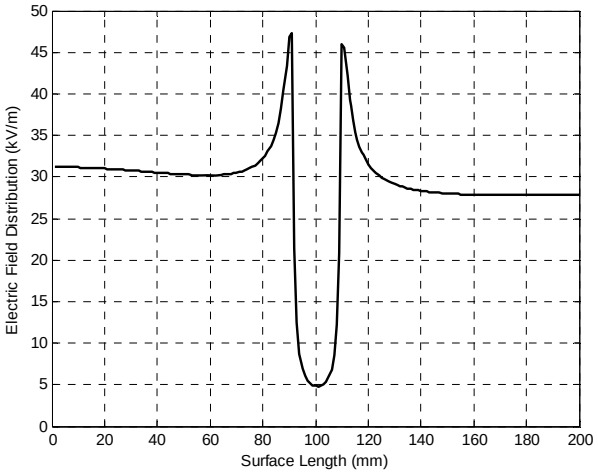

(a) Contact Angle = 90°

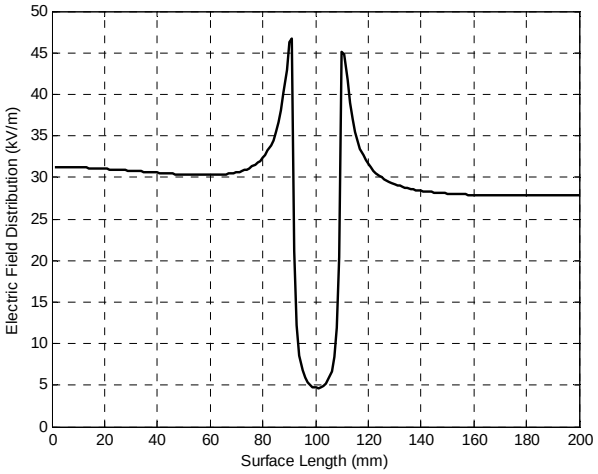

(b) Contact Angle = 80°

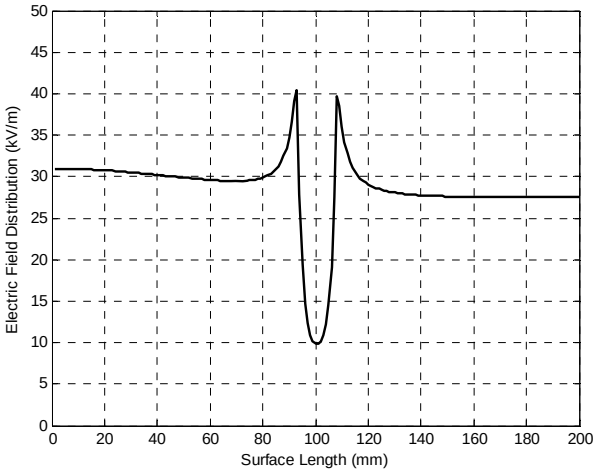

(c) Contact Angle = 50°

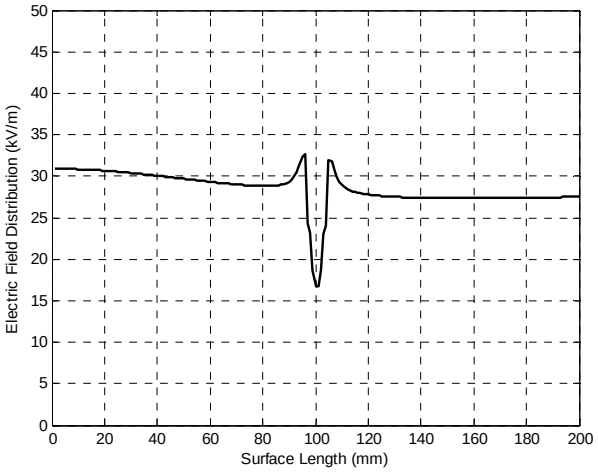

(d) Contact Angle = 30°

Figure 95. Electric Field Distribution of Water droplets with Different Contact Angles

Figure 95 indicates that the electric field distribution becomes distorted when the contact angle increases.

The number of water droplets varies from 1 to 5. The distance between water droplets is 1 mm. The five water droplets model schematic is shown in Figure 96.

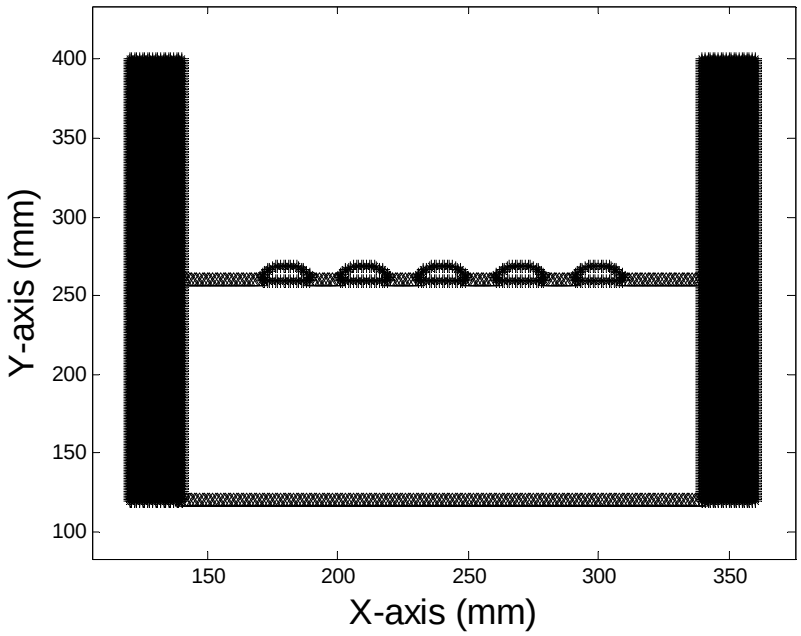

Figure 96. Model Details on Simulation Platform

The electric field distribution along the surface is shown in Figure 97.

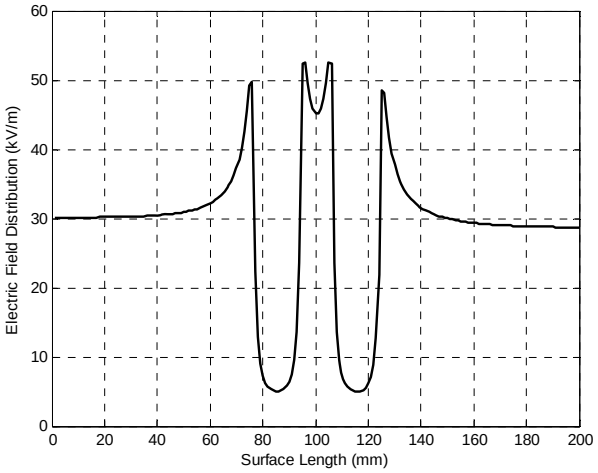

(a) Number of Droplets = 2

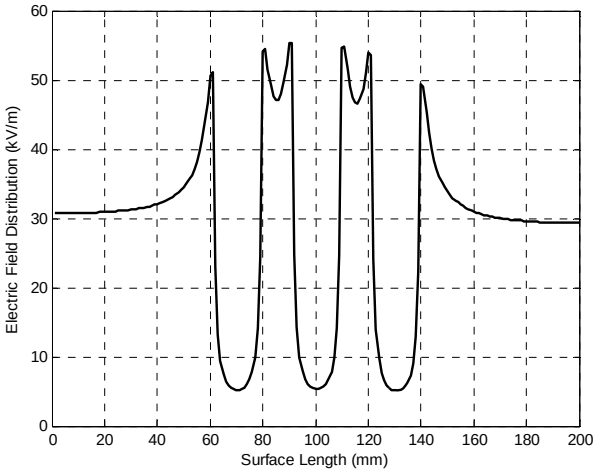

(b) Number of Droplets = 3

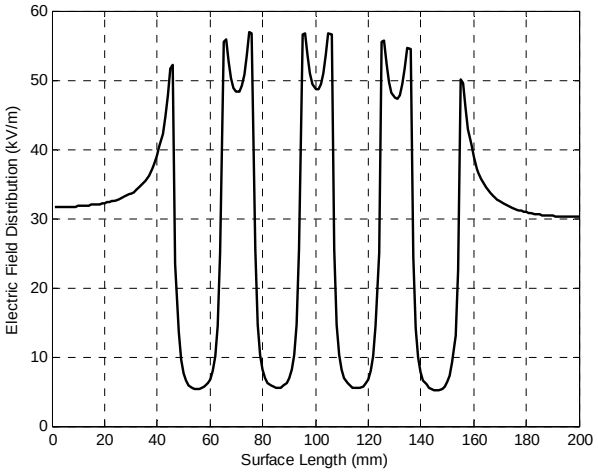

(c) Number of Droplets = 4

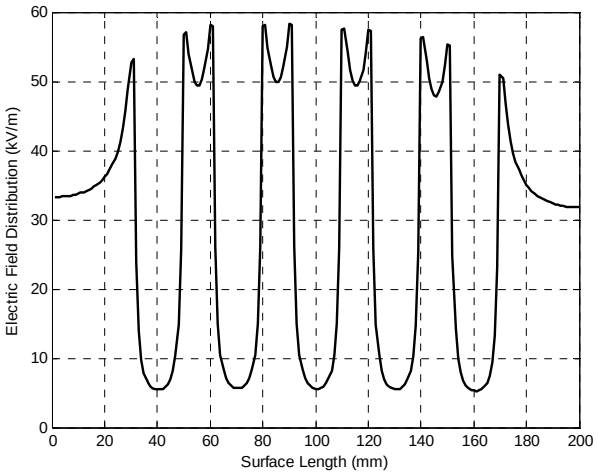

(d) Number of Droplets = 5

Figure 97. Electric Field Distribution of Water Droplets with Different Numbers

Figure 97 indicates that the electric field distortion becomes severe as the number of water droplets increases. Therefore, both contact angle and number of droplets intensify the electric field distortion.

7.3 Arc Propagation Results and Flashover Probability

The insulator dimension is shown in Figure 98. The supply voltage is 138 kV. The water droplets with different contact angles and radius are used to represent seven hydrophobicity classes. 110 times of arc propagations are repeated to calculate the flashover probability and 50% flashover voltages.

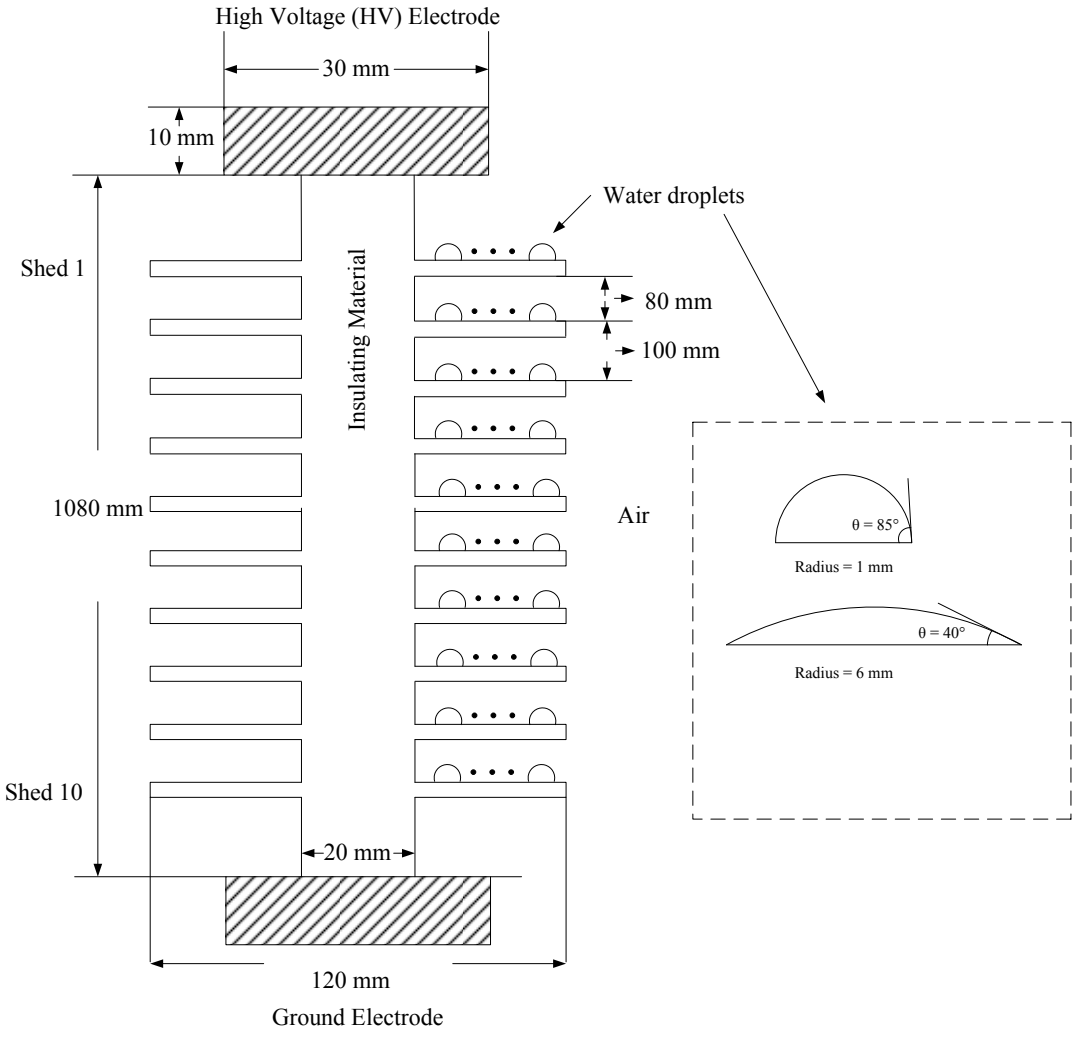

Figure 98. Insulator Dimension with Droplets on the Surface.

ESDD is set at 0.7 mg/cm^2. The detailed arc propagation processes of HC 1, 3, 5 and 7 are shown in Figure 99.

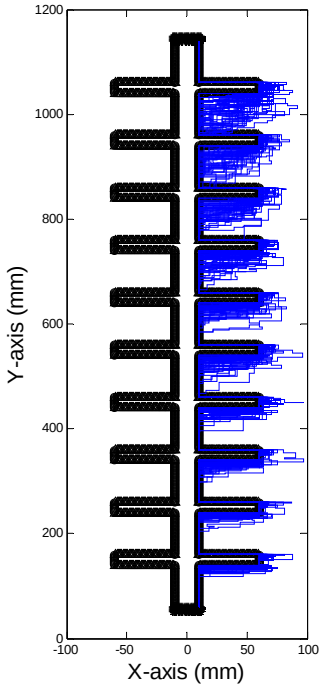

(a) HC = 1

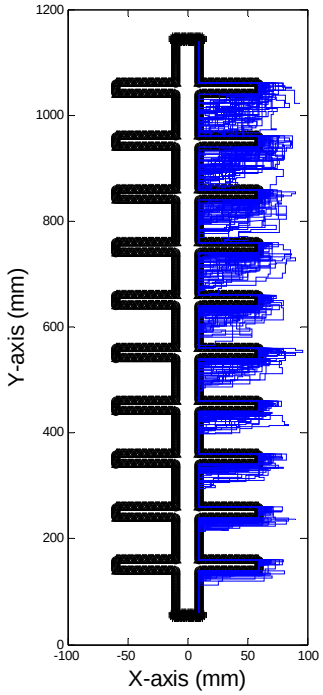

(b) HC = 3

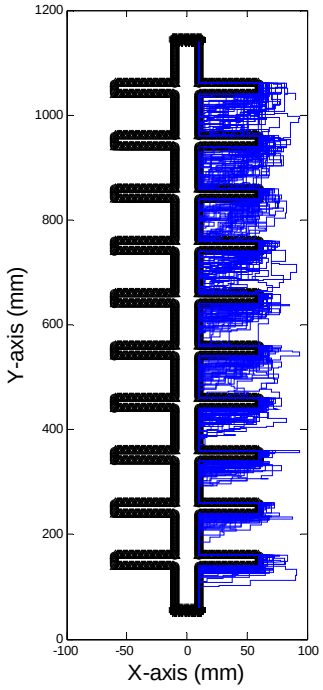

(c) HC = 5

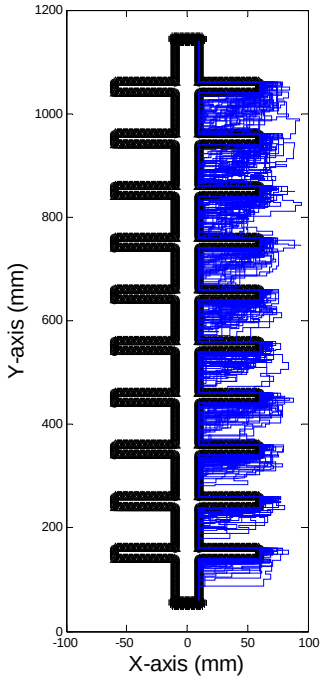

(d) HC = 7

Figure 99. Detailed Arc Propagation Processes

Flashover voltage as a function of HC is shown in Figure 100.

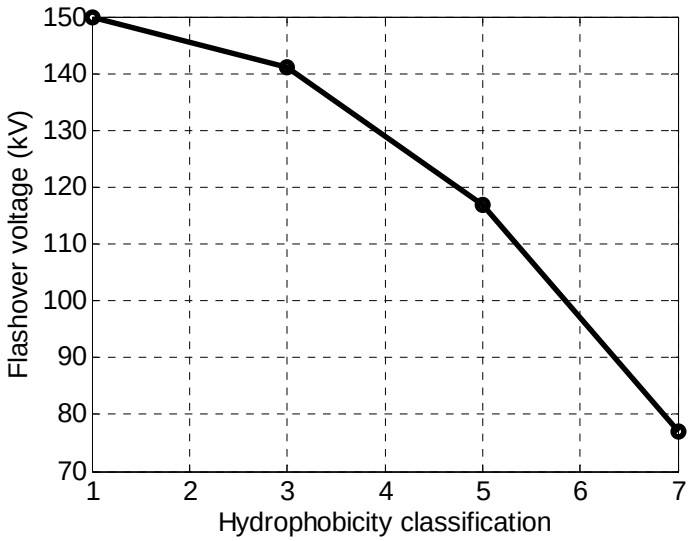

Figure 100. Flashover Voltage as a Function of HC

In Figure 100, it can be observed that the flashover voltage reduces as the insulator surface loses its hydrophobicity.

8 CONCLUSIONS AND FUTURE WORK

8.1 Conclusions

This research focuses on the simulation of flashover probability based on the electric field calculation and Random Walk Theory. The electric field distribution is calculated by variable-grid finite difference method, and arc propagation process depends on Random Walk Theory. The model makes some improvements over existing models, such as using a stochastic process to describe arc growth rather than determining the flashover by criteria equations. Supply voltage and ESDD values are two factors that mainly contribute to the probability of insulator flashover and arc jumping between insulator sheds. Water particles in the air also have effects on flashover performance. Additionally, the effects of different hydrophobicity classes have been investigated in the model. The conclusions of this research are listed below:

(1) Electric field distribution around the insulators is mainly affected by supply voltage and surface contamination levels. The vertical electric field from HV electrode to ground electrode is the dominant field vector.

(2) The insulator leakage distance reduces when the arc gets close to the ground electrode. Consequently, the electric field strength along the insulator surface increases with the arc propagation.

(3) If the pollution layer on the insulator surface is uniform, both supply voltage and ESDD values have influence on insulator flashover probability. Meanwhile,

supply voltage has positive effect on the probability mean of arc jumping between sheds. The probability standard deviation of arc jumping between sheds reduces if ESDD value increases.

(4) Water particles in the air significantly increase the insulator flashover probability, especially for the ESDD values in the range 0.01-0.1 mg/cm^2, which represents the majority of locations.

(5) Station insulator with large shank radius has higher flashover probability than line insulator with small shank radius, since the large shank radius reduces the surface resistivity. The increase of shed radius would reduce the flashover probability in the first place by lengthening the leakage distance. However, the flashover probability would increase when shed radius is larger than the critical value. Adding number of sheds decreases flashover probability. Nevertheless, the flashover performance improvement would be negligible when number of sheds exceeds the critical value.

(6) Insulator hydrophobic surface can significantly improve the insulator flashover performance under wet condition.

8.2 Future Work

The future work will aim at the simulation model in three dimensions and electric field analysis of defective insulators.

(1) Three dimension insulator model will be analyzed in the future. Dimension growth costs more CPU time and RAM space of the computer. Therefore, in order to reduce the computational complexity, both field calculation method and random walk process need to be optimized.

(2) Next step research includes the electric field calculation on defective insulators for AC and DC voltages. Different defect types, such as air bubble and conductive impurities will be modeled. The schematic of simulation model is shown in Figure 89. Grid-varied FDM will be used to calculate the electric field distribution along the dashed line (Figure 89). The purpose is to locate and identify the type of the defects by measuring the electric field around insulators, and then and replace them before failure occurs.

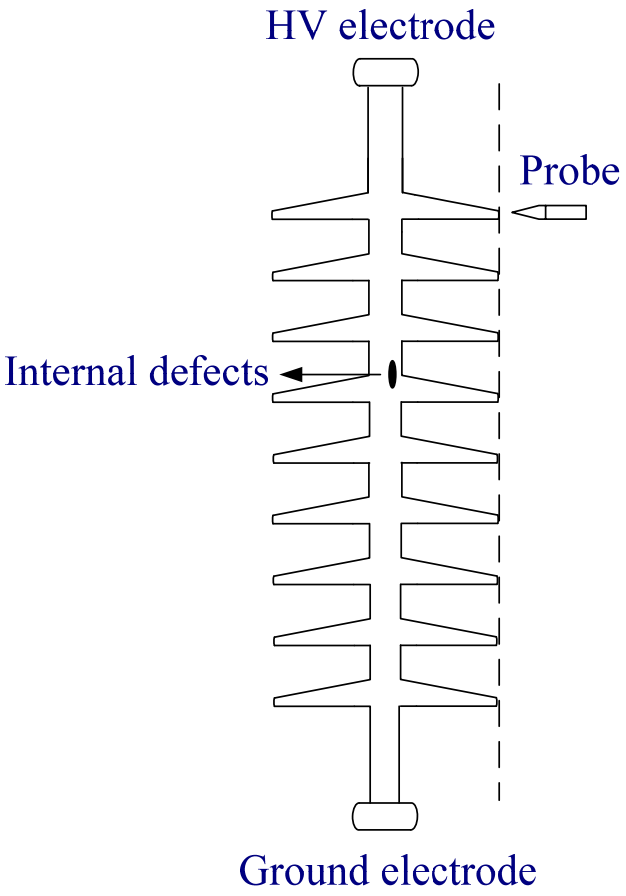

Figure 101. Insulator Model with Internal Defects

REFERENCES

[1] H. Ryan, Numerical analysis of electromagnetic fields, The Institution of Engineering and Technology, November 2013.

[2] R. R. Prabu, S. Usa, K. Udayakumar, M. A. Khan and S. S. M. A. Majeed, "Theoretical correlations amongst electrical and mechanical characteristics of polymeric housing materials for outdoor insulators," *IEEE Transactions on Dielectrics and Electrical Insulation*, vol. 15, no. 3, pp. 771-782, June 2008.

[3] Md. Abdus Salam, Modeling of Contaminated Insulator, LAP Lambert Academic Publishing, 2012.

[4] R. Matsuoka, S. Ito, K. Sakanishi and K. Naito, "Flashover on contaminated insulators with different diameters," *IEEE Transactions on Electrical Insulation*, vol. 26, no. 6, pp. 1140-1146, Dec 1991.

[5] S. Venkataraman and R. S. Gorur, "Prediction of flashover voltage of non-ceramic insulators under contaminated conditions," *IEEE Transactions on Dielectrics and Electrical Insulation*, vol. 13, no. 4, pp. 862-869, Aug. 2006.

[6] S. Zhao, X. Jiang, Z. Zhang, J. Hu and L. Shu, "Flashover Voltage Prediction of Composite Insulators Based on the Characteristics of Leakage Current," *IEEE Transactions on Power Delivery*, vol. 28, no. 3, pp. 1699-1708, July 2013.

[7] J. S. Rigden, Macmillan Encyclopedia of Physics. Simon & Schuster, 1996.

[8] G.B. Pontecorvo, Branislav Sitar, Gabriel I. Merson and Valery A. Chechin, Ionization Measurements in High Energy Physics, Springer Berlin Heidelberg, 2013.

[9] W. M. Haynes, CRC Handbook of Chemistry and Physics, CRC Press, 1992.

[10] E. B. Shand, "The dielectric strength of glass-an engineering viewpoint," *American Institute of Electrical Engineers, Transactions of the*, vol. 60, no. 8, pp. 814-818, August. 1941.

[11] Qing Yang, Rui Wang, Wenxia Sima, Chilong Jiang, Xing Lan and Markus Zahn, "Electrical circuit flashover model of polluted insulators under AC voltage based on the arc root voltage gradient criterion", Energies, vol. 5, 2012.

[12] F. A. M. Rizk, “Mathematical Models for Pollution Flashover”, Electra, Vol. 78, pp. 71-103, 1981.

[13] D. C. Jolly, T. C. Cheng and D. M. Otten, “Dynamic Theory of Discharge Growth over Contaminated Insulator Surfaces”, Conference Paper No. 74-068-3, *IEEE PES Winter Power Meeting*, 1974.

[14] R. Sundararajan and R. S. Gorur, “Dynamic Arc Modeling of Pollution Flashover Insulators under DC Voltages”, *IEEE Transactions on Electrical Insulation*, Vol. 28, No. 2, pp. 209-218, 1993.

[15] P. B. Zhou, Numerical analysis of electromagnetic fields, Springer Verlag, 1993.

[16] M. D. R. Beasley, J. H. Pickles, and G. Gallet, "Comparative study of three methods for computing electric fields," *Proceedings of the Institution of Electrical Engineers*, vol. 126, pp. 126-134, January 1979.

[17] R. Arora and W. Mosch, Numerical analysis of electromagnetic fields, Wiley-IEEE Press, August 2011.

[18] N. Cressie, "A Two-Dimensional Random Walk in the Presence of a Partially Reflecting Barrier," *Journal of Applied Probability*, vol. 11, no. 1, pp. 199-205, March 1974.

[19] J. S. T. Looms, Insulators with high voltages, Peregrinus on behalf of the Institution of Electrical Engineers, 1988.

[20] R. S. Gorur, E. A. Cherney and J. T. Burnham, Outdoor insulators, Ravi S. Gorur Inc, 1999

[21] Nouruddeen Bashir, High Voltage Transmission Line Ceramic Insulators, VDM Verlag Dr. Müller, 2010.

[22] M. A. Douar, A. Beroual and X. Souche, "Influence of the rise rate of voltage and leakage distance on flashover gradient and partial discharges level for various polymeric materials under AC stress," *IEEE Transactions on Dielectrics and Electrical Insulation*, vol. 22, no. 3, pp. 1644-1653, June 2015.

[23] S. Chakravorti and H. Steinbigler, "Capacitive-resistive field calculation on HV bushings using the boundary-element method," *IEEE Transactions on Dielectrics and Electrical Insulation*, vol. 5, no. 2, pp. 237-244, Apr 1998.

[24] M. C. Milholland, Glass insulator reference book, Olympia, 1967.

[25] E. Cherney *et al*., "Evaluation of and Replacement Strategies for Aged High-Voltage Toughened Glass-Suspension Insulators," *IEEE Transactions on Power Delivery*, vol. 30, no. 3, pp. 1145-1152, June 2015.

[26] E. Kuffel and W. S. Zaengl, High voltage engineering, Pergamon Press, 1984.

[27] M. Farzaneh, "Outdoor insulators: overview of in-service experience, inspection practice and future challenges," *2009 IEEE Electrical Insulation Conference*, Montreal, QC, 2009, pp. 542-550.

[28] K. O. Papailiou and F. Schmuck, Silicone Composite Insulators: Materials, Design, Applications (Power Systems), Springer, 1992.

[29] M. Amin, M. Akbar and M. N. Khan, "Aging Investigations of Polymeric Insulators: Overview and Bibliography," *IEEE Electrical Insulation Magazine*, vol. 23, no. 4, pp. 44-50, July-Aug. 2007.

[30] C. S. Richards, C. L. Benner, K. L. Butler-Purry, B. D. Russell, "Electrical behavior of contaminated distribution insulators exposed to natural wetting," *Power Delivery, IEEE Transactions on* , vol. 18, no. 2, pp. 551-558, April 2003.

[31] M. A. Salam, H. M. bin Hj Kassim, "Performance study of line post insulator under different pollution conditions," *Power and Energy Conference, 2008. PECon 2008. IEEE 2nd International* , pp. 18-21, 1-3 Dec. 2008

[32] H. Su, Z. Jia, Z. Guan and L. Li, "Mechanism of contaminant accumulation and flashover of insulator in heavily polluted coastal area," *IEEE Transactions on Dielectrics and Electrical Insulation*, vol. 17, no. 5, pp. 1635-1641, October 2010.

[33] M. A. R. M. Fernando and S. M. Gubanski, "Ageing of silicone rubber insulators in coastal and inland tropical environment," *IEEE Transactions on Dielectrics and Electrical Insulation*, vol. 17, no. 2, pp. 326-333, April 2010.

[34] F. M. Zedan, M. Akbar, A. S. Farag, T. C. Cheng, C. Y. Wu, "Review Performance of HV Transmission Line Insulators in Desert Conditions Part I: Review of Research and Methods Adopted Internationally," *Electrical Insulation, IEEE Transactions on*, vol. EI-18, no .2, pp. 97-109, April 1983.

[35] Abdulaziz-el-sulaiman and M. I. Qureshi, "Effect of Contamination on the Leakage Current of Inland Desert Insulators," *IEEE Transactions on Electrical Insulation*, vol. EI-19, no. 4, pp. 332-339, Aug. 1984.

[36] Artificial pollution tests on high voltage insulators to be used on AC systems, IEC 60507, 1991.

[37] K. H. Huehner and E. A. Thornton, The Finite Element Method for Engineers, John Wiley & Sons, Inc., 1982.

[38] H. Chang, S. Bong, -Y. Soo, "Efficient hybrid finite element-boundary element method for 3-dimensional open-boundary field problems," *Magnetics, IEEE Transactions on* , vol. 27, no. 5, pp. 4069-4072, September 1991.

[39] I. M. Smith, D. V. Griffiths, Programming the Finite Element Method, John Wiley & Sons, 2005.

[40] O. Paris, J. Lewiner, T. Ditchi, S. Hole and C. Alquie, "A finite element method for the determination of space charge distributions in complex geometry," *IEEE Transactions on Dielectrics and Electrical Insulation*, vol. 7, no. 4, pp. 556-560, August 2000.

[41] Balkrishna S. Annigeri and Kadin Tseng, Boundary Element Methods in Engineering, Springer Science & Business Media, 2012.

[42] D. A. S. Curran, B. A. Lewis and M. Cross, "A boundary element method for the solution of the transient diffusion equation in two dimensions", *Applied Mathematical Modeling*, vol. 10, no .2, pp. 107-113, April 1986.

[43] S. S. Bamji, A. T. Bulinski and K. M. Prasad, "Electric field calculations with the boundary element method," *IEEE Transactions on Electrical Insulation*, vol. 28, no. 3, pp. 420-424, Jun 1993.

[44] N. H. Malik, "A review of the charge simulation method and its applications," *IEEE Transactions on Electrical Insulation*, vol. 24, pp. 3-20, February 1989.

[45] H. EI-Kishky and R. S. Gorur, "Electric field computation on an insulating surface with discrete water droplets," *IEEE Trans. Dielectrics and Electrical Insulation*, vol. 3, pp. 450-456, June. 1996.

[46] M. J. Khan and P. H. Alexander, "Charge Simulation Modeling of Practical Insulator Geometries," *IEEE Transactions on Electrical Insulation*, vol. EI-17, no. 4, pp. 325-332, Aug. 1982.

[47] H. Singer, H. Steinbigler and P. Weiss, "A Charge Simulation Method for the Calculation of High Voltage Fields," *IEEE Transactions on Power Apparatus and Systems*, vol. PAS-93, no. 5, pp. 1660-1668, Sept. 1974.

[48] R. W. Hamming, Numerical Methods for Scientists and Engineers, Dover Publications, 1987.

[49] Randall J. LeVeque, Finite Difference Methods for Ordinary and Partial Differential Equations: Steady-State and Time-Dependent Problems, SIAM, Society for Industrial and Applied Mathematics, 2007.

[50] D. R. Bland, Solutions of Laplace's Equation, Springer Netherlands, 1961.

[51] T. Takuma, T. Kawamoto and H. Fujinami, "Charge Simulation Method with Complex Fictitious Charges for Calculating Capacitive-Resistive Fields," *IEEE Transactions on Power Apparatus and Systems*, vol. PAS-100, no. 11, pp. 4665-4672, Nov. 1981.

[52] M. C. Lai, Z. L. Li and X. B. Lin, "Fast solvers for 3D Poisson equations involving interfaces in a finite or the infinite domain," *Journal of Computational and Applied Mathematics*, vol. 191, pp. 106-125, 2006.

[53] F. A. M. Rizk, D. H. Nguyen, "AC Source-Insulator Interaction in HV Pollution Tests", *IEEE Transactions on Power Apparatus and Systems*, vol. 103,no. 4, pp 723-732, 1984.

[54] B. F. Hampton, "Flashover Mechanism of Polluted Insulation", Proceeding of the Institution of Electrical Engineers, vol. 111, no. 5, pp. 985-990, 1964.

[55] M. D. Noskov, A. S. Malinovski, M. Sack, A. J. Schwab, "Modelling of partial discharge development in electrical tree channels," *Dielectrics and Electrical Insulation, IEEE Transactions on* , vol. 10, no. 3, pp. 425-434, June 2003.

[56] L. Bo and R. S. Gorur, "Modeling flashover of AC outdoor insulators under contaminated conditions with dry band formation and arcing," *Dielectrics and Electrical Insulation, IEEE Transactions on* , vol. 19, no. 3, pp. 1037-1043, June 2012.

[57] IEEE Standard for High-Voltage Testing Techniques, *IEEE Std 4-2013 (Revision of IEEE Std 4-1995)*, pp. 1-213, May 10 2013.

[58] Ludvika, Hydrophobicity Classification Guide. Guide 1, 92/1, STRI, 1992.